

DEVELOPMENT OF FAST AND ROBUST SPECTRAL DECOMPOSITION
METHOD FOR NONLINEAR INDUSTRIAL LOADS WITH CURRENT
FREQUENCY SPECTRUM RICH IN HARMONIC AND INTERHARMONIC
CONTENT

A THESIS SUBMITTED TO
THE GRADUATE SCHOOL OF NATURAL AND APPLIED SCIENCES
OF
MIDDLE EAST TECHNICAL UNIVERSITY

BY

EDA UZ-LOĞOĞLU

IN PARTIAL FULFILLMENT OF THE REQUIREMENTS
FOR
THE DEGREE OF DOCTOR OF PHILOSOPHY
IN
ELECTRICAL AND ELECTRONICS ENGINEERING

AUGUST 2016

Approval of the thesis:

**DEVELOPMENT OF FAST AND ROBUST SPECTRAL DECOMPOSITION
METHOD FOR NONLINEAR INDUSTRIAL LOADS WITH CURRENT
FREQUENCY SPECTRUM RICH IN HARMONIC AND INTERHARMONIC
CONTENT**

submitted by **EDA UZ-LOĞOĞLU** in partial fulfillment of the requirements for the
degree of **Doctor of Philosophy in Electrical and Electronics Engineering Depart-**
ment, Middle East Technical University by,

Prof. Dr. Gülbin Dural Ünver
Dean, Graduate School of **Natural and Applied Sciences** _____

Prof. Dr. Gönül Turhan Sayan
Head of Department, **Electrical and Electronics Engineering** _____

Prof. Dr. Muammer Ermiş
Supervisor, **Electrical and Electronics Eng. Dept., METU** _____

Assoc. Prof. Dr. Özgül Salor Durna
Co-supervisor, **Electrical-Electronic Eng. Dept., Gazi Uni.** _____

Examining Committee Members:

Assoc. Prof. Dr. Umut Orguner
Electrical and Electronics Eng. Dept., Hacettepe University _____

Prof. Dr. Muammer Ermiş
Electrical and Electronics Eng. Dept., METU _____

Prof. Dr. Işık Çadircı
Electrical and Electronics Eng. Dept., METU _____

Assist. Prof. Dr. Tolga İnan
Electrical and Electronics Eng. Dept., TED University _____

Assist. Prof. Dr. Murat Göl
Electrical and Electronics Eng. Dept., METU _____

Date: _____

I hereby declare that all information in this document has been obtained and presented in accordance with academic rules and ethical conduct. I also declare that, as required by these rules and conduct, I have fully cited and referenced all material and results that are not original to this work.

Name, Last Name: EDA UZ-LOĞOĞLU

Signature :

ABSTRACT

DEVELOPMENT OF FAST AND ROBUST SPECTRAL DECOMPOSITION METHOD FOR NONLINEAR INDUSTRIAL LOADS WITH CURRENT FREQUENCY SPECTRUM RICH IN HARMONIC AND INTERHARMONIC CONTENT

Uz-Loğoğlu, Eda

Ph.D., Department of Electrical and Electronics Engineering

Supervisor : Prof. Dr. Muammer Ermiş

Co-Supervisor : Assoc. Prof. Dr. Özgül Salor Durna

August 2016, 108 pages

Nonlinear industrial loads such as AC arc furnaces and induction melting furnaces with resonant converters exhibit highly distorted currents rich in harmonic and interharmonic frequency components. Detection of these harmonics and interharmonics is crucial for applying countermeasures to achieve power quality requirements defined by the regulations of the power system operator. Fast and accurate harmonic and interharmonic detection in a power system experiences some difficulties due to the fact that power system frequency varies in time while the harmonic and interharmonic content is also time-varying. Hence Fourier Analysis based methods are slow and inaccurate to be used with compensation systems such as active filters. The aim of this thesis is to develop methods both fast and robust under time-varying fundamental frequency and spectrum conditions as well as in cases of unbalanced currents drawn by nonlinear industrial loads. Therefore, in this thesis, a novel method which combines the multiple synchronous reference frame (MSRF) analysis with the Kalman filter is proposed in order to take the advantage of the prediction capability of the Kalman filter and the accurate performance of the MSRF analysis. This algorithm, which provides the positive- and negative-sequences of all harmonic and interharmonic components under consideration, is implemented on the NVIDIA Jetson TX1 graphics processing unit (GPU). Results proves that the decomposition of the har-

monic and the interharmonic components is achieved accurately with a microsecond latency that allows the proposed algorithm to be used in a real-time operation

Keywords: Graphical Processing Unit (GPU), Harmonics, Interharmonics, Multiple Synchronous Reference Frame Analysis (MSRF), Power Quality (PQ)

ÖZ

HARMONİK VE ARAHARMONİK İÇERİĞİ YÜKSEK AKIM FREKANS SPEKTRUMUNA SAHİP DOĞRUSAL OLMAYAN ENDÜSTRİYEL YÜKLER İÇİN HIZLI VE GÜRBÜZ SPEKTRAL ÇÖZÜMLEME YÖNTEMLERİNİN GELİŞTİRİLMESİ

Uz-Loğoğlu, Eda

Doktora, Elektrik ve Elektronik Mühendisliği Bölümü

Tez Yöneticisi : Prof. Dr. Muammer Ermiş

Ortak Tez Yöneticisi : Doç. Dr. Özgül Salor Durna

Ağustos 2016 , 108 sayfa

AA ark ocakları ve rezonant dönüştürücülü endüksiyon ergitme ocakları gibi doğrusal olmayan endüstriyel yükler, harmonik ve araharmonik içeriği yüksek, oldukça bozuk akım üretirler. Bu harmonik ve araharmoniklerin algılanması, güç sistemi işletmeninin tanımladığı güç kalitesi isterlerini sağlayabilmek adına önlemler alınabilmesi için önemlidir. Bir güç sisteminde hızlı ve doğru harmonik ve araharmonik algılama, harmonik ve araharmonik içeriği zamanla değişirken, güç sistemi frekansının da zaman içinde değişmesi nedeniyle, bazı zorluklar içermektedir. Bu yüzden Fourier çözümleme tabanlı yöntemler, aktif filtre gibi kompanzasyon sistemleri için yavaş ve doğru olmayan sonuçlar üretir. Bu tezin amacı, zamanla değişen temel frekans ve spektrumların yanı sıra, doğrusal olmayan endüstriyel yüklerin çektiği dengesiz akımlar olduğu zaman, hızlı ve gürbüz çalışan yöntemler geliştirmektir. Bu nedenle bu tezde, çoklu senkron referans tabanlı (ÇSRT) analiz ile Kalman filtreyi birleştirilen, Kalman filtresinin tahmin yeteneğine sahip ve aynı zamanda ÇSRT analizinin doğru sonuç veren performansından faydalanan özgün bir yöntem sunulmuştur. İlgilenilen bütün harmoniklerin ve araharmoniklerin pozitif ve negatif bileşenlerinin bulunmasını sağlayan bu algoritma, NVIDIA'nın Jetson TX1 kodlu grafik işleme ünitesinde uygulanmıştır. Sonuçlar gösteriyor ki, harmonik ve araharmonik bileşenlerine ayırıştırma işlemi sunulan

bu yöntem ile mikro saniye mertebelerinde gecikmeyle doğru sonuçlar vermektedir. Bu da yöntemin gerçek zamanlı kullanıma uygun olduğunu göstermektedir.

Anahtar Kelimeler: Araharmonikler, Çoklu Senkron Referans Düzlem Analizi, Grafik İşleme Ünitesi, Güç Kalitesi (GK), Harmonikler

TO MY BELOVED FAMILY

ACKNOWLEDGMENTS

First and foremost I would like to express my deepest gratitude to my advisors Prof. Dr. Muammer Ermiř and Dr. Özgöl Salor Durna for their guidance, encouragement and supervision throughout this research and their valuable contributions to my career.

I would also thank my thesis committee for their valuable comments and suggestions.

I gratefully acknowledge Ege-Celik and Nursan Iron and Steel Plant Authorities for providing permission and support to make online measurements inside their facilities.

I would like to thank my friends and my beloved family for their sacrifice, unconditional support and motivation.

Last but not least, I would like express my special thanks to my dearest husband Berker, without whose love, encouragement and support, I would not have finished this thesis.

TABLE OF CONTENTS

ABSTRACT	v
ÖZ	vii
ACKNOWLEDGMENTS	x
TABLE OF CONTENTS	xi
LIST OF TABLES	xiii
LIST OF FIGURES	xiv
LIST OF ABBREVIATIONS	xviii
CHAPTERS	
1 INTRODUCTION	1
1.1 Problem Definition	5
1.2 Contributions	11
1.3 Outline of the Thesis	12
2 MULTIPLE SYNCHRONOUS REFERENCE FRAME ANALYSIS	15
2.1 Classification of the Problem	21
2.2 Implementation of the Proposed Method	25
2.2.1 Asymmetrical Balanced Three-Phase Current System	26

2.2.2	Asymmetrical Unbalanced Three-Phase Current System	30
3	APPLICATION OF MSRF	37
3.1	Results of MSRF Analysis Applied on Some Important Harmonics and Interharmonics	40
3.2	Verification of MSRF Results by Comparing Them with DFT Results	51
4	PROPOSED METHOD	63
4.1	Kalman Prediction Filter	65
4.2	GPU-based Implementation	72
4.2.1	Code Development and Optimization in CUDA	73
4.2.2	Developed System on GPU Framework	79
4.3	Results of the Overall System	82
5	DISCUSSIONS AND CONCLUSIONS	93
5.1	Possible Application Areas	95
	REFERENCES	99
	APPENDICES	
	CURRICULUM VITAE	107

LIST OF TABLES

TABLES

Table 1.1	Power System Harmonics.	7
Table 2.1	Symmetrical components resulting from the respective three phase sets. Reconstructed from the figure in [1]. (SBS: symmetrical balanced set, SUS: symmetrical unbalanced set, ABS: asymmetrical balanced set, AUS: asymmetrical unbalanced set) Superscripts + and - represent positive- and negative-sequence components, respectively.	17
Table 3.1	Interharmonics and harmonics in line current waveforms on MV side of a sample AC EAF transformer (mean RMS values over a tap-to-tap time; positive-sequence of the fundamental current is assumed to be 100%.	52

LIST OF FIGURES

FIGURES

Figure 1.1 A 135-MVA, 135-tonne electric arc furnace, first melting cycle just after commissioning / by courtesy of NURSAN Iron and Steel Inc., Payas, Iskenderun, Turkey.	6
Figure 1.2 The effects of the conventional passive shunt filters to the PCC. Figures taken from [2].	8
Figure 2.1 Positive- (I_A^+ , I_B^+ , I_C^+), negative- (I_A^- , I_B^- , I_C^-) and zero-sequence (I_A^o , I_B^o , I_C^o) decomposition of an arbitrary three-phase system.	16
Figure 2.2 Relationship between the two different types of 3-phase symmetrical sets (SBS and SUS) and their dqo components.(Id, Iq: dq components with 50Hz; Idn, Iqn: dq components with -50Hz).	20
Figure 2.3 Relationship between two different types of 3-phase asymmetrical sets (ABS and AUS) and their dqo components.(Id, Iq: dq components with 50Hz; Idn, Iqn: dq components with -50Hz).	21
Figure 2.4 Illustration of the measurement point (MP), whose data is used in this thesis, in a typical transformer substation supplying the AC EAF. . . .	22
Figure 2.5 Earth current flow path due to the over-voltages on inductive elements during the energization and de-energization of the EAF transformer or sudden movement of one of the electrodes.	23
Figure 2.6 The rate of variation of the three-phase line current during abnormal operating conditions.	24
Figure 2.7 The sum of the instantaneous three-phase line currents of the AC EAF during a tap-to-tap time.	24
Figure 2.8 The instantaneous real power consumption of the AC EAF, with the corresponding charge periods.	25
Figure 2.9 Positive- and negative-sequence decomposition for an asymmetrical and balanced three-phase system.	27

Figure 2.10 Online extraction of direct current and fundamental current components (both positive- and negative-sequence) from the actual three phase line current waveforms sampled at a rate of 25.6 kHz/channel in the field.	28
Figure 2.11 Online extraction of line current harmonic components (both positive- and negative-sequence) by MSRF analysis.	28
Figure 2.12 Online extraction of interharmonic current components with 5-Hz resolution (both positive- and negative-sequence) by MSRF analysis. w_{iH} represents the interharmonic frequencies and f_1 is the fundamental frequency.	29
Figure 2.13 Online extraction of direct current and fundamental current components for unbalanced systems (all positive-, negative- and zero-sequences) from the actual three phase line current waveforms sampled at a rate of 25.6 kHz/channel in the field.	36
Figure 3.1 Actual line current waveforms recorded on the MV side of EAF transformer (ten-cycle window during the boring phase of the EAF).	37
Figure 3.2 Frequency spectrum of 10-cycle current waveform obtained from Figure 3.1 by MSRF analysis in 5-Hz resolution.	38
Figure 3.3 Frequency response of the second order Butterworth LPF whose cut-off frequency is set to 2.5 Hz.	39
Figure 3.4 Fundamental components of the line currents obtained from the actual current waveforms given in Figure 3.1 by SRF analysis illustrated in Figure 2.10.	41
Figure 3.5 Second harmonic components of the line currents obtained from the actual current waveforms given in Figure 3.1 by MSRF analysis illustrated in Figure 2.11.	42
Figure 3.9 Positive-sequence (black colored) and negative-sequence (grey colored) RMS current components of some interharmonics in comparison with the RMS of the second harmonic current component (cycle-by-cycle RMS current calculation over a tap-to-tap time).	51
Figure 3.10 Computation of frequency spectrum of the three-phase EAF currents on 10-cycle FFT windows sliding one-cycle at each computation step.	53
Figure 3.11 Samples taken on an ideal sinc function and on its shifted version.	54

Figure 3.13 Comparison between the results of MSRF and FFT analyses for the interharmonics around the second harmonic component (1-s averaged RMS phase-A currents).	61
Figure 4.1 Comparison of the second harmonics produced by MSRF with Butterworth filter and Moving average filter in 200ms.	64
Figure 4.2 Flowchart of Kalman measurement and time update algorithms applied to positive- and negative-sequence components of all harmonics and interharmonics (k denotes the sampling index, where time step is $\Delta t = t_k - t_{k-1} = 40\mu s$).	69
Figure 4.3 Comparison of time delays in LPF blocks in Figures 2.10, 2.11, and 2.12 corresponding to Kalman- and Butterworth-filter. Subscripts K and B denote Kalman- and Butterworth-filter, respectively.	71
Figure 4.4 Response of the Kalman filter to a sudden jump.	72
Figure 4.5 Best practice of the design cycle for the application developers. . .	74
Figure 4.6 Generated code flowchart for MSRF algorithm implementation. . .	75
Figure 4.7 Coalesced memory access.	76
Figure 4.8 Race condition and synchronization techniques.	79
Figure 4.9 The system developed for the real-time detection of interharmonics and harmonics of AC EAFs on GPU framework.	81
Figure 4.10 Implementation of MSRF.	83
Figure 4.11 Comparison of actual and reconstructed (all harmonics and interharmonics with 5-Hz resolution are included up to 1.5kHz) line current sample waveforms.	85
Figure 4.12 Comparison of FFT results of actual and reconstructed line current waveforms during a typical tap-to-tap time.	86
Figure 4.13 10-cycle window FFT comparison of actual and 2 nd harmonic subgroup (obtained by MSRF analysis) subtracted actual line current waveforms.	87
Figure 4.14 10-cycle waveform of actual line current and filtered line current whose harmonic and interharmonic components between 65Hz and 675Hz are eliminated.	88

Figure 4.16 Comparison of FFT results of actual and compensated line current waveforms whose all harmonic and interharmonic components except the fundamental component subgroup are eliminated.	92
Figure 5.1 Detection of the power system fundamental frequency to update the speeds of the rotating reference frames in Figures 2.10, 2.11 and 2.12 (f_1 is the fundamental frequency of the power system).	94
Figure 5.2 Frequency variation of power system for one hour before the interconnection.	95
Figure 5.3 Persistency test results of second harmonic subgroup in phase-A.	96
Figure 5.4 P_{st} variations at 34.5 kV bus over a typical tap-to-tap time for case studies, i) there is no reactive power compensation or harmonic filtering, ii) reactive current components at fundamental frequency are fully compensated, iii) compensation is achieved according to the instantaneous-p-q theory, iv) interharmonics and harmonics are all eliminated, v) interharmonics, harmonics, and reactive current at supply frequency are all eliminated (EAF installation draws only the active current component at fundamental frequency from the 34.5 kV bus).	98

LIST OF ABBREVIATIONS

ABS	Asymmetrical Balanced Set
AC EAF	Alternating Current Electric Arc Furnaces
APF	Active Power Filters
AUS	Asymmetrical Unbalanced Set
BPF	Band Pass Filter
DAQ	Data Acquisition
DC	Direct Current
DFT	Discrete Fourier Transform
ESS	Energy Storage Systems
FFT	Fast Fourier Transform
GPU	Graphical Processing Unit
LF	Ladle Furnaces
LPF	Low Pass Filter
LV	Low Voltage
MSRF	Multiple Synchronous Reference Frame
MV	Medium Voltage
PCC	Point of Common Coupling
PLL	Phase Locked Loop
P_{lt}	Long-Term Flicker Severity
PQ	Power Quality
P_{st}	Short-Term Flicker Severity
RC	Resistor-Capacitor
RMS	Root-Mean-Square
SBS	Symmetrical Balanced Set
STATCOM	Synchronous Static Compensators
SUS	Symmetrical Unbalanced Set
SVC	Static VAr Compensation
TCR	Tyristor Controller Reactors

CHAPTER 1

INTRODUCTION

Alternating current electric arc furnaces (AC EAFs) are producers of currents with spectrums rich in interharmonics and harmonics owing to their operation principles, which in turn cause harmonic and interharmonic voltages and hence flicker at the point of common coupling (PCC). Therefore, fast and accurate determination of the spectral content of the current produced by an EAF is crucial in terms of both analyzing the harmonic and interharmonic contribution of an EAF load to the PCC and developing mitigation techniques against the undesired voltage spectrum production [3].

Various methods have been proposed in the literature for both harmonic and interharmonic analyses of current and voltage waveforms of the power systems [3–41]. The idea of using synchronous reference frames (SRFs) for the detection of sequence components of the harmonics is one of the well-known method and has been studied in various applications. A very common method for the detection of the speed of the synchronous frame that uses the benefits of the SRF decomposition is the use of phase-locked loops (PLLs) [4–10]. The PLL algorithm has been improved to extract the desired harmonic components from the original waveform by taking positive- and negative-sequence components into account in [9] and [10]. These methods, though convenient in time-varying conditions, are inapplicable in real-time fast response operations due to its heavy computational burden and cumulative phase lags. Attempts to optimize the performance of PLL-based methods have been summarized in [11]. Multiple synchronous reference frame (MSRF) analysis is one of the recent methods proposed to decompose the current or voltage waveforms into its harmonic

and also interharmonic components [3, 12, 13]. The use of multiple reference frames for selective harmonic compensation is proposed in [14]. MSRF strategy is used to compensate both positive- and negative-sequence components of the harmonics in [15], [16], [17] and [3]. The most important challenge of using MSRF analysis to effectively decompose the waveforms rich in harmonic and interharmonic content is the choice of the filtering method for decomposition. The fast and accurate response characteristics of the filter give the opportunity to decompose the waveform into its spectrum in real-time. Due to this reason, the use of moving average filters has been investigated to obtain faster and more accurate results for the computation of the fundamental positive sequence in [18] and adaptive notch filter has been proposed in [19] for selective harmonics and interharmonics decomposition. However, in a waveform having rapidly fluctuating harmonics and interharmonics content with comparable magnitudes such as the one in AC EAF, these filters do not give satisfactory results. Only in the proposed method in [3], a solution for this kind of load has been presented thoroughly, yet the method needs to be improved to be applicable in real-time operations.

Increasing attention is being paid to the estimation methods and adaptive filters with the increasing presence of highly distorted and unbalanced loads, and penetration of renewable energy sources to the PCC. For this reason, applications of Kalman filter have been proposed in various areas in [20–23]. In [20], conventional Kalman filter has been proposed for real-time harmonic tracking purpose, while in [21], Kalman filter has been improved to become more robust to the predicted filter parameters and to find a solution for Kalman’s synchronization problems in case of the abrupt changes. In [22], an extended Kalman filter algorithm which prevents the overflow of the time index and the estimation error has been implemented for decomposition of the current and/or voltage waveforms. However, none of them have a detailed study on interharmonic and hence flicker content of these waveforms. For real-time applications, a comparative analysis of the decomposition methods under distorted utility conditions has been carried out in [13] where the fast and accurate behaviors of conventional Kalman filter have been verified. Kalman filter-based approaches have also been preferred in different kind of application areas. For example, in [23], similar method has been proposed to detect the unbalanced voltage dips by the help of

positive- and negative- sequence voltages of the fundamental frequency, in [24], [25] flicker contribution has been predicted by the use of a Kalman filter-based approach. In spite of the many advanced properties of Kalman filter, neither of these proposed methods has offered a complete solution to the abrupt changes in amplitude and presence of comparable positive- and negative-sequence components of all harmonics and interharmonics components.

As to the interharmonic analysis, though not as popular as the harmonic analysis, various methods have been proposed since early 1990s [26–41]. Due to the fact that, there had been no limits for interharmonics recommended in any standard until new limits for interharmonic voltages were pronounced in [35] in July 2014, interharmonic analysis has received little attention in the regulations when compared to the harmonic analysis. However, since it is known that interharmonics and flicker relationship are intertwined, power quality (PQ) analysis of the EAF plants should also consider interharmonics, which commonly exist in the EAF and LF currents [27–29]. A comparative analysis has been given in [42] which can be a useful guide to determine the suitable methods for interharmonics detection.

In [27], a frequency-domain model has been proposed for determining only the harmonics of the EAF current in the existence of interharmonics and unbalances. In [30], usage of Fourier transform instead of Fourier series for interharmonic analysis is proposed, however, it is known that Fourier transform requires special attention for the reduction of spectral leakage in the actual case of oscillations in the power system frequency [31], [32], and it is not easy to reduce the interharmonic computation error to negligible rates in [36], migrating characteristics of interharmonics in the supply line current waveforms of medium frequency induction steel melting furnaces are described and modeled by considering these cases in [33]. Classification and modeling of various interharmonic sources have been described in detail based on the methods used for harmonic analysis in [34]. The most recent form of the IEC standard for computation methods of harmonics and interharmonics recommend usage of the groups and subgroups for interharmonic computation, which adopts the concept of total interharmonic effect for all interharmonic frequency components between two harmonics, instead of considering the individual interharmonic components [35]. Group interharmonic component takes the square root of the sum of squares of all the

interharmonic components using 5-Hz resolution discrete Fourier transform (DFT), while subgrouping neglects the effects of the interharmonic components closest to the harmonics in the same computation. On the other hand, this approach has been reported to suffer in [37] from leakage effect of the DFT, when interharmonics close to harmonics exist. Hence, Hui et al. [37] propose a frequency-domain method to improve the interharmonic grouping scheme adopted by IEC Standard 61000-4-7 [35].

It has been shown that, time-domain averaging and usage of difference filter in [38], space-vector DFT in [39], generalized delayed signal cancellation in [40] and most recently, Kalman filter and generalized averaging methods in [41] can be used for both harmonic and interharmonic detections in the framework of the IEC standards to improve the interharmonic computation accuracy, however, these works do not aim to resolve the amplitude and phase of each interharmonic. A detailed work on the sequences of interharmonics has been investigated for different cases such as variable frequency motor drives and motors with fluctuating mechanical loads in [43] and it has been concluded that interharmonics can have either positive or negative sequence and have rarely zero sequence component. However, in the published materials mentioned above, EAF is not considered as a case, where the generation of interharmonics is not systematic but rather stochastic, and hence both negative- and positive-sequence components of all interharmonics can exist at the same time.

The decomposition methods to calculate the harmonics and interharmonics content of the current and voltage waveforms are important, as well as the platform itself where these algorithms are implemented. Digital signal processors (DSPs) and field programmable gate arrays (FPGAs) are two commonly used hardware for this purpose. DSPs have been utilized to implement an adaptive PLL algorithm in [44] and [45], and to produce reference signal for the control system of an active power filter by pq-theory in [46] and by comb-filter-based method in [47]. On the other hand, the complexity of these methods demands high computational speed and parallel operation to allow advanced compensation system to take measures for the power quality problems. Therefore, FPGAs have become more popular and even compulsory [48] for the applications such as complex selected harmonic elimination techniques [49] and monitoring/decomposition methods [50], [51]. Nowadays, graphics processing units (GPUs) have become more popular which combine the benefits of FPGA and

CPU-based solutions offering enormous parallel computing power with micro second latency between input and output, and providing ease in development of complex algorithms at a reduced cost. GPUs have found place widely in image processing area, however there haven't been any suggested solutions regarding power system harmonics and interharmonics detection techniques implemented on GPU framework in the literature other than [52] and [53].

1.1 Problem Definition

Figure 1.1 shows a picture of a 135-MVA and 135-tonne AC EAF. The time-varying, nonlinear, and double-valued relationship between arc voltage and current makes an AC EAF one of the most problematic industrial loads for a power system. Due to the nature of the EAF operation, where carbon electrodes supplied from three phases are short-circuited through the scrap metal randomly in time, EAF current is time-varying and stochastic, causing noncharacteristic components of both positive- and negative-sequences of harmonics and also interharmonics. Therefore, the analysis of the EAF current spectrum deserves special care to resolve its harmonics and interharmonics. As in [3], typical characteristics of an AC EAF can be summarized as follows:

- i Rapidly fluctuating high active power demand in the range from a few tens to a few hundreds of MW,
- ii High reactive power demand resulting in operational power factors in the range from 0.65 to 0.8 pf lagging,
- iii Very rich in interharmonics content of the current waveforms in the medium voltage (MV) lines of the EAF transformer,
- iv Uncharacteristic power system even harmonics owing to the asymmetry of the positive and the negative half cycles of the current waveforms,
- v Usual characteristic power system odd harmonics,
- vi Light flicker arising from the modulation of fundamental frequency of the EAF bus voltage owing to the distortion caused by the interharmonic current components especially around the first and the second harmonics.



Figure 1.1: A 135-MVA, 135-tonne electric arc furnace, first melting cycle just after commissioning / by courtesy of NURSAN Iron and Steel Inc., Payas, Iskenderun, Turkey.

Interharmonic current components of AC EAF installations whose magnitudes are comparable with the harmonic current components may cause harmful effects on power system elements and neighboring industrial plant components. This is because conventional power systems contain transformers, overhead lines, cables, rotating electrical machines, line-commutated power electronic converters, and shunt-connected plain-capacitor or passive-filter banks tuned to the characteristic power system harmonics. For such systems only the characteristic current and voltage harmonics, whose frequencies are odd-integer multiples of the fundamental, are present as given in Table 1.1. Interharmonic currents injected by the AC EAF installation into the power system may cause generation of dangerous over-voltages or flow of over-currents at the tuning frequencies of the power system components as a result of parallel or series resonances.

On the other hand, huge amounts of reactive power consumed by an EAF installation causes significant drop in the voltage of supply bus to which the installation is con-

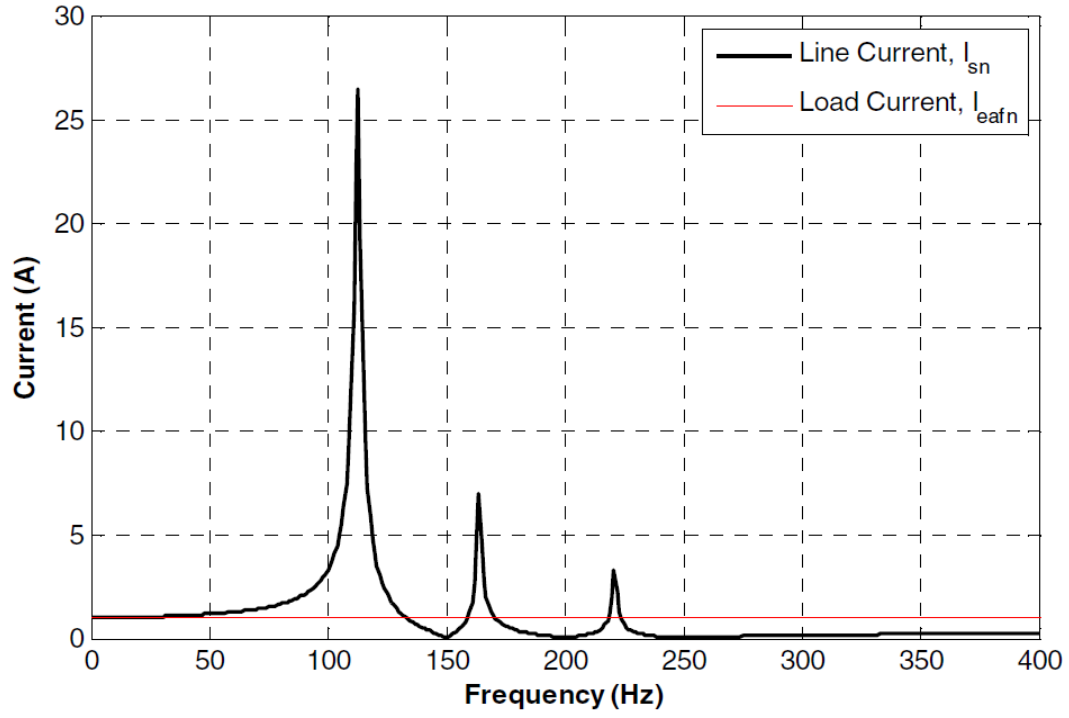
Table 1.1: Power System Harmonics.

3-phase, Sinusoidal Current Systems	Characteristic Harmonics	Uncharacteristic Harmonics
Positive-Sequence	$1^{st}, 7^{th}, 13^{th}, 19^{th}, \dots$	$4^{th}, 10^{th}, 16^{th}, 22^{nd}, \dots$
Negative-Sequence	$5^{th}, 11^{th}, 17^{th}, 23^{rd}, \dots$	$2^{nd}, 8^{th}, 14^{th}, 20^{th}, \dots$
Zero Sequence	$3^{rd}, 9^{th}, 15^{th}, 21^{st}, \dots$	$6^{th}, 12^{th}, 18^{th}, 24^{th}, \dots$

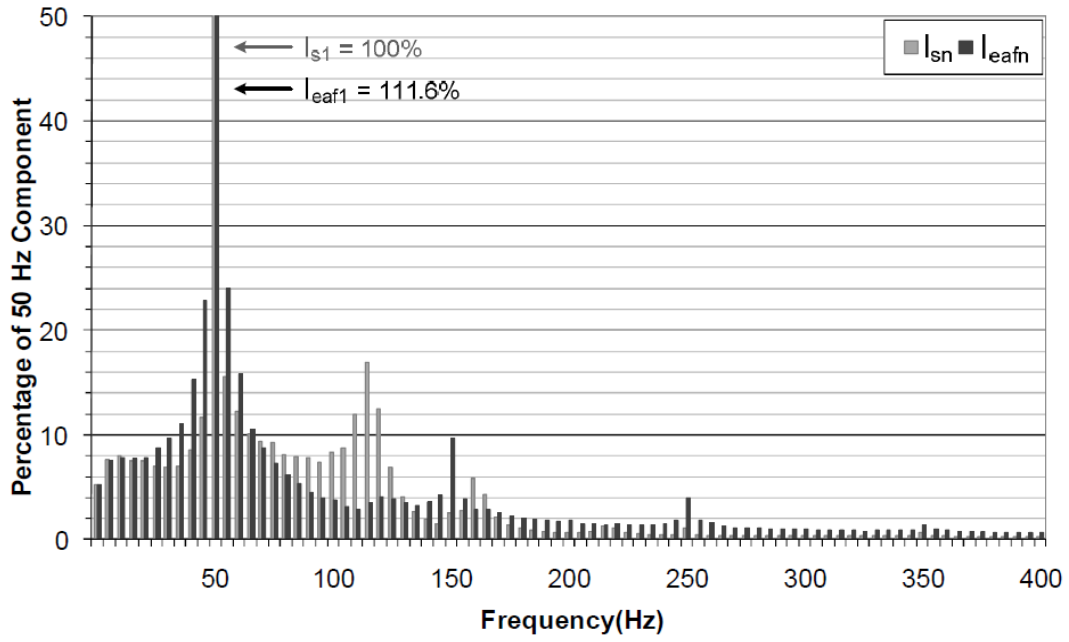
nected. Operation at a reduced voltage gives rise to lower amounts of heat that will be transferred to the crucible and hence a decline in the productivity of the steel melt shop.

In order to mitigate harmonics, interharmonics and huge amounts of reactive power demand, AC EAF installations in most of the iron and steel plants are equipped with SVC systems. These are composed of TCR and passive shunt harmonic filters tuned to some of the characteristic and/or uncharacteristic power system harmonics such as the 2^{nd} , 3^{rd} , 4^{th} , 5^{th} , 6^{th} , 7^{th} , and etc. Although these systems provide a good compensation of reactive power and suppression of the 3^{rd} and higher order harmonics, their light flicker suppression ability does not comply with tight short-term flicker severity (P_{st}) and long-term flicker severity (P_{lt}) limits [e.g. planning level of P_{st} should be less than or equal to 0.9 for MV level and compatibility level should be less than or equal to 1.0 for low voltage (LV)] specified in various standards [54, 55] and grid codes [56] especially for multi-EAF installations. Furthermore, field experience has shown that conventionally designed passive shunt harmonic filter topologies cause amplification of interharmonics around the fundamental and the 2^{nd} harmonic frequencies [2]. It has been summarized in [2] that there are basically three types of conventional passive shunt harmonic filter topologies utilized by the SVC manufacturers which are tuned to lower order harmonic frequencies such as 2^{nd} , 3^{rd} , 4^{th} and 5^{th} . It can be clearly seen from Figure 1.2 that these filters may cause the interharmonic currents to be amplified especially those between the 2^{nd} and the 3^{rd} instead of compensating them.

The limit values of even order uncharacteristic power system harmonics specified in standards and grid codes are also very tight. For example, maximum permissible value of the 2^{nd} current harmonic subgroup should not exceed 1% of maximum de-



(a) The overall frequency response of shunt filters tuned to 3rd, 4th and 5th harmonics.



(b) Harmonics and interharmonics content of AC EAF before (in black) and after (in grey) compensation by the above filter configuration.

Figure 1.2: The effects of the conventional passive shunt filters to the PCC. Figures taken from [2].

mand load current for the weakest grid. Unfortunately, in various standards [54, 55] and grid codes [56], maximum permissible values of only the characteristic (odd) and uncharacteristic (even) power system harmonics are recommended. Only in IEEE 2012 draft version of [55], maximum permissible values of interharmonic current components are recommended only for AC arc furnace installations [55]. In summary, voltage and hence light flicker and amplification of the 2nd harmonic subgroup are the major power quality problems of the AC EAFs when they are equipped with conventional SVC and passive shunt harmonic filter installations especially for multi-furnace operations.

To mitigate the PQ problems given above, more advanced technologies such as STATCOM [57, 58], semi-conventional C-type second harmonic filters [2] have been developed and installed in the field. Unfortunately, detailed information on the performance of STATCOM-based flicker mitigation systems and their control strategies are not available in the literature. On the other hand, the semi-conventional C-type harmonic filter in [2] prevents only the amplification of the interharmonics around the 2nd harmonic frequency.

Since the mentioned PQ problems of AC EAFs can only be solved by using advanced compensation technologies including active power filters (APFs), real-time detection and computation of the reactive current demand of, and the interharmonic and the harmonic current components injected by the AC EAF to the grid are essential tasks in the design and implementation of such advanced compensation systems. Several methods have been widely used to generate a reference current for the advanced-technology reactive power compensation and flicker compensation or active power filtering systems. In [59], some of these harmonic detection methods have been evaluated and compared to create a reference current for APFs. To achieve the same task, MSRF method has been proposed in [3], which also reveals the harmonic and interharmonic spectrum of the AC EAF. However, they have some common shortcomings which make these methods inefficient for the real-time operations. First of all, they suffer from phase lags of the filters appearing inside the range from several cycles to 10-cycles long. This latency is unacceptable since the harmonic and interharmonic content of an AC EAF change every cycle. However, it is compulsory to keep the cut-off frequency of the filters close to the desired frequency of the harmonics and the

interharmonics to obtain correct results since the interharmonic content (especially around the fundamental and the 2nd harmonic) of the load is high. Hence there is a trade-off between latency and the accuracy. As the cut-off frequency is kept closer to obtain more accurate decomposition, the latency increases and vice versa. In order to minimize this trade-off, the prediction capability of the Kalman filter has been utilized in this thesis to estimate the direct- and quadrature-axes components of all the harmonics and interharmonics with positive- and negative-sequence components obtained in the multiple reference frame analysis technique.

With the increase in the nonlinear and time-varying loads (such as AC EAFs, induction melting furnaces, and etc.), the harmonic and interharmonic contents of the PCC have increased and the methods previously developed have become no longer a solution for the compensation of these undesirable components. Therefore, decomposition algorithms have become more complex, adaptive and repetitive in order to obtain the correct spectrums of the PCCs to take suitable countermeasures which bring another challenge for real-time operations. DSPs can handle the computational burden of these algorithms, however they lack parallel processing capability which forces the sequential computation of the desired harmonics and interharmonics. Although the execution time of one content is quite short, there may be hundreds of different contents to compute if the frequency decomposition is achieved in 5-Hz resolution according to the IEC Standard [35] which results in an unacceptable response time. On the other hand, FPGAs and multi-core CPUs have been widely used in order to overcome this problem. Even if the CPUs have ease in programming and the parallel process capability, the execution time may differ from data sample to sample since the operating system may have some more important duties waiting on the queue. This causes CPU to have an unpredictable latency and brings the necessity to use a real-time operating system. Nevertheless CPUs have powerfull but not enough amount of cores to compute all the harmonics and interharmonics at the same time. FPGAs are more suitable for real-time complex algorithm implementations with parallel processing capability offering a microsecond-latency. Even if they seem to be a suitable choice to implement the algorithm proposed in this thesis, graphics processing unit (GPU) whose area of utilization is constantly increasing over the years has been preferred due to several reasons: GPUs combine the benefits of CPU- and FPGA-based

systems. They are easy to program, have precise execution time and have a comparable computational power to FPGAs with less expensive cost per unit. Especially with the integrated solutions NVIDIA offers (such as Jetson TK1 and TX1), they have become smaller, cheaper and more powerful at the same time. In order to overcome the above challenges, in this work, multiple synchronous reference frame (MSRF) analysis technique combined with Kalman prediction filter on GPU framework have been implemented to obtain the positive- and negative-sequence components of all harmonics and interharmonics of an AC EAF which will be described in detail in the forthcoming chapters.

1.2 Contributions

In this thesis, an MSRF analysis method introduced in [3] is developed to determine the sequence components of current harmonics and interharmonics produced by the AC EAF loads online. The balanced but asymmetrical characteristics of AC EAFs are usually not taken care of in the analysis procedures reported in the literature. The proposed method decomposes the frequency spectrum above the fundamental component of the EAF currents based on MSRF analysis inside a data window of one cycle of the harmonics and interharmonics, which is less than or equal to 20 ms, which is one tenth of the data window required for 5-Hz spectral resolution in the IEC Standard 61000-4-7 [26]. The window size increases for the subharmonics below the fundamental frequency due to the increasing period-length by the decreasing frequency, however it reaches to 20 ms only at 5 Hz. Therefore, the proposed method is suitable to be used with advanced-technology reactive power compensation and flicker compensation or active power filtering systems for the generation of the required reference current signals, where fast response from the frequency component amplitude and phase detection is required.

Additionally, the work presented in this thesis has led to the following publication in IEEE Transactions on Industry Applications:

- E. Uz-Logoglu, O. Salor, and M. Ermis. "Online characterization of interharmonics and harmonics of AC electric arc furnaces by multiple synchronous ref-

erence frame analysis." *Industry Applications, IEEE Transactions on*, 52(3):2673-2683, 2016.

- Also a second paper titled "Real-Time detection of interharmonics and harmonics of AC electric arc furnaces on GPU framework" is ready for submission.

1.3 Outline of the Thesis

The thesis is organized as follows; first of all, in Chapter 2, the categorization of three phase systems is given according to [1] and MSRF analysis is described to obtain the positive- and negative-sequence components of each harmonic and interharmonic component of a balanced but asymmetrical system. The improvement of the proposed algorithm is further detailed to have the ability to obtain the sequence components of unbalanced systems.

Next, the results of the proposed algorithm are given in Chapter 3 for several dominant harmonics and interharmonics. A brief matching performance comparison with the well known FFT algorithm is also provided to prove the validity and effectiveness of the algorithm.

In Chapter 4, two major challenges of the MSRF analysis will be given. First, the drawback of the low pass filters which prevents the proposed method to be used in real time systems is given. In order to increase the performance of the proposed method for real time systems, Kalman prediction filter which functions as a low pass filter is introduced. It is seen that Kalman filter not only helps to increase the speed of the filter response, but also it gives more accurate results for rapidly fluctuating waveforms. Second, the real-time determination of harmonics and interharmonics on GPU framework is explained in details. The advantages of the proposed architecture over the common methods in the extraction of power quality problems in real-time are detailed. It is shown that the fast and accurate nature of the GPU parallel computation capability is suitable to implement the proposed method. In the rest of this chapter, the possible application areas are presented. It has been shown that the proposed GPU framework based MSRF analysis can be used to suppress all harmonics and interharmonics significantly in an active power filter application in the power system.

Finally, the conclusions and the future work are stated in Chapter 5.

CHAPTER 2

MULTIPLE SYNCHRONOUS REFERENCE FRAME ANALYSIS

According to the classification proposed by [1], a three phase set in an electrical system can be divided into two subsets: The *symmetrical* set and the *asymmetrical* set. A three phase-set which can be represented by the equations in 2.1 is called symmetrical set when the magnitudes of each phase are equal to each other ($I_a = I_b = I_c$) and there is 120° or 0° phase difference between them at all times ($|\phi_a - \phi_b| = |\phi_b - \phi_c| = |\phi_c - \phi_a| = 120^\circ$ or 0°). In 2.1, I_a , I_b , and I_c represent magnitudes of the phases A, B, and C; w represents the angular frequency; and ϕ_a , ϕ_b , and ϕ_c represent the phase angles of the three phases. On the contrary, an asymmetrical set is defined when the set is not symmetrical which means that the magnitudes of phases are not equal to each other and/or the phase difference between any two phase is different than 120° or 0° . On the other hand, symmetrical and asymmetrical sets can be called *balanced* or *unbalanced* according to their algebraic sum at all time instants. If this sum is equal to zero, the three phase set is balanced, otherwise it is called unbalanced.

$$\begin{aligned}i_a(t) &= \sqrt{2}I_a \sin(wt + \phi_a) \\i_b(t) &= \sqrt{2}I_b \sin(wt + \phi_b) \\i_c(t) &= \sqrt{2}I_c \sin(wt + \phi_c)\end{aligned}\tag{2.1}$$

Fortescue in [60] proposed that given a set of three phase voltage or current waveforms whose amplitudes and phase information is arbitrary, it can be decomposed into three balanced and symmetrical sequence components, which are so called pos-

itive (the phase sequence of which is the same as the system under study), negative (the phase sequence of which is the reverse of the system under study) and zero sequence (the phase sequence of which is in phase with each other) as in Figure 2.1. The relation between three phase set with its sequence components are given in equation 2.2. In this equation, α stands for 120° rotation angle operator.

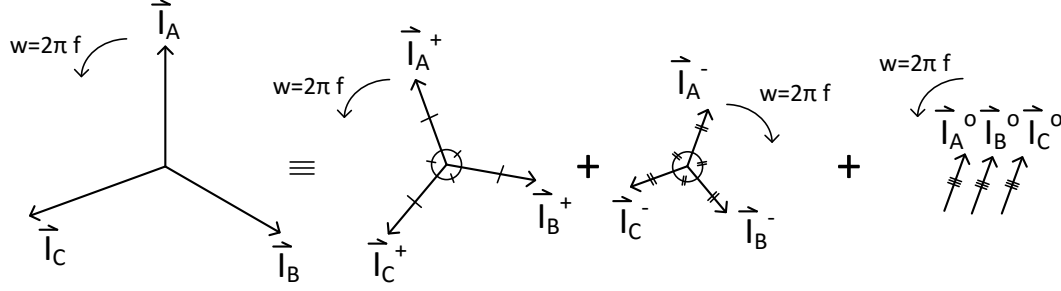


Figure 2.1: Positive- (I_A^+ , I_B^+ , I_C^+), negative- (I_A^- , I_B^- , I_C^-) and zero-sequence (I_A^o , I_B^o , I_C^o) decomposition of an arbitrary three-phase system.

$$\begin{bmatrix} I_a \\ I_b \\ I_c \end{bmatrix} = \overbrace{\begin{bmatrix} 1 & 1 & 1 \\ 1 & \alpha^2 & \alpha \\ 1 & \alpha & \alpha^2 \end{bmatrix}}^A \begin{bmatrix} I^o \\ I^+ \\ I^- \end{bmatrix} \Rightarrow I_{abc} = AI_{o+-} \quad (2.2)$$

Conversely, in order to obtain these balanced and symmetrical sets, three phase sets must be multiplied by the inverse of transformation matrix A given in 2.2 which is shown in 2.3. This conversion is very suitable for the equations especially containing the phasor representation of the phases.

$$A^{-1} = \frac{1}{3} \begin{bmatrix} 1 & 1 & 1 \\ 1 & \alpha & \alpha^2 \\ 1 & \alpha^2 & \alpha \end{bmatrix} \Rightarrow I_{o+-} = A^{-1}I_{abc} \quad (2.3)$$

[1] has summarized the categorization of three phase sets and their respective symmetrical sets by Table 2.1. Since the PQ-problematic loads such as AC EAFs are generally connected to the three-phase three-wire power system, asymmetrical balanced loads are of capital importance in this thesis. The most important result seen

from 2.1 is that both positive- and negative-sequences of all harmonics and interharmonics can be observed at the PCC when the load connected to this bus is classified as asymmetrical and balanced (ABS). The importance of this result comes from the fact that characteristic and uncharacteristic harmonics are assumed to be found in only one of the positive- and negative-sequences listed in Table 1.1 in the power system, hence the countermeasures are taken in order to compensate only the related symmetrical components. However, in this thesis, it is shown that both positive- and negative-sequence components have approximately the same importance for all harmonic and interharmonic components.

Table 2.1: Symmetrical components resulting from the respective three phase sets. Reconstructed from the figure in [1]. (SBS: symmetrical balanced set, SUS: symmetrical unbalanced set, ABS: asymmetrical balanced set, AUS: asymmetrical unbalanced set) Superscripts + and - represent positive- and negative-sequence components, respectively.

3-phase Sets	Type of the Symmetrical Components		
	Positive	Negative	Zero
SBS ⁺	✓		
SBS ⁻		✓	
SUS ^o			✓
ABS ^{+/-}	✓	✓	
AUS ^{+/-}	✓	✓	✓
AUS ^o	✓	✓	✓

In order to convert a three phase set into more convenient frames in time domain, Clarke's [61] (often referred as $\alpha\beta\gamma$ transformation) and Park's [62] (often referred as dqo transformation) transformations can be used. It should be noted that if the load under study is classified as balanced, neither γ nor o -components are observed after transformation which makes these transformations even more useful. Therefore, $\alpha\beta\gamma$ transformation can be considered as the projection of the phase quantities onto the stationary $\alpha\beta$ reference frame which are perpendicular to each other, whereas dqo transformation can be considered as the projection of the phase quantities onto the rotating dq reference frame which are perpendicular to each other as well. The referred transformations and their power invariant versions can be seen in the equations 2.4

and 2.5. One should be aware of the fact that the Park's transformation matrix and its power invariant version do not give the same result in case of the zero-sequence components. Park's transformation itself gives the same zero-sequence component with the Fortescue's symmetrical-component transformation [60]. On the other hand, the power invariant version of this transformation gives the o -component as $\sqrt{3}$ times the zero-sequence component of Fortescue's symmetrical-component transformation.

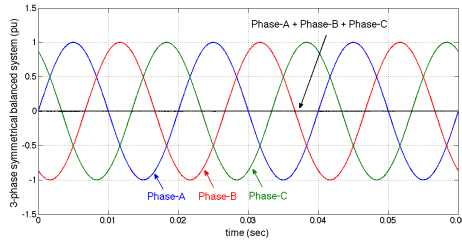
$$\begin{aligned}
& \text{Clarke's transformation matrix} \\
\begin{bmatrix} i_\alpha(t) \\ i_\beta(t) \\ i_\gamma(t) \end{bmatrix} &= \frac{2}{3} \begin{bmatrix} 1 & -\frac{1}{2} & -\frac{1}{2} \\ 0 & \frac{\sqrt{3}}{2} & -\frac{\sqrt{3}}{2} \\ \frac{1}{2} & \frac{1}{2} & \frac{1}{2} \end{bmatrix} \begin{bmatrix} i_a(t) \\ i_b(t) \\ i_c(t) \end{bmatrix} \\
& \text{Power invariant form of Clarke's transformation matrix} \\
\begin{bmatrix} i_\alpha(t) \\ i_\beta(t) \\ i_\gamma(t) \end{bmatrix} &= \sqrt{\frac{2}{3}} \begin{bmatrix} 1 & -\frac{1}{2} & -\frac{1}{2} \\ 0 & \frac{\sqrt{3}}{2} & -\frac{\sqrt{3}}{2} \\ \frac{1}{\sqrt{2}} & \frac{1}{\sqrt{2}} & \frac{1}{\sqrt{2}} \end{bmatrix} \begin{bmatrix} i_a(t) \\ i_b(t) \\ i_c(t) \end{bmatrix} \\
& \text{Park's transformation matrix} \\
\begin{bmatrix} i_d(t) \\ i_q(t) \\ i_o(t) \end{bmatrix} &= \frac{2}{3} \begin{bmatrix} \cos(\theta) & \cos(\theta - \frac{2\pi}{3}) & \cos(\theta + \frac{2\pi}{3}) \\ -\sin(\theta) & -\sin(\theta - \frac{2\pi}{3}) & -\sin(\theta + \frac{2\pi}{3}) \\ \frac{1}{2} & \frac{1}{2} & \frac{1}{2} \end{bmatrix} \begin{bmatrix} i_a(t) \\ i_b(t) \\ i_c(t) \end{bmatrix} \\
& \text{Power invariant form of Park's transformation matrix} \\
\begin{bmatrix} i_d(t) \\ i_q(t) \\ i_o(t) \end{bmatrix} &= \sqrt{\frac{2}{3}} \begin{bmatrix} \cos(\theta) & \cos(\theta - \frac{2\pi}{3}) & \cos(\theta + \frac{2\pi}{3}) \\ -\sin(\theta) & -\sin(\theta - \frac{2\pi}{3}) & -\sin(\theta + \frac{2\pi}{3}) \\ \frac{\sqrt{2}}{2} & \frac{\sqrt{2}}{2} & \frac{\sqrt{2}}{2} \end{bmatrix} \begin{bmatrix} i_a(t) \\ i_b(t) \\ i_c(t) \end{bmatrix}
\end{aligned} \tag{2.4}$$

$$\begin{aligned}
& \text{Park's transformation matrix} \\
\begin{bmatrix} i_d(t) \\ i_q(t) \\ i_o(t) \end{bmatrix} &= \frac{2}{3} \begin{bmatrix} \cos(\theta) & \cos(\theta - \frac{2\pi}{3}) & \cos(\theta + \frac{2\pi}{3}) \\ -\sin(\theta) & -\sin(\theta - \frac{2\pi}{3}) & -\sin(\theta + \frac{2\pi}{3}) \\ \frac{1}{2} & \frac{1}{2} & \frac{1}{2} \end{bmatrix} \begin{bmatrix} i_a(t) \\ i_b(t) \\ i_c(t) \end{bmatrix} \\
& \text{Power invariant form of Park's transformation matrix} \\
\begin{bmatrix} i_d(t) \\ i_q(t) \\ i_o(t) \end{bmatrix} &= \sqrt{\frac{2}{3}} \begin{bmatrix} \cos(\theta) & \cos(\theta - \frac{2\pi}{3}) & \cos(\theta + \frac{2\pi}{3}) \\ -\sin(\theta) & -\sin(\theta - \frac{2\pi}{3}) & -\sin(\theta + \frac{2\pi}{3}) \\ \frac{\sqrt{2}}{2} & \frac{\sqrt{2}}{2} & \frac{\sqrt{2}}{2} \end{bmatrix} \begin{bmatrix} i_a(t) \\ i_b(t) \\ i_c(t) \end{bmatrix}
\end{aligned} \tag{2.5}$$

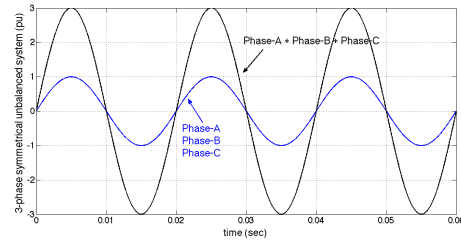
In this thesis, the dqo transformation has been used in order to calculate the symmetrical components which will be described in detail in Section 2.2. In order to give an idea about the relationship between dqo components and the type of the load, in other words, in order to comment on the results of this conversion depending on the load type, signal plots in Figure 2.2 have been obtained with synthetic data in MATLAB simulation environment. There are basically four different types of any load, which are symmetrical balanced, symmetrical unbalanced, asymmetrical balanced

and asymmetrical unbalanced. In each figure, there is a 60ms-long (which corresponds to 3 cycles in a 50Hz-electrical system and 50Hz is assumed to be the ideal fundamental frequency in this thesis) three-phase waveform with different types and the resulting dq -components by dqo transformation with 50Hz and -50Hz rotational speed for positive- and negative-sequence components respectively. In this thesis, little attention is paid to the o component since it does not exist in the load type under investigation (AC EAF load) which will be explained in detail Section 2.1. The two fundamental frequencies, 50Hz and -50Hz, have been chosen since dq transformation of both positive- and negative-sequence components will be investigated for each harmonic and interharmonic frequency. Results obtained by rotating the reference frame with positive 50Hz will result in the 50Hz-components carried to the zero frequency or DC. If there were any other components with different frequencies in the waveform (which means that if the waveform includes harmonics and/or interharmonics), they would have been obtained as AC components superposed on the DC component and fluctuating with the frequencies relative to the 50Hz. In other words, if the waveform included 100Hz component for example, this component would be transformed to 50Hz AC signal superposed on the top of DC component (which represents the magnitude of the positive 50Hz component) after dqo transformation with 50Hz rotation speed. Similarly, if the rotation speed is chosen to be negative 50Hz, then the 100Hz harmonic component would appear as 150Hz AC signal superimposed on the DC component which represents the magnitude of the negative 50Hz component inside the actual waveform.

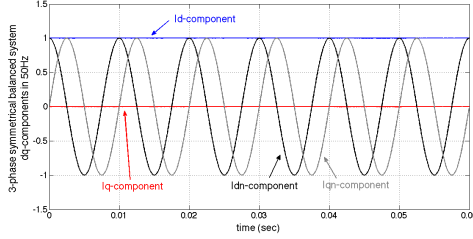
In Figure 2.2, two symmetrical sets one balanced and one unbalanced (SBS and SUS) have been investigated. I_d - and I_q -components represent the dq components resulting from the transformation with the speed of 50Hz. On the other hand, I_{dn} - and I_{qn} -components represent the dq components resulting from the transformation with the speed of -50Hz. As can be seen from Figure 2.2b, when the waveform includes only the fundamental positive-sequence (the phase sequence can be verified from Figure 2.2a), there isn't any q component and d component turns out to be a DC waveform with the magnitude of the fundamental positive-sequence component. If the rotation speed is reversed in the transformation (-50Hz), this time fundamental frequency component appears to be an AC-component with 100Hz frequency (relative



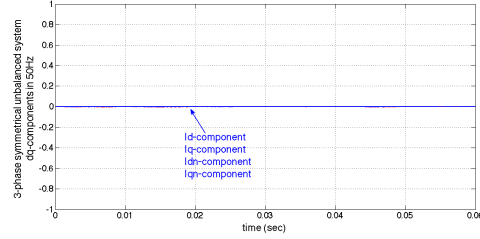
(a) Sample 3-phase SBS.



(c) Sample 3-phase SUS.



(b) dqo components of the waveforms in 2.2a.



(d) dqo components of the waveforms in 2.2c.

Figure 2.2: Relationship between the two different types of 3-phase symmetrical sets (SBS and SUS) and their dqo components. (I_d , I_q : dq components with 50Hz; I_{dn} , I_{qn} : dq components with -50Hz).

speed is 100Hz calculated by $(50\text{Hz} - (-50\text{Hz}))$ whose mean value is equal to zero and magnitude is equal to one. Since there isn't any negative sequence component inside the waveform, the resulting transformation includes no DC. dq components both give the same result with 90° phase difference as expected. Figure 2.2c illustrates a symmetrical unbalanced set. All three phases are in-phase with the same magnitude. The o component is present in this unbalanced load, which is equal to one third of the summation of all phases. This time, the dq transformation gives zero for each component rotated in 50Hz and -50Hz.

In Figure 2.3, two asymmetrical sets one balanced and one unbalanced (ABS and AUS) have been investigated. As can be seen from Figure 2.3b, when the load is asymmetrical (the different magnitude of each phase and phase differences different than 120° as given in Figure 2.3a), there is q component and d component at the same time whose mean values are different than zero. DC value of the d component represents the mean of the fundamental positive-sequence magnitudes, and DC value of the q component represents the mean of the discrepancies between the fundamental

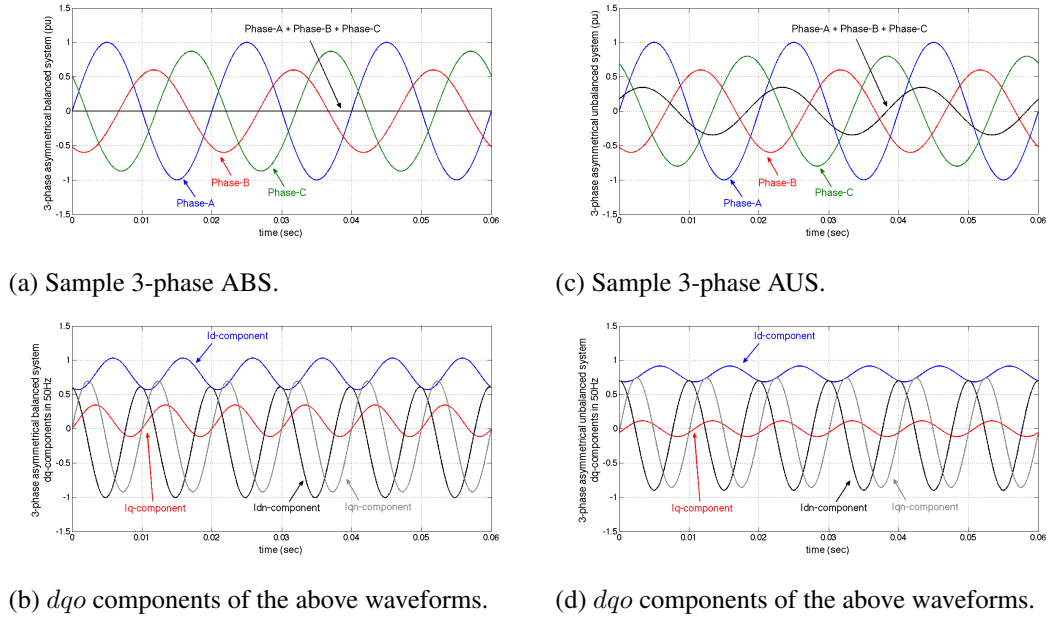


Figure 2.3: Relationship between two different types of 3-phase asymmetrical sets (ABS and AUS) and their dqo components. (I_d , I_q : dq components with 50Hz; I_{dn} , I_{qn} : dq components with -50Hz).

positive-sequence magnitudes. The frequency of the AC fluctuation on both rotating reference frame components is observed to be 100Hz referenced to the rotation angle which corresponds to 150Hz in real time. If the rotation speed is reversed in the transformation (-50Hz), this time fundamental frequency component appears as AC-component with 100Hz frequency (relative frequency is 100Hz, calculated by 50-(-50)Hz) whose mean value is not equal to zero representing the discrepancies of the phase angles. It is important to note that because the mean values of the I_{dn} and I_{qn} -components are nonzero values, hence the existence of the negative sequence component is obvious. Figure 2.3c illustrates the asymmetrical unbalanced set (AUS). Similar conclusions can be drawn by comparing Figures 2.3a and 2.3c.

2.1 Classification of the Problem

A typical power system for an AC EAF is as illustrated in Figure 2.4. All the measurements presented in this thesis were taken from the measurement point (MP) in Figure

2.4 which represents the primary side of the arc furnace transformer before the compensation system shown in the same figure. This installation can be considered as a balanced but asymmetrical three-phase load according to the classification provided in [1]. Since it constitutes a three-phase three-wire AC system with Δ -connected EAF transformer, there will be no zero sequence current theoretically on the MV side. Some odd cases which temporarily violate the balanced-load assumption can be described as given below.

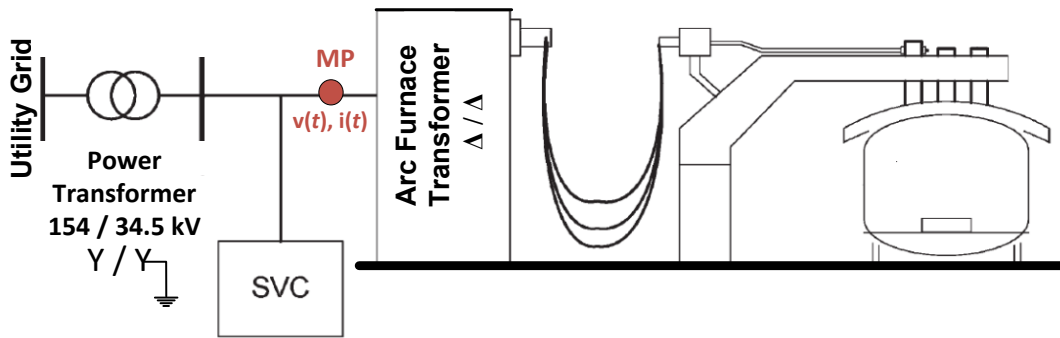


Figure 2.4: Illustration of the measurement point (MP), whose data is used in this thesis, in a typical transformer substation supplying the AC EAF.

Most of the AC EAF installations are switched on and off by using vacuum circuit breakers. Sudden interruption of EAF transformer current via vacuum circuit breaker causes generation of dangerous transient over voltages on the MV side of the EAF transformer. These are suppressed by RC snubber circuits and surge arresters mounted on the MV side of the EAF transformer. Furthermore, inrush currents flowing in the MV lines during the energization of EAF transformer are very rich in DC and second harmonic components. During energization and de-energization instants snubber circuit may act and cause flow of large unbalanced currents between grounding points of the snubber and MV side of the power transformer. The paths of the earth current is illustrated in Figure 2.5. According to the most common operation practice, the vacuum circuit breaker is frequently switched on and off for the purpose of charging the crucible, removing the slag and taking samples from the molten metal bath. Furthermore, when the electrode control system lifts one of the electrodes up

rapidly, current in that electrode is suddenly reduced or interrupted resulting in generation of high voltages on both sides of the EAF transformer. These voltages will then be suppressed by the surge capacitors connected to the LV side and the snubber circuit connected to the MV side of the EAF transformer resulting in flow of a larger current in usually two of the lines. Derivatives of phase currents together with the summation of the currents of all phases are shown in Figure 2.6 for a sample period of 40ms. For the vast majority of time, normal operation ($i_A(t) + i_B(t) + i_C(t) = 0$) takes place for which the maximum value of $\frac{di(t)}{dt} = 6.7 \times 10^2 \frac{kA}{s}$ for any of the three phases. However, as can be seen from Figure 2.6, the rate of variation of the current becomes $\frac{di}{dt} = -5.3 \times 10^3 \frac{kA}{s}$ during these unusual operating conditions which is ten times larger than the normal operation.

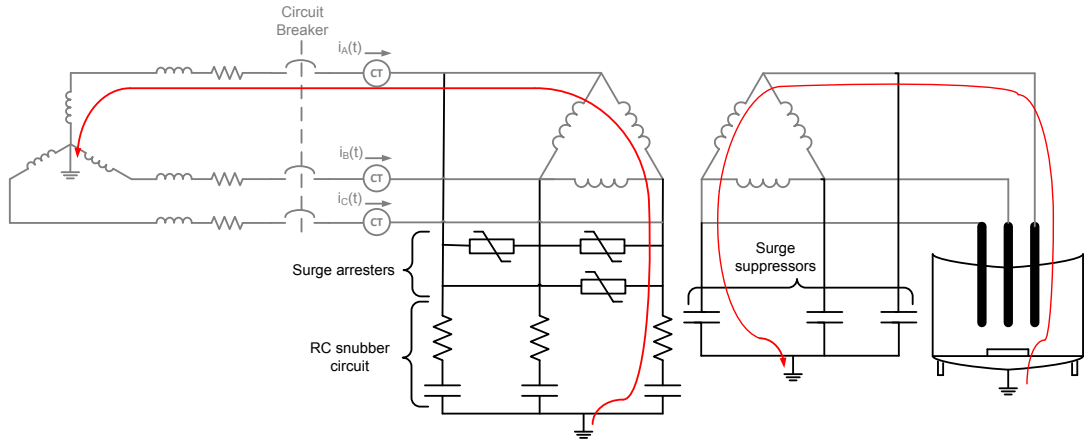


Figure 2.5: Earth current flow path due to the over-voltages on inductive elements during the energization and de-energization of the EAF transformer or sudden movement of one of the electrodes.

Figure 2.7 shows the summation of the instantaneous three phase line currents and Figure 2.8 shows the corresponding real power consumption of the plant in a tap-to-tap time which is approximately 55 mins. The times where the violation of the balanced circuit condition takes place can be clearly seen in this figure. It should be noted that, the operation of the protection devices coincides with the energization-of-the-transformer-period. However, in the vast majority of tap-to-tap time (in approximately all 55-min measurement period except for 3.3 seconds), the EAF installation operates as a three-phase balanced load, thus, satisfying equation 2.6. Therefore, it

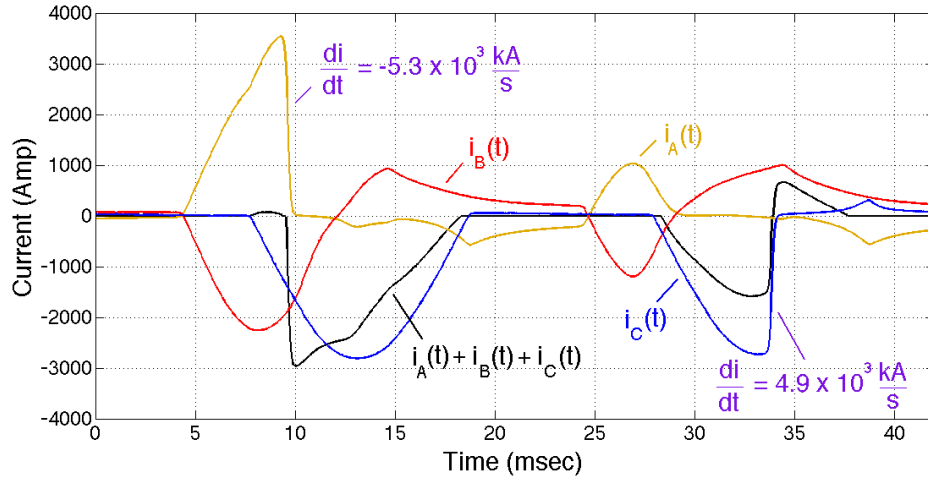


Figure 2.6: The rate of variation of the three-phase line current during abnormal operating conditions.

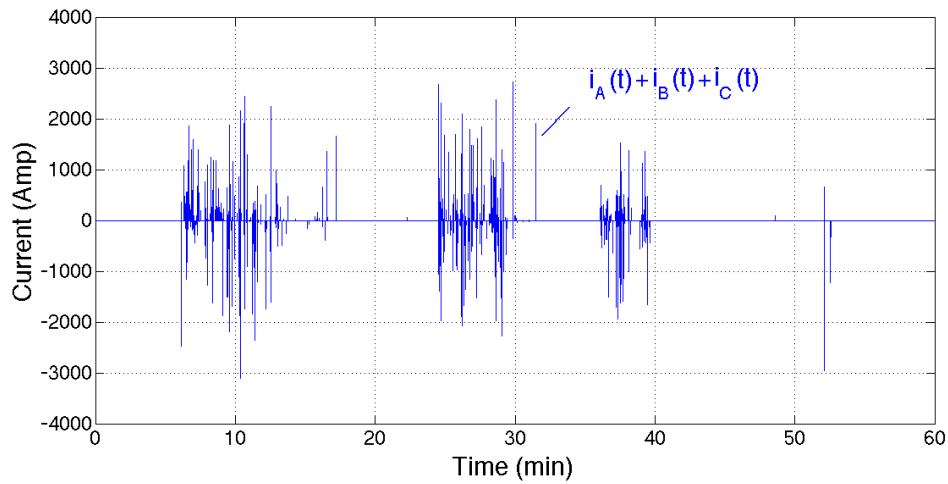


Figure 2.7: The sum of the instantaneous three-phase line currents of the AC EAF during a tap-to-tap time.

wouldn't be wrong to say that the AC EAF load is assumed to be balanced.

$$i_a(t) + i_b(t) + i_c(t) = 0. \quad (2.6)$$

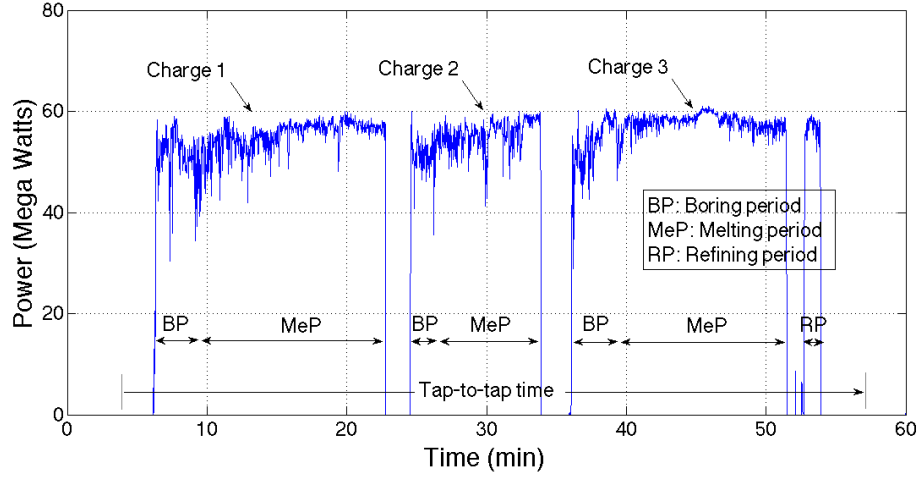


Figure 2.8: The instantaneous real power consumption of the AC EAF, with the corresponding charge periods.

2.2 Implementation of the Proposed Method

In this thesis, multiple synchronous reference frame (MSRF) analysis has been proposed in order to decompose the current and/or voltage waveform into its harmonic and interharmonic components with their respective symmetrical components. In the previous section, dqo method has been introduced to represent the three-phase signal in synchronous reference frame. In the synchronous reference frame, the frequencies other than the frequency of the rotating frame can be observed as AC components with the frequencies relative to the rotational speed. When the DC component is extracted among these waveforms by a simple low pass filter, the magnitude of these dqo -axes representing the harmonic or interharmonic component whose frequency is equal to the rotational speed of the reference frame is found. When the inverse transformation is applied to these DC components as in 2.7, time domain representation

of the harmonics and interharmonics can be obtained for each sample of the data.

$$\begin{aligned}
 \begin{bmatrix} i_a(t) \\ i_b(t) \\ i_c(t) \end{bmatrix} &= \overbrace{\begin{bmatrix} \cos(\theta) & -\sin(\theta) & 1 \\ \cos(\theta - \frac{2\pi}{3}) & -\sin(\theta - \frac{2\pi}{3}) & 1 \\ \cos(\theta + \frac{2\pi}{3}) & -\sin(\theta + \frac{2\pi}{3}) & 1 \end{bmatrix}}^{\text{Inverse Park's transformation matrix}} \begin{bmatrix} i_d(t) \\ i_q(t) \\ i_o(t) \end{bmatrix} \\
 &\quad \text{Power invariant form of inverse Park's transformation matrix} \\
 \begin{bmatrix} i_a(t) \\ i_b(t) \\ i_c(t) \end{bmatrix} &= \sqrt{\frac{2}{3}} \overbrace{\begin{bmatrix} \cos(\theta) & -\sin(\theta) & \frac{\sqrt{2}}{2} \\ \cos(\theta - \frac{2\pi}{3}) & -\sin(\theta - \frac{2\pi}{3}) & \frac{\sqrt{2}}{2} \\ \cos(\theta + \frac{2\pi}{3}) & -\sin(\theta + \frac{2\pi}{3}) & \frac{\sqrt{2}}{2} \end{bmatrix}}^{\text{Power invariant form of inverse Park's transformation matrix}} \begin{bmatrix} i_d(t) \\ i_q(t) \\ i_o(t) \end{bmatrix}
 \end{aligned} \tag{2.7}$$

In this section, block diagram representation of the proposed methods for balanced and unbalanced systems will be described in details. Mathematical derivation of the proposed method applicable to the unbalanced three phase system will be given. There are some challenges in the application of this method in real-time which will be described in Chapter 3. To overcome these challenges, novel solutions will be introduced in Chapter 4.

2.2.1 Asymmetrical Balanced Three-Phase Current System

The asymmetrical three-phase balanced current system of the EAF installation can be resolved into two three-phase balanced and symmetrical current systems, the so called positive-sequence and negative-sequence systems as given in Figure 2.9, where f is the corresponding frequency component.

Online application of the MSRF analysis in the field requires measuring the line currents and voltages on the MV side of the EAF transformer continuously and synchronously at a sampling rate of at least 5 kHz per channel to satisfy the Nyquist sampling frequency to monitor up to the 50th harmonic in the 50Hz system according to the IEC Standard 61000-4-7 [35]. The data employed in MSRF analysis in this paper is sampled at a sampling rate of 25.6 kHz per channel on the MV side of a 65 MVA EAF transformer by using the multi-purpose platform described in [63] and operating it in the *Raw Data Collection mode*.

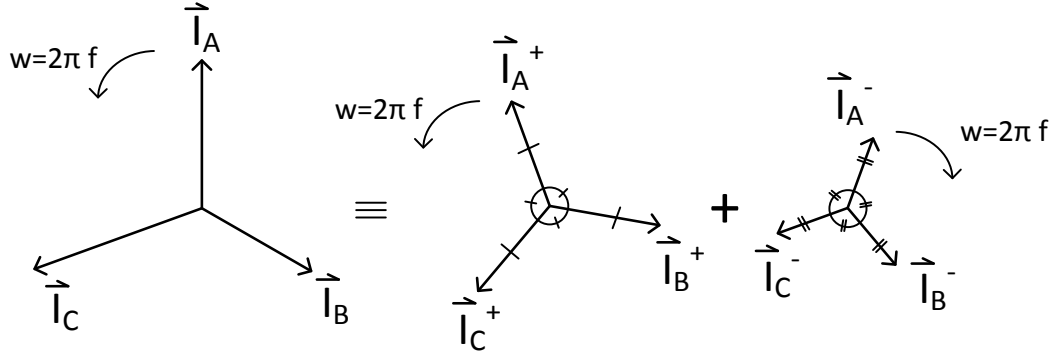


Figure 2.9: Positive- and negative-sequence decomposition for an asymmetrical and balanced three-phase system.

MSRF algorithm presented in this paper is summarized in Figures 2.10, 2.11 and 2.12. In the first step of the calculations, DC component of each phase is subtracted from the associated actual current waveform as illustrated in Figure 2.10. DC component is calculated as the mean value over each cycle of the fundamental current. Then positive- and negative-sequence components of the fundamental current are obtained from the DC subtracted currents, $\tilde{i}_A(t)$, $\tilde{i}_B(t)$, and $\tilde{i}_C(t)$ by rotating the Synchronous Reference Frame (SRF) at a speed of $2\pi f_1$ in both directions, where fundamental frequency $f_1 = 50$ Hz in our applications. The SRF yields AC components superimposed on the DC component corresponding to either positive-sequence or the negative-sequence of the fundamental current. The DC component is extracted by a LPF. Phase response of the LPF is compensated to be zero at all frequencies. The actual positive-sequence ($i_{A1}^+(t)$, $i_{B1}^+(t)$, $i_{C1}^+(t)$) and the negative-sequence ($i_{A1}^-(t)$, $i_{B1}^-(t)$, $i_{C1}^-(t)$) current waveforms are then obtained by inverse transformations as shown in Figure 2.10. The fundamental components of line current waveforms are deduced by summing up the positive-sequence and the negative-sequence components sample-by-sample in time. Note that the subscript 1 refers to the fundamental frequency component in Figure 2.10.

Since the amplitudes of fundamental line currents are much higher than those of interharmonics and harmonics, fundamental line current components ($i_{A1}^+(t) + i_{A1}^-(t)$, $i_{B1}^+(t) + i_{B1}^-(t)$, and $i_{C1}^+(t) + i_{C1}^-(t)$) should be subtracted from the zero-DC current waveforms ($\tilde{i}_A(t)$, $\tilde{i}_B(t)$, and $\tilde{i}_C(t)$) before proceeding further for the harmonics and

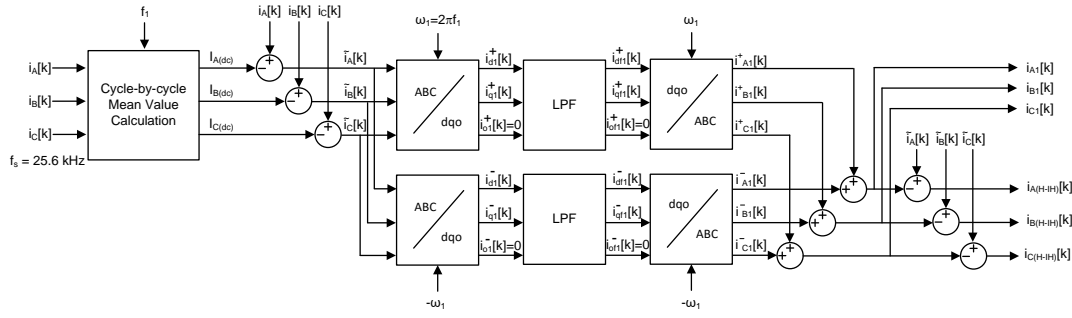


Figure 2.10: Online extraction of direct current and fundamental current components (both positive- and negative-sequence) from the actual three phase line current wave-forms sampled at a rate of 25.6 kHz/channel in the field.

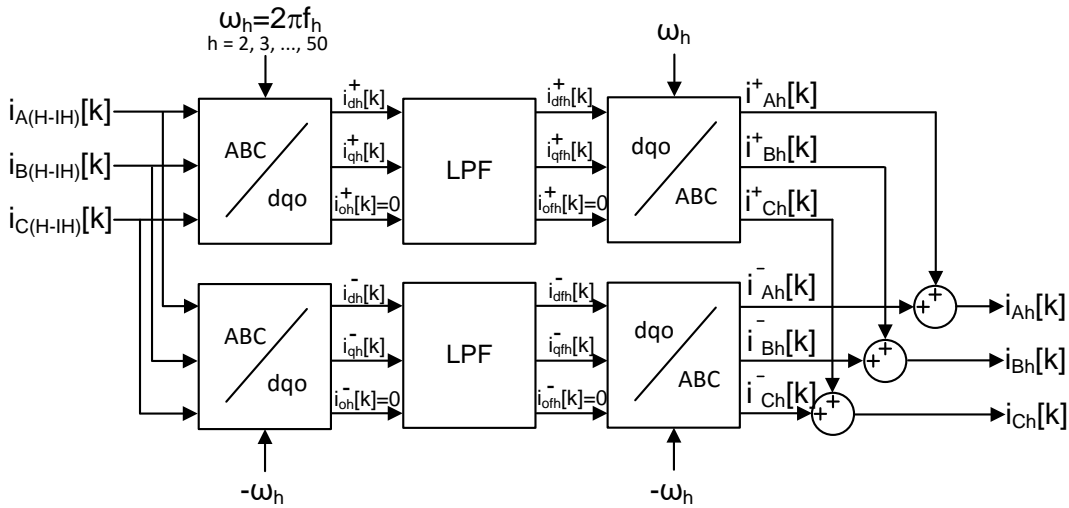


Figure 2.11: Online extraction of line current harmonic components (both positive- and negative-sequence) by MSRF analysis.

interharmonics analysis. Harmonic and interharmonic current components will then be obtained from the current waveforms, $i_{A(H-IH)}(t)$, $i_{B(H-IH)}(t)$ and $i_{C(H-IH)}(t)$ which represent all frequency components except for the fundamental. The subscript $H-IH$ stands for harmonics and interharmonics.

Figure 2.11 illustrates the computation of positive- ($i_{Ah}^+(t)$, $i_{Bh}^+(t)$, $i_{Ch}^+(t)$) and negative-sequence ($i_{Ah}^-(t)$, $i_{Bh}^-(t)$, $i_{Ch}^-(t)$) harmonic components of the current where subscript h represents the harmonic number. Similarly, in Figure 2.12, computation of the

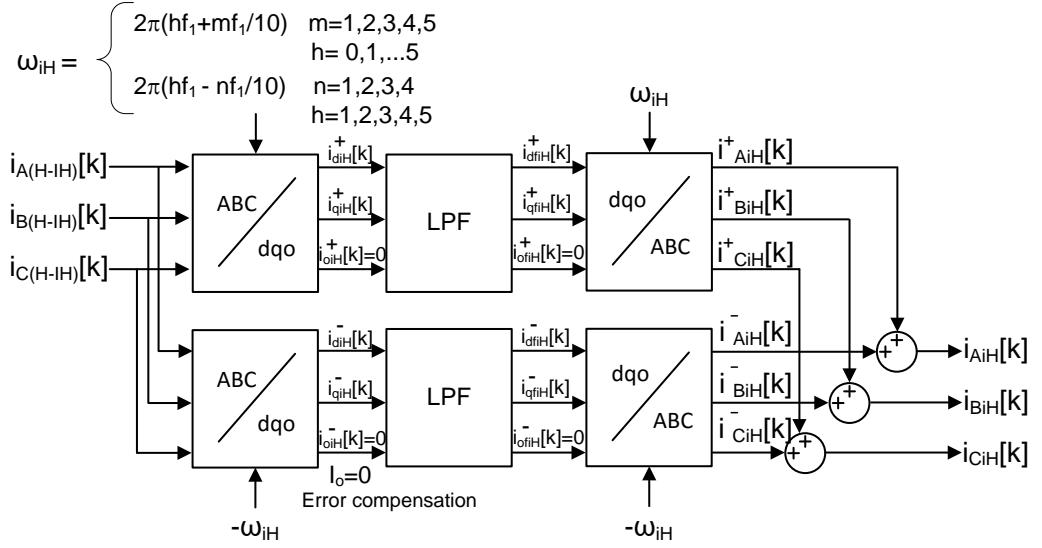


Figure 2.12: Online extraction of interharmonic current components with 5-Hz resolution (both positive- and negative-sequence) by MSRF analysis. w_{iH} represents the interharmonic frequencies and f_1 is the fundamental frequency.

positive- ($i_{AiH}^+(t)$, $i_{BiH}^+(t)$, $i_{CiH}^+(t)$) and negative-sequence ($i_{AiH}^-(t)$, $i_{BiH}^-(t)$, $i_{CiH}^-(t)$) components of the interharmonic current waveforms is illustrated. Interharmonic analysis is carried out as multiples of 5 Hz as explained by w_{iH} in Figure 2.12. This is to make the results comparable with the Fourier analysis results, whose resolution is 5 Hz owing to the 10-cycle DFT analysis recommendation of the IEC Standard 61000-4-7 [35]. In Chapter 3), harmonic and interharmonic current waveforms are computed consecutively from field data in MATLAB computing environment.

Note that in Figures 2.10, 2.11 and 2.12, o -components are all equated to zero since EAF is assumed to be an ABS for more than 99% of the operation time. That is why equating the o -component is called error compensation. If o -component is not exactly equal to zero, this is assumed to be due to the reading error of the measurement transformers. The results of the harmonic and interharmonic analyses using the MSRF are compared with the Fourier analysis results for verification of the developed spectrum analysis method in Chapter 3.

2.2.2 Asymmetrical Unbalanced Three-Phase Current System

As described in the previous sections, an asymmetrical unbalanced set (AUS) can be represented by three symmetrical sets as shown in Figure 2.1. In order to decompose this kind of a set into its harmonic and interharmonic components, all three symmetrical components need to be considered for every frequency under consideration. Asymmetrical balanced three phase set is a special case of the AUS whose o -component is equal to zero. Therefore only two unknowns have been introduced for each analysis as described in the previous section which makes the calculations easier. Since usually the researches have been held on balanced sets, there is not much information about asymmetrical unbalanced sets in the literature. However, this kind of loads may exist in every four wire system, and loads such as AC EAFs whose protection devices operate most of the time in a typical tap-to-tap time can be considered as asymmetrical unbalanced load even if it is connected to a 3-wire electrical system. Therefore, these kind of loads (AUS) should be represented by global equations whose derivation will be started with the most generic three-phase current/voltage waveform representation whose amplitude and phase difference are not equal to each other as shown in 2.8. Here, the amplitudes of the three phases are all different ($A \neq B \neq C$) and the phase differences are different than 120° by ϵ_B and ϵ_C . The frequency, f_A , in equations 2.8 is the same for all phases and it represents only one of the frequency component inside $x_A(t)$ to make the following derivations simpler. Similarly ϕ_A represents the phase of Phase-A with respect to the data analysis window. The summation of the three phase waveforms are not necessarily equal to zero in this unbalanced case.

In the equations 2.8 to 2.12, f is the frequency under consideration and the transformation is applied to get the positive-sequence d -component corresponding to f . The superscript LP represents the low-pass-filtered waveform whereas BPF represents the band-pass-filtered waveform in equations 2.9 to 2.13, therefore those equations hold only if the frequency f_A is so close to f that frequency component at their difference, $f_A - f$, can pass through a sharp LPF whose cut-off frequency is at 2.5 Hz. $\tilde{x}_A(t)$ represents the calculated phase component of the related harmonic or interharmonic, whose frequency is closest to f for phase-A. The next step is to apply the back

transformation 2.14 to 2.21 in order to obtain the time-domain representation of each phase for frequency closest to f . Equations below introduce the overall procedure.

$$\begin{aligned}x_A(t) &= A \sin(2\pi f_A t + \phi_A) \\x_B(t) &= B \sin(2\pi f_A t + \phi_A - 2\pi/3 + \epsilon_B) \\x_C(t) &= C \sin(2\pi f_A t + \phi_A + 2\pi/3 + \epsilon_C)\end{aligned}\tag{2.8}$$

First, the positive-sequence of d -component is obtained by applying the transformation matrix as shown in 2.9. Note that the power invariant version of the Park's transformation has been used to calculate all the components.

Then the positive-sequence of q -component is obtained as shown in equation 2.10.

The same method is applied in order to find the negative-sequences with a small difference. This time the frequency under consideration is chosen to be negative as can be seen in 2.11 and 2.12.

$$\begin{aligned}x_D^+(t) &= \sqrt{\frac{2}{3}} A \sin(2\pi f_A t + \phi_A) \cos(2\pi f t) \\&+ \sqrt{\frac{2}{3}} B \sin(2\pi f_A t + \phi_A - 2\pi/3 + \epsilon_B) \cos(2\pi f t - 2\pi/3) \\&+ \sqrt{\frac{2}{3}} C \sin(2\pi f_A t + \phi_A + 2\pi/3 + \epsilon_C) \cos(2\pi f t + 2\pi/3) \\x_D^+(t) &= \sqrt{\frac{2}{3}} \frac{A}{2} \{ \sin(2\pi(f_A + f)t + \phi_A) + \sin(2\pi(f_A - f)t + \phi_A) \} \\&+ \sqrt{\frac{2}{3}} \frac{B}{2} \{ \sin(2\pi(f_A + f)t + \phi_A - 4\pi/3 + \epsilon_B) + \sin(2\pi(f_A - f)t + \phi_A + \epsilon_B) \} \\&+ \sqrt{\frac{2}{3}} \frac{C}{2} \{ \sin(2\pi(f_A + f)t + \phi_A + 4\pi/3 + \epsilon_C) + \sin(2\pi(f_A - f)t + \phi_A + \epsilon_C) \} \\x_D^{LP+}(t) &= \sqrt{\frac{2}{3}} \frac{A}{2} \sin(2\pi(f_A - f)t + \phi_A) \\&+ \sqrt{\frac{2}{3}} \frac{B}{2} \sin(2\pi(f_A - f)t + \phi_A + \epsilon_B) \\&+ \sqrt{\frac{2}{3}} \frac{C}{2} \sin(2\pi(f_A - f)t + \phi_A + \epsilon_C)\end{aligned}\tag{2.9}$$

$$\begin{aligned}
x_Q^+(t) &= \sqrt{\frac{2}{3}} A \sin(2\pi f_A t + \phi_A) - \sin(2\pi f t) \\
&+ \sqrt{\frac{2}{3}} B \sin(2\pi f_A t + \phi_A - 2\pi/3 + \epsilon_B) - \sin(2\pi f t - 2\pi/3) \\
&+ \sqrt{\frac{2}{3}} C \sin(2\pi f_A t + \phi_A + 2\pi/3 + \epsilon_C) - \sin(2\pi f t + 2\pi/3) \\
x_Q^+(t) &= -\sqrt{\frac{2}{3}} \frac{A}{2} \{ \cos(2\pi(f_A - f)t + \phi_A) - \cos(2\pi(f_A + f)t + \phi_A) \} \\
&- \sqrt{\frac{2}{3}} \frac{B}{2} \{ \cos(2\pi(f_A - f)t + \phi_A + \epsilon_B) - \cos(2\pi(f_A + f)t + \phi_A - 4\pi/3 + \epsilon_B) \} \\
&- \sqrt{\frac{2}{3}} \frac{C}{2} \{ \cos(2\pi(f_A - f)t + \phi_A + \epsilon_C) - \cos(2\pi(f_A + f)t + \phi_A + 4\pi/3 + \epsilon_C) \} \\
x_Q^{LP+}(t) &= -\sqrt{\frac{2}{3}} \frac{A}{2} \cos(2\pi(f_A - f)t + \phi_A) \\
&- \sqrt{\frac{2}{3}} \frac{B}{2} \cos(2\pi(f_A - f)t + \phi_A + \epsilon_B) \\
&- \sqrt{\frac{2}{3}} \frac{C}{2} \cos(2\pi(f_A - f)t + \phi_A + \epsilon_C)
\end{aligned} \tag{2.10}$$

$$\begin{aligned}
x_D^-(t) &= \sqrt{\frac{2}{3}} A \sin(2\pi f_A t + \phi_A) \cos(-2\pi f t) \\
&+ \sqrt{\frac{2}{3}} B \sin(2\pi f_A t + \phi_A - 2\pi/3 + \epsilon_B) \cos(-2\pi f t - 2\pi/3) \\
&+ \sqrt{\frac{2}{3}} C \sin(2\pi f_A t + \phi_A + 2\pi/3 + \epsilon_C) \cos(-2\pi f t + 2\pi/3) \\
x_D^-(t) &= \sqrt{\frac{2}{3}} \frac{A}{2} \{ \sin(2\pi(f_A + f)t + \phi_A) + \sin(2\pi(f_A - f)t + \phi_A) \} \\
&+ \sqrt{\frac{2}{3}} \frac{B}{2} \{ \sin(2\pi(f_A + f)t + \phi_A + \epsilon_B) + \sin(2\pi(f_A - f)t + \phi_A - 4\pi/3 + \epsilon_B) \} \\
&+ \sqrt{\frac{2}{3}} \frac{C}{2} \{ \sin(2\pi(f_A + f)t + \phi_A + \epsilon_C) + \sin(2\pi(f_A - f)t + \phi_A + 4\pi/3 + \epsilon_C) \} \\
x_D^{LP-}(t) &= \sqrt{\frac{2}{3}} \frac{A}{2} \sin(2\pi(f_A - f)t + \phi_A) \\
&+ \sqrt{\frac{2}{3}} \frac{B}{2} \sin(2\pi(f_A - f)t + \phi_A - 4\pi/3 + \epsilon_B) \\
&+ \sqrt{\frac{2}{3}} \frac{C}{2} \sin(2\pi(f_A - f)t + \phi_A + 4\pi/3 + \epsilon_C)
\end{aligned} \tag{2.11}$$

$$\begin{aligned}
x_Q^-(t) &= \sqrt{\frac{2}{3}}A \sin(2\pi f_A t + \phi_A) - \sin(-2\pi f t) \\
&+ \sqrt{\frac{2}{3}}B \sin(2\pi f_A t + \phi_A - 2\pi/3 + \epsilon_B) - \sin(-2\pi f t - 2\pi/3) \\
&+ \sqrt{\frac{2}{3}}C \sin(2\pi f_A t + \phi_A + 2\pi/3 + \epsilon_C) - \sin(-2\pi f t + 2\pi/3) \\
x_Q^-(t) &= -\sqrt{\frac{2}{3}}\frac{A}{2} \{ \cos(2\pi(f_A - f)t + \phi_A) - \cos(2\pi(f_A + f)t + \phi_A) \} \\
&+ \sqrt{\frac{2}{3}}\frac{B}{2} \{ \cos(2\pi(f_A - f)t + \phi_A - 4\pi/3 + \epsilon_B) - \cos(2\pi(f_A + f)t + \phi_A + \epsilon_B) \} \\
&+ \sqrt{\frac{2}{3}}\frac{C}{2} \{ \cos(2\pi(f_A - f)t + \phi_A + 4\pi/3 + \epsilon_C) - \cos(2\pi(f_A + f)t + \phi_A + \epsilon_C) \} \\
x_Q^{LP-}(t) &= -\sqrt{\frac{2}{3}}\frac{A}{2} \cos(2\pi(f_A - f)t + \phi_A) \\
&+ \sqrt{\frac{2}{3}}\frac{B}{2} \cos(2\pi(f_A - f)t + \phi_A - 4\pi/3 + \epsilon_B) \\
&+ \sqrt{\frac{2}{3}}\frac{C}{2} \cos(2\pi(f_A - f)t + \phi_A + 4\pi/3 + \epsilon_C)
\end{aligned} \tag{2.12}$$

Calculation of the zero component is fairly straightforward as in 2.13.

$$\begin{aligned}
x_O(t) &= \frac{1}{\sqrt{3}}A \sin(2\pi f_A t + \phi_A) \\
&+ \frac{1}{\sqrt{3}}B \sin(2\pi f_A t + \phi_A - 2\pi/3 + \epsilon_B) \\
&+ \frac{1}{\sqrt{3}}C \sin(2\pi f_A t + \phi_A + 2\pi/3 + \epsilon_C) \\
x_O^{BPF}(t) &= \frac{1}{\sqrt{3}}A \sin(2\pi f_A t + \phi_A) \\
&+ \frac{1}{\sqrt{3}}B \sin(2\pi f_A t + \phi_A - 2\pi/3 + \epsilon_B) \\
&+ \frac{1}{\sqrt{3}}C \sin(2\pi f_A t + \phi_A + 2\pi/3 + \epsilon_C)
\end{aligned} \tag{2.13}$$

The BPF in equation 2.13 is adjusted to filter out only the frequency of interest in the computations which is f . Here f_A is assumed to be very close to f . Positive sequence phase-A current is obtained by multiplying the positive-sequence d - and q -

components with the back transformation matrix (inverse Park's transformation matrix) as in 2.14. The details of the derivations can be followed from Equations 2.15, 2.16 and 2.17. Some cancellations are held in order to simplify the equations.

$$\widetilde{x}_A^+(t) = \sqrt{\frac{2}{3}} \{x_D^{LP+}(t) \cos(2\pi ft) - x_Q^{LP+}(t) \sin(2\pi ft)\} \quad (2.14)$$

$$\begin{aligned} \widetilde{x}_A^+(t) = \frac{1}{2} \sqrt{\frac{2}{3}} \sqrt{\frac{2}{3}} \{ & A \sin(2\pi(f_A - f)t + \phi_A) \cdot \cos(2\pi ft) \\ & + B \sin(2\pi(f_A - f)t + \phi_A + \epsilon_B) \cdot \cos(2\pi ft) \\ & + C \sin(2\pi(f_A - f)t + \phi_A + \epsilon_C) \cdot \cos(2\pi ft) \\ & + A \cos(2\pi(f_A - f)t + \phi_A) \cdot \sin(2\pi ft) \\ & + B \cos(2\pi(f_A - f)t + \phi_A + \epsilon_B) \cdot \sin(2\pi ft) \\ & + C \cos(2\pi(f_A - f)t + \phi_A + \epsilon_C) \cdot \sin(2\pi ft) \} \end{aligned} \quad (2.15)$$

$$\begin{aligned} \widetilde{x}_A^+(t) = \frac{1}{6} \{ & A[\sin(2\pi ft + \phi_A) + \sin(2\pi(f_A - 2f)t + \phi_A)] \\ & + B[\sin(2\pi f_A t + \phi_A + \epsilon_B) + \sin(2\pi(f_A - 2f)t + \phi_A + \epsilon_B)] \\ & + C[\sin(2\pi f_A t + \phi_A + \epsilon_C) + \sin(2\pi(f_A - 2f)t + \phi_A + \epsilon_C)] \\ & + A[\sin(2\pi f_A t + \phi_A) - \sin(2\pi(f_A - 2f)t + \phi_A)] \\ & + B[\sin(2\pi f_A t + \phi_A + \epsilon_B) - \sin(2\pi(f_A - 2f)t + \phi_A + \epsilon_B)] \\ & + C[\sin(2\pi f_A t + \phi_A + \epsilon_C) - \sin(2\pi(f_A - 2f)t + \phi_A + \epsilon_C)] \} \end{aligned} \quad (2.16)$$

$$\begin{aligned} \widetilde{x}_A^+(t) = \frac{1}{3} \{ & A \sin(2\pi f_A t + \phi_A) \\ & + B \sin(2\pi f_A t + \phi_A + \epsilon_B) \\ & + C \sin(2\pi f_A t + \phi_A + \epsilon_C) \} \end{aligned} \quad (2.17)$$

Now, the negative-sequence component of phase-A is calculated by applying the same back transformation matrix. The equations are stated in equations 2.18, 2.19, 2.20 and 2.21.

$$\widetilde{x}_A^-(t) = \sqrt{\frac{2}{3}} \{x_D^{LP-}(t) \cos(-2\pi ft) - x_Q^{LP-}(t) \sin(-2\pi ft)\} \quad (2.18)$$

$$\begin{aligned}
\widetilde{x}_A^-(t) = \frac{1}{2}\sqrt{\frac{2}{3}}\sqrt{\frac{2}{3}}\{ & A \sin(2\pi(f_A - f)t + \phi_A) \cos(2\pi ft) \\
& + B \sin(2\pi(f_A - f)t + \phi_A - 4\pi/3 + \epsilon_B) \cos(2\pi ft) \\
& + C \sin(2\pi(f_A - f)t + \phi_A + 4\pi/3 + \epsilon_C) \cos(2\pi ft) \\
& + A \cos(2\pi(f_A - f)t + \phi_A) \sin(2\pi ft) \\
& + B \cos(2\pi(f_A - f)t + \phi_A - 4\pi/3 + \epsilon_B) \sin(2\pi ft) \\
& + C \cos(2\pi(f_A - f)t + \phi_A + 4\pi/3 + \epsilon_C) \sin(2\pi ft)\}
\end{aligned} \tag{2.19}$$

$$\begin{aligned}
\widetilde{x}_A^-(t) = \frac{1}{6}\{ & A[\sin(2\pi f_A t + \phi_A) + \sin(2\pi(f_A - 2f)t + \phi_A)] \\
& + B[\sin(2\pi f_A t + \phi_A - 4\pi/3 + \epsilon_B) + \sin(2\pi(f_A - 2f)t + \phi_A - 4\pi/3 + \epsilon_B)] \\
& + C[\sin(2\pi f_A t + \phi_A + 4\pi/3 + \epsilon_C) + \sin(2\pi(f_A - 2f)t + \phi_A + 4\pi/3 + \epsilon_C)] \\
& + A[\sin(2\pi f_A t + \phi_A) - \sin(2\pi(f_A - 2f)t + \phi_A)] \\
& + B[\sin(2\pi f_A t + \phi_A - 4\pi/3 + \epsilon_B) - \sin(2\pi(f_A - 2f)t + \phi_A - 4\pi/3 + \epsilon_B)] \\
& + C[\sin(2\pi f_A t + \phi_A + 4\pi/3 + \epsilon_C) - \sin(2\pi(f_A - 2f)t + \phi_A + 4\pi/3 + \epsilon_C)]\}
\end{aligned} \tag{2.20}$$

$$\begin{aligned}
\widetilde{x}_A^-(t) = \frac{1}{3}\{ & A \sin(2\pi f_A t + \phi_A) \\
& + B \sin(2\pi f_A t + \phi_A - 4\pi/3 + \epsilon_B) \\
& + C \sin(2\pi f_A t + \phi_A + 4\pi/3 + \epsilon_C)\}
\end{aligned} \tag{2.21}$$

Calculation of the zero-sequence component of phase-A is again straightforward 2.22, 2.23. At the end, the zero-sequence component of respective phase is the 1/3 of the summation of all three phases filtered with a bandpass filter whose cut-off frequency is set according to the frequency component under consideration, f . Again f_A is assumed to be very close to f .

$$\begin{aligned}
\widetilde{x}_A^o(t) = \frac{1}{2}\sqrt{\frac{2}{3}}\sqrt{\frac{2}{3}}\{ & A \sin(2\pi \widehat{f}_A t + \phi_A) \\
& + B \sin(2\pi \widehat{f}_A t + \phi_A - 2\pi/3 + \epsilon_B) \\
& + C \sin(2\pi \widehat{f}_A t + \phi_A + 2\pi/3 + \epsilon_C)\}
\end{aligned} \tag{2.22}$$

$$\begin{aligned}\widetilde{x}_A^o(t) = & \frac{1}{3} \{ A \sin(2\pi f_A t + \phi_A) \\ & + B \sin(2\pi f_A t + \phi_A - 2\pi/3 + \epsilon_B) \\ & + C \sin(2\pi f_A t + \phi_A + 2\pi/3 + \epsilon_C) \}\end{aligned}\quad (2.23)$$

Last, the phase-A component of the respective harmonic or interharmonic is stated as the summation of all these three components, the positive-sequence, the negative-sequence and the zero-sequence respectively as in 2.24. The overall procedure is also applicable to and true for all other phases.

$$\begin{aligned}\widetilde{x}_A(t) &= \widetilde{x}_A^+(t) + \widetilde{x}_A^-(t) + \widetilde{x}_A^o(t) \\ &= A \sin(2\pi f_A t + \phi_A)\end{aligned}\quad (2.24)$$

The above derivation is summarized as a novel block diagram shown in Figure 2.13.

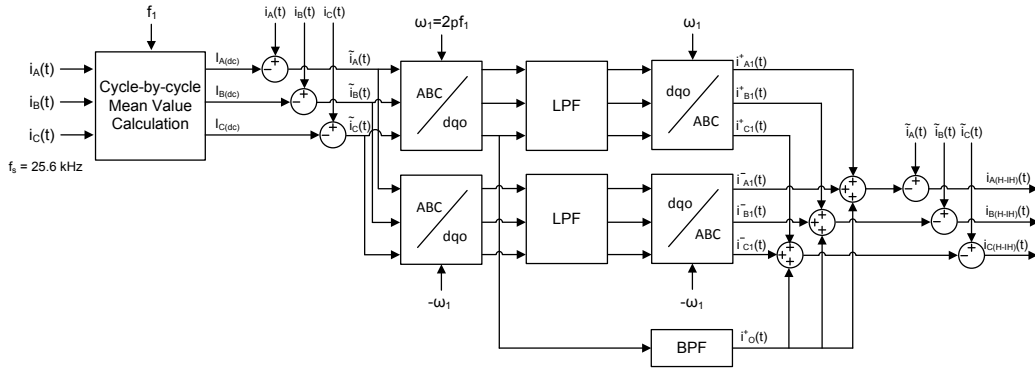


Figure 2.13: Online extraction of direct current and fundamental current components for unbalanced systems (all positive-, negative- and zero-sequences) from the actual three phase line current waveforms sampled at a rate of 25.6 kHz/channel in the field.

CHAPTER 3

APPLICATION OF MSRF

Actual three-phase line current waveforms ($i_A(t)$, $i_B(t)$, $i_C(t)$) recorded on the MV side of the EAF transformer are shown in Figure 3.1 for a typical ten-cycle window in the boring phase of the EAF (the worst operation condition). The asymmetrical behavior of the waveform can be easily observed from this figure. The amplitudes of the phase jump from 1000A to 3000A inside any two-cycle duration. The content of the harmonics and interharmonics can also be observed from the deviation of the waveforms from ideal sinusoidal waveform. Phases and frequencies are also different at each cycle. This kind of waveform representing an AC EAF load is not uncommon during the whole operation cycle (which is approximately 55 mins) and the same characteristics is repeated at the other operational periods.

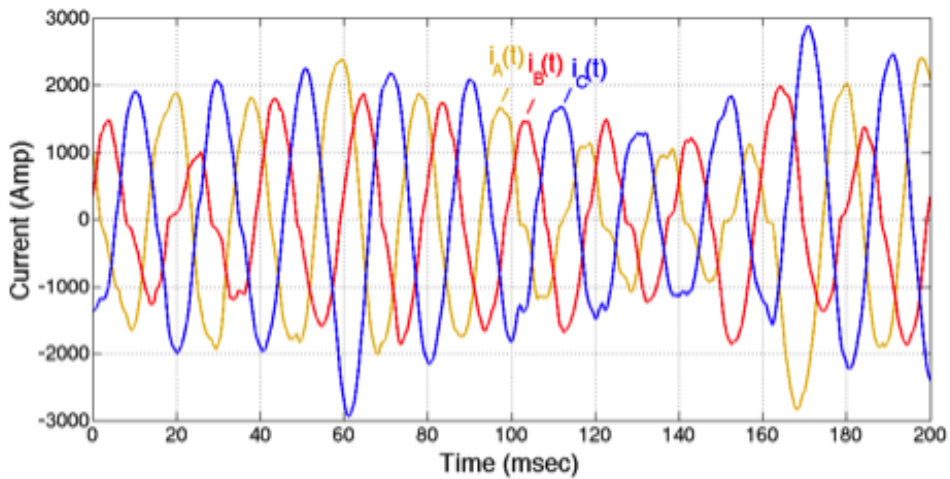


Figure 3.1: Actual line current waveforms recorded on the MV side of EAF transformer (ten-cycle window during the boring phase of the EAF).

The frequency content of this 10-cycle waveform is given in Figure 3.2 with all positive- and negative- sequence components. The amplitude of the positive-sequence fundamental current component is considered as 100% and the rest of the magnitudes are represented as percentages of the positive-sequence fundamental component. The positive-sequence is represented by blue color in bar graph whereas the negative-sequence is by red color. In addition to the important integer multiples of harmonics, only the interharmonics around the fundamental and the second harmonic have been shown in this graph. These interharmonic components need significant attention since they are considerably high and also the main cause of flicker. This graph clearly shows the severity of the analyzed current signal. The side bands of the fundamental and the second harmonic are rich in interharmonic content and their amplitudes are close to the integer harmonics.

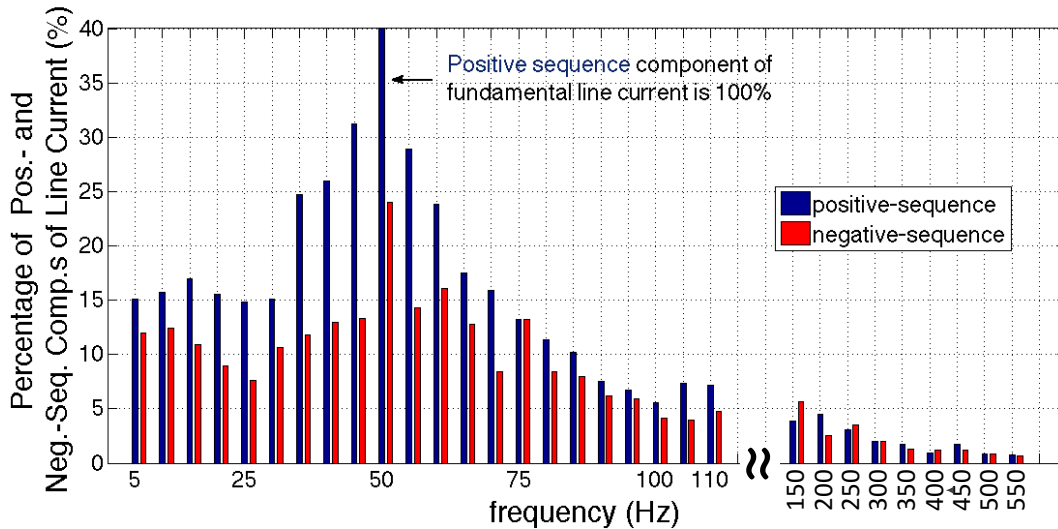


Figure 3.2: Frequency spectrum of 10-cycle current waveform obtained from Figure 3.1 by MSRF analysis in 5-Hz resolution.

In this chapter, a second order Butterworth type low pass filter whose cut-off frequency is tuned to 2.5 Hz is used for the filtration of dq components. The frequency response of this filter is shown in Figure 3.3. In order to verify the proposed algorithm, discrete Fourier transform (DFT) has been utilized whose resolution is 5-Hz. 5-Hz resolution for the frequency axis corresponds to a 10-cycle window which includes 5120 samples for 50Hz waveform in 25.6 kHz sampling frequency. DFT produces only one value for the amplitude of each frequency component and one phase

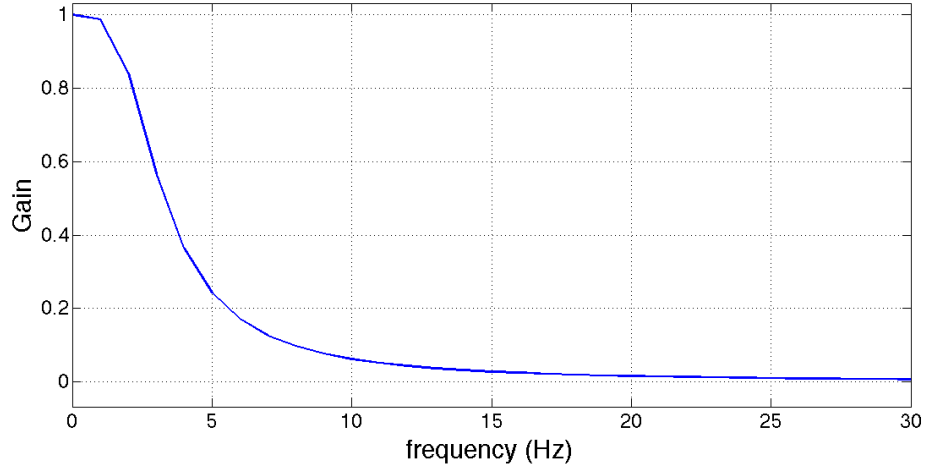


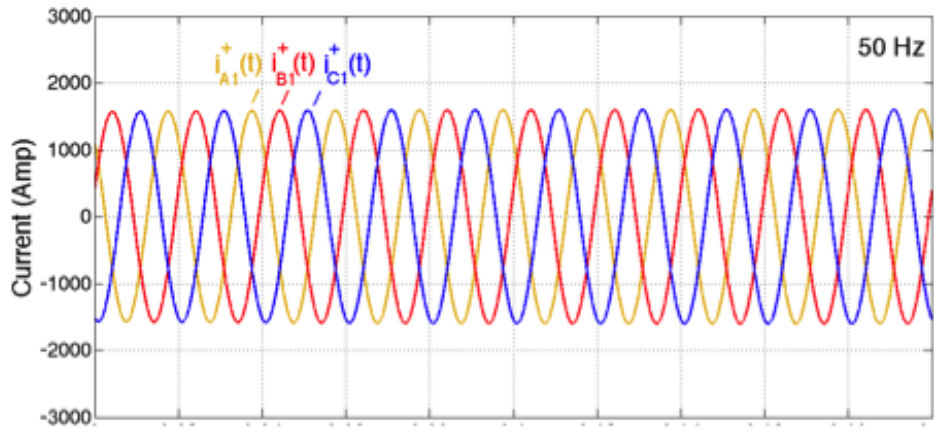
Figure 3.3: Frequency response of the second order Butterworth LPF whose cut-off frequency is set to 2.5 Hz.

information belonging to the corresponding frequency. The variations in 5120 sample are represented only with these values. Therefore, it is reasonable to have some mismatches because of this fact. In addition to this, DFT makes an optimization to represent the actual waveform with the frequency resolution determined by the length of the window. This means that even if the actual waveform does not consist of the frequencies which are at multiples of the frequency resolution, the frequencies inside the waveform are represented by these frequencies. In other words, if the actual waveform includes 48Hz, it will be represented by the nearby frequencies such as 50Hz, 45Hz, and etc. This is a drawback of the Fourier transform based algorithms. Besides, the MSRF method gives the true values of each frequency searched in the actual waveform. This means that if the frequency of the MSRF analysis is selected to be $f = 57\text{Hz}$, and the actual waveform does not include 57Hz (i.e. $f_A \neq 57\text{Hz}$), then the MSRF result will give almost zero depending on the performance of the chosen LPF. Hence, there can be again some discrepancies between FFT and MSRF results. However, it will be observed from the results that they are in parallel to each other.

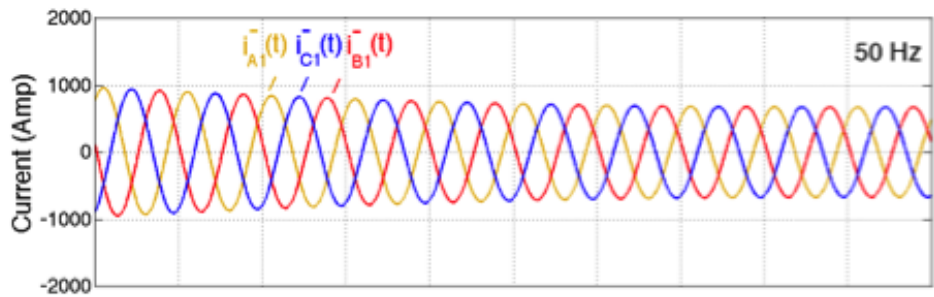
3.1 Results of MSRF Analysis Applied on Some Important Harmonics and Interharmonics

Positive-sequence fundamental components ($i_{A1}^+(t)$, $i_{B1}^+(t)$, $i_{C1}^+(t)$), negative-sequence fundamental components ($i_{A1}^-(t)$, $i_{B1}^-(t)$, $i_{C1}^-(t)$) and the total fundamental components themselves ($i_{A1}^+(t) + i_{A1}^-(t)$, $i_{B1}^+(t) + i_{B1}^-(t)$, $i_{C1}^+(t) + i_{C1}^-(t)$) of the actual current waveforms shown in Figure 3.1 obtained by MSRF analysis set are given in Figures 3.4a, 3.4b, 3.4c, respectively. For the same raw data set in Figure 3.1, positive-sequence second harmonic components ($i_{A2}^+(t)$, $i_{B2}^+(t)$, $i_{C2}^+(t)$), negative-sequence second harmonic components ($i_{A2}^-(t)$, $i_{B2}^-(t)$, $i_{C2}^-(t)$) and the total second harmonic components ($i_{A2}^+(t) + i_{A2}^-(t)$, $i_{B2}^+(t) + i_{B2}^-(t)$, $i_{C2}^+(t) + i_{C2}^-(t)$) are also given in Figures 3.5a, 3.5b, and 3.5c, respectively. Asymmetrical characteristics of the total line currents for each harmonic component and the contribution of the negative-sequence components to these harmonics are apparent from Figures 3.4 and 3.5.

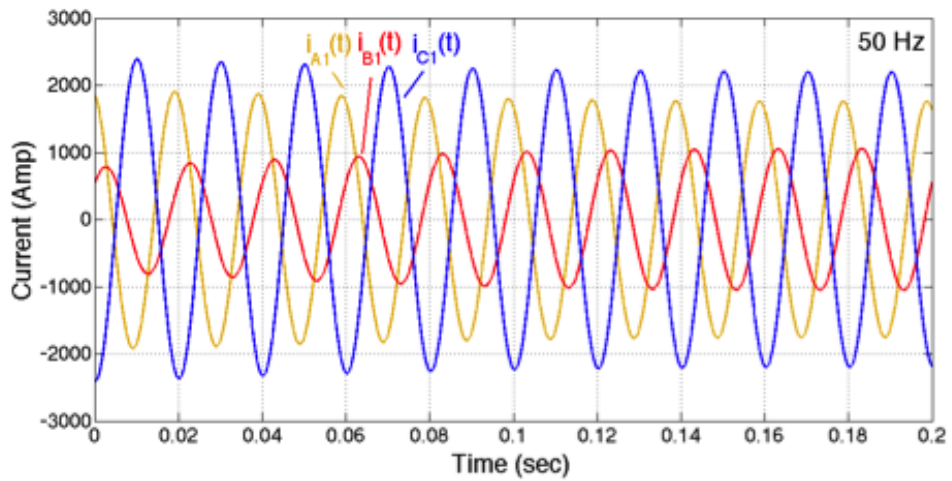
All integer harmonics up to the 50th and interharmonics with 5-Hz resolution upto 1.5kHz are determined from the field data for a typical tap-to-tap time (approximately 50 mins) by MSRF analysis. Note that by the proposed MSRF analysis, it is possible to obtain the frequency component of the current waveform at any rational frequency value, not necessarily at a multiple of 5 Hz from zero to half of the sampling frequency, however, only the interharmonics at multiples of 5 Hz with significantly high amplitudes are considered to make the results comparable with the DFT results, whose frequency resolution is 5 Hz as recommended in IEC Std. 61000-4-7 [35]. For the prominent interharmonic current components ($f_{iH} = 5, 10, 15, 20, 25, 30, 35, 40, 45, 55, 60, 65$, and 70 Hz) around the fundamental frequency ($f_1 = 50$ Hz), positive- and negative-sequence components of these interharmonics are as given in Figures 3.6 and 3.7 over a typical tap-to-tap time. The RMS values of the 40, 45, 50, 55 and 60 Hz components have been given cycle-by-cycle in order to show the rapid amplitude fluctuations, while 1-sec-averaged RMS values of the 5, 10, 15, 20, 25, 30, 35, 65, 70, 75, 80 and 85 Hz components have been given in order to show the pattern clearer. In a similar way, some dominant interharmonics ($f_{iH} = 75, 80, 85, 90, 95$, and 105 Hz – significance of these harmonics and interharmonics for an EAF plant had also been noted previously in [2]) around the second harmonic current component



(a) Positive-sequence

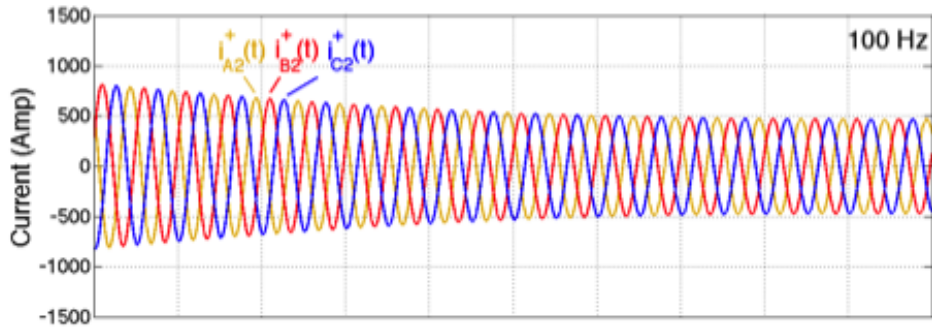


(b) Negative-sequence

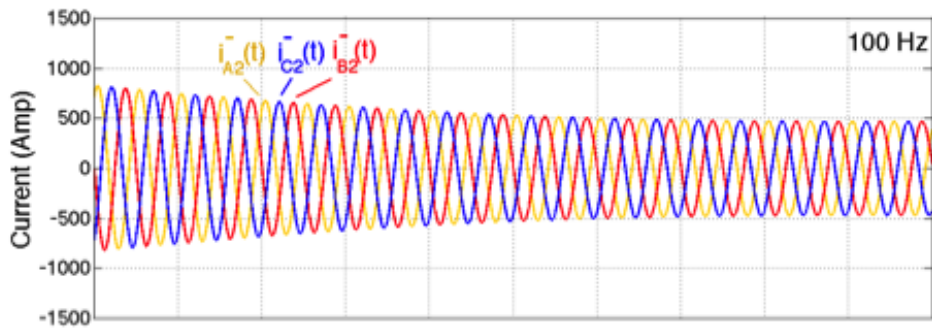


(c) Summation of positive- and negative-sequences for each phase.

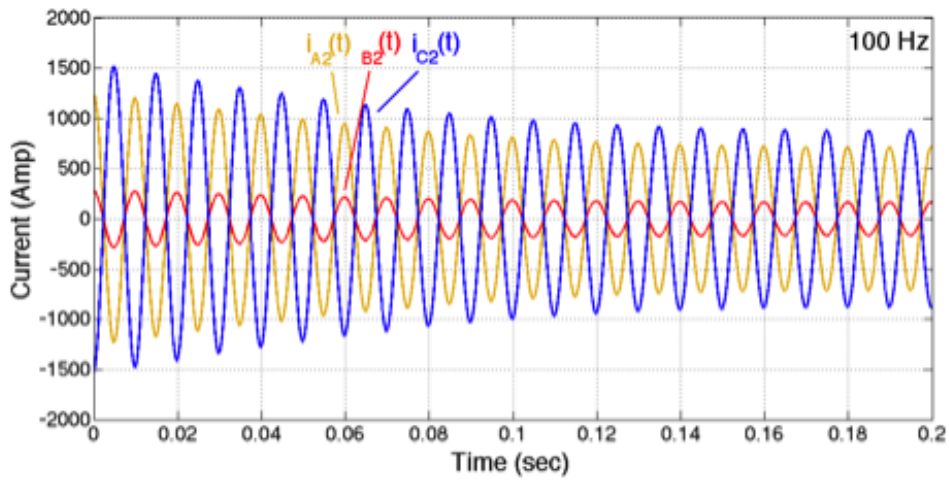
Figure 3.4: Fundamental components of the line currents obtained from the actual current waveforms given in Figure 3.1 by SRF analysis illustrated in Figure 2.10.



(a) Positive-sequence



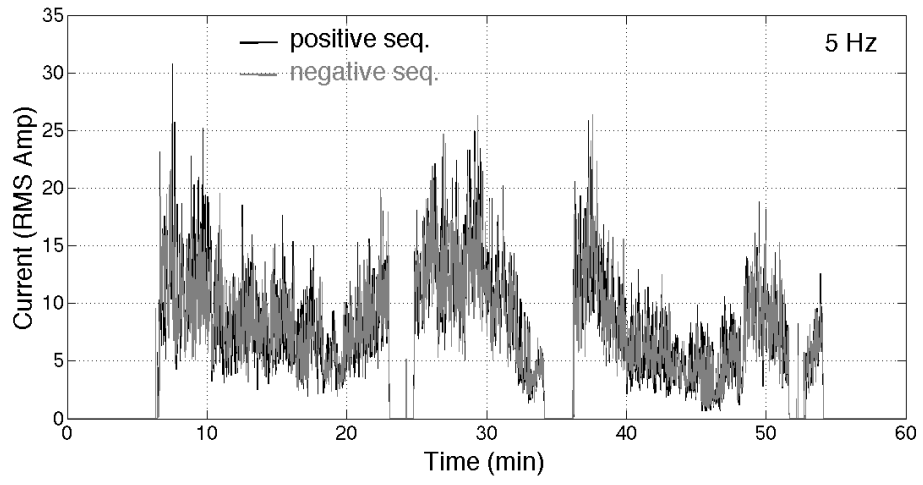
(b) Negative-sequence



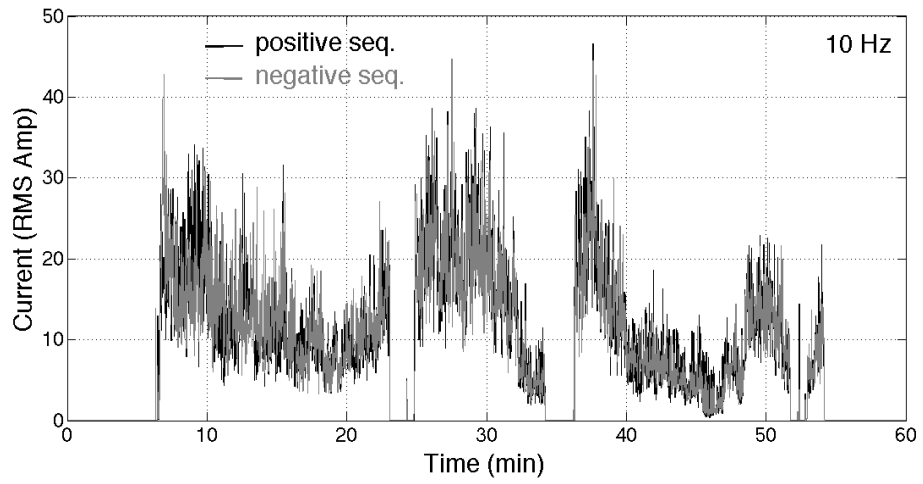
(c) Summation of positive- and negative-sequences for each phase.

Figure 3.5: Second harmonic components of the line currents obtained from the actual current waveforms given in Figure 3.1 by MSRF analysis illustrated in Figure 2.11.

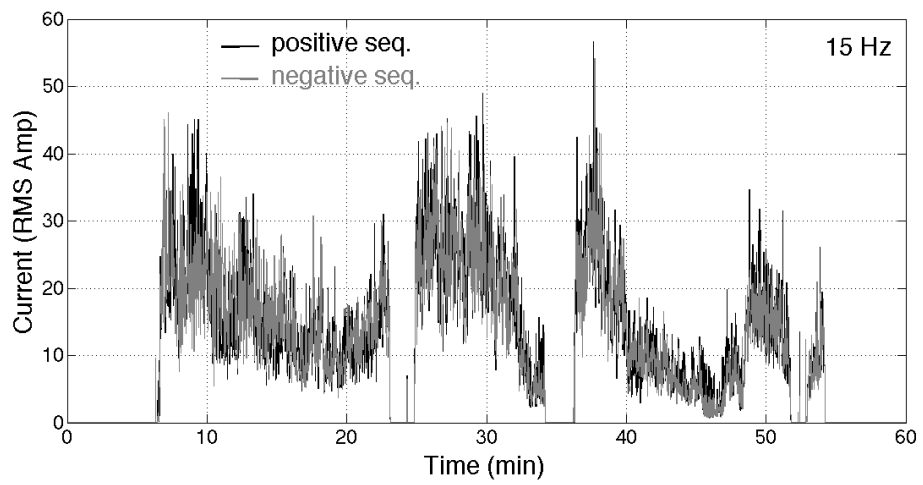
($f_2=100$ Hz) are given in Figures 3.8 and 3.9.



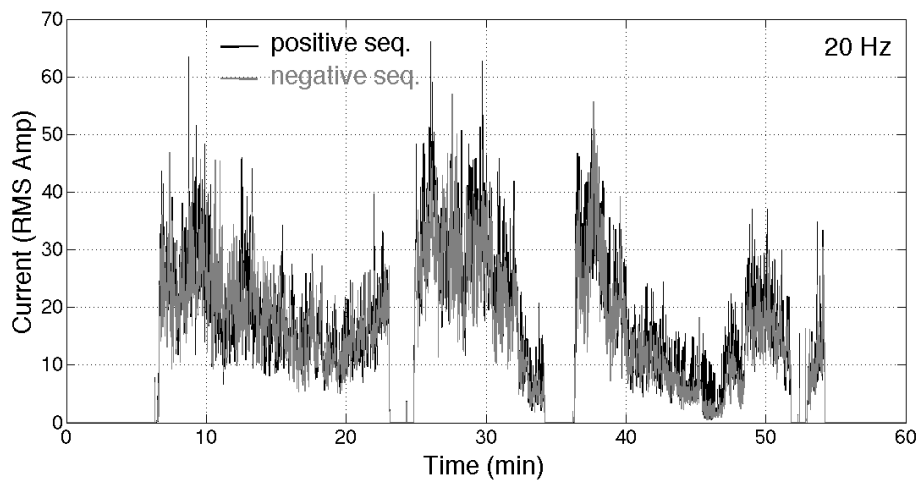
(a) $f_{iH}=5$ Hz



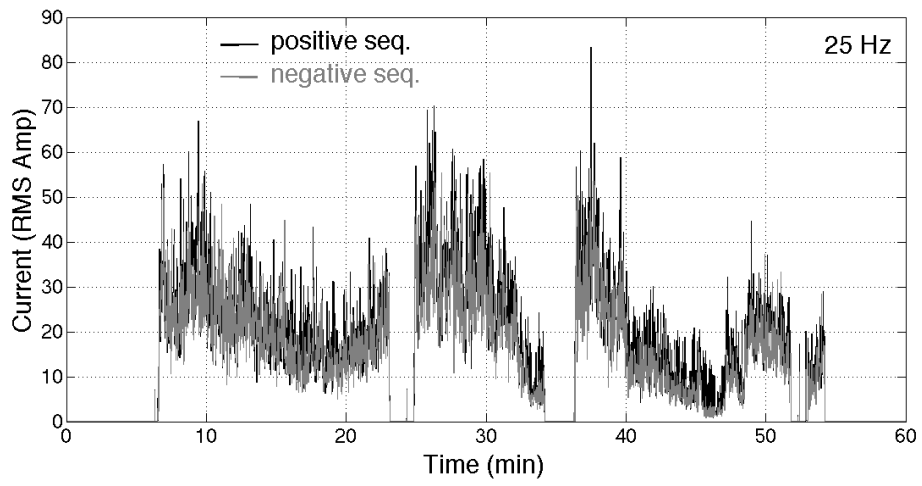
(b) $f_{iH}=10$ Hz



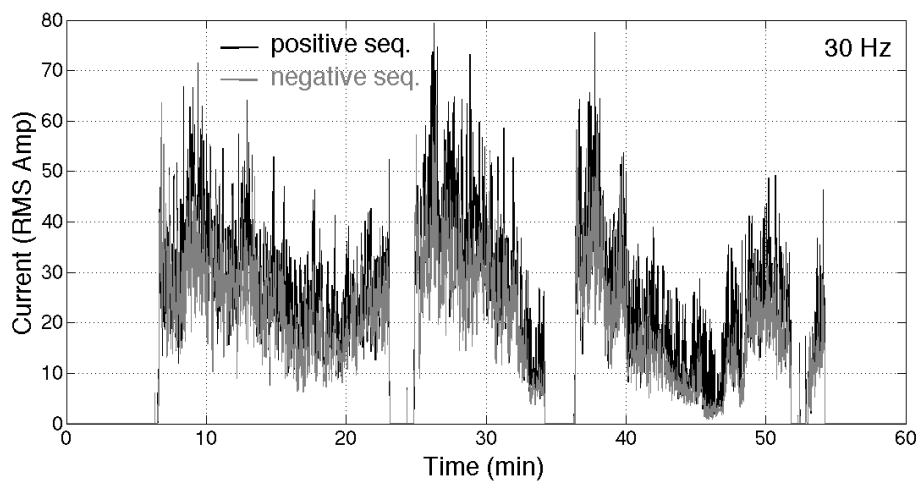
(c) $f_{iH}=15$ Hz



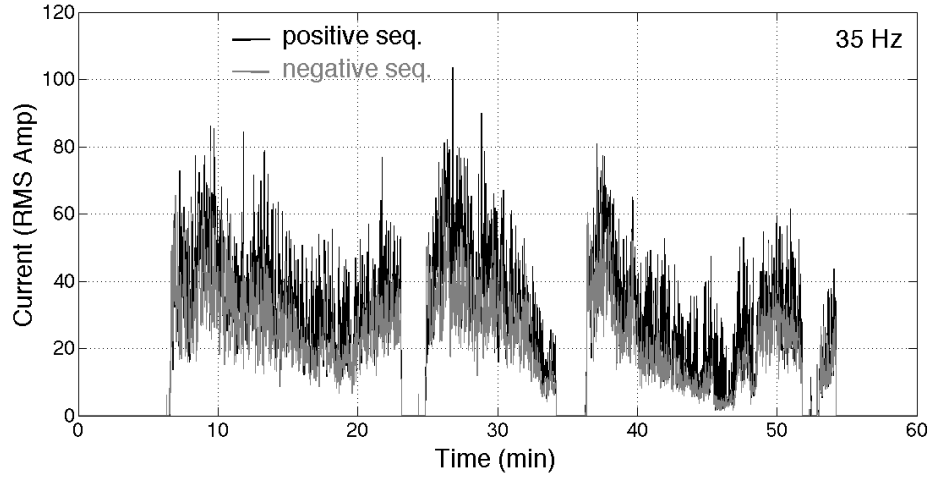
(d) $f_{iH}=20$ Hz



(e) $f_{iH}=25$ Hz



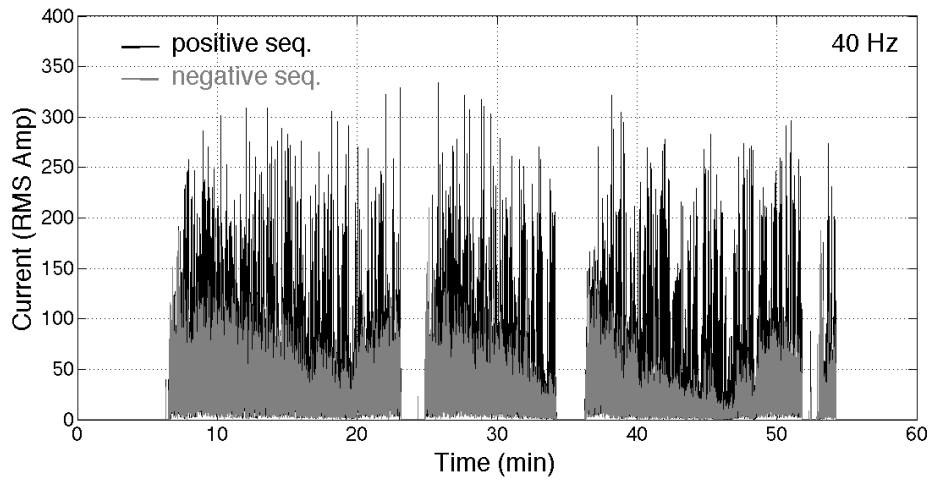
(f) $f_{iH}=30$ Hz



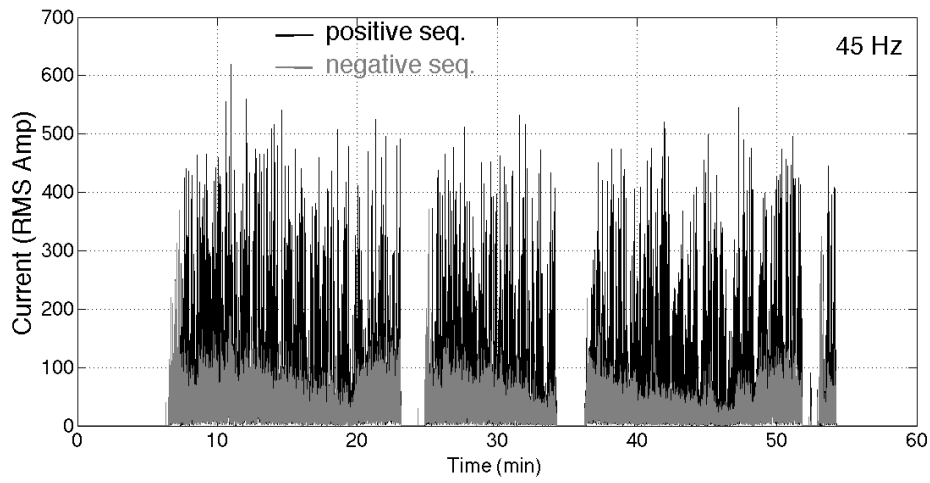
(g) $f_{iH}=35$ Hz

Figure 3.6: Positive-sequence (black colored) and negative-sequence (grey colored) RMS current components of some interharmonics (1-sec-averaged RMS current calculation over a tap-to-tap time).

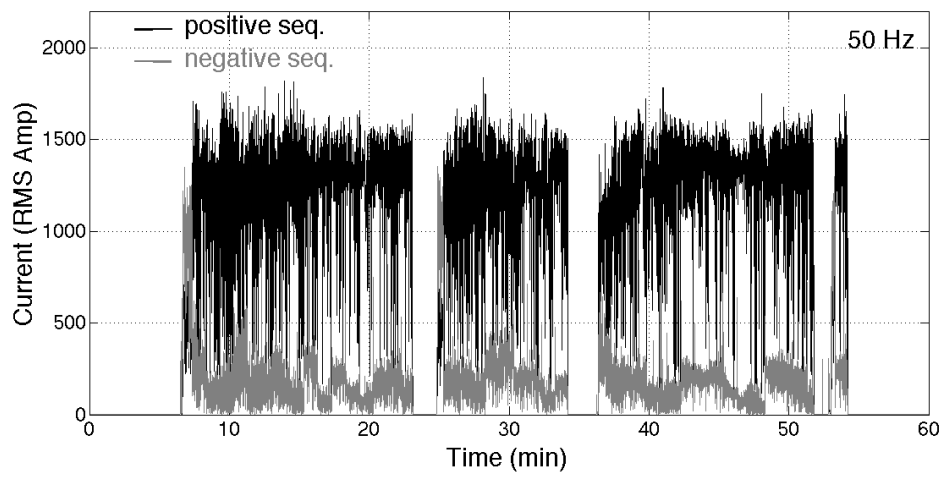
In order to make a comparison between various interharmonics, harmonics and the fundamental component, the results of the proposed MSRF analysis are summarized in Table 3.1. In this table, averages of RMS values of the consequent cycles of each frequency component for both positive- and negative-sequence components calculated over a typical tap-to-tap time are given for some interharmonics, harmonics and the fundamental component. Similarly, the positive-sequence of the fundamental component has been taken as 100% and the rest of the components have been computed as percentages of this value. A comparison between the cycle-by-cycle computed positive- and negative- sequence components in Figures 3.7 and 3.9 and the mean values computed by averaging them over the tap-to-tap time in Table 3.1 show that each interharmonic or harmonic current component may have much larger one-cycle RMS value than its mean value, at any time. Therefore, fast tracking of every harmonic and interharmonic is necessary in order to be able to compensate the undesired components to an acceptable level. For example, 45Hz component has jumped up to 600A-RMS when the fundamental positive-sequence component has increased up to approximately 1800A-RMS as seen in Figure 3.7, which means that 45Hz has been increased up to 30% of the fundamental frequency component. However the mean value of 45Hz over a tap-to-tap time is calculated as only 4.86% of the



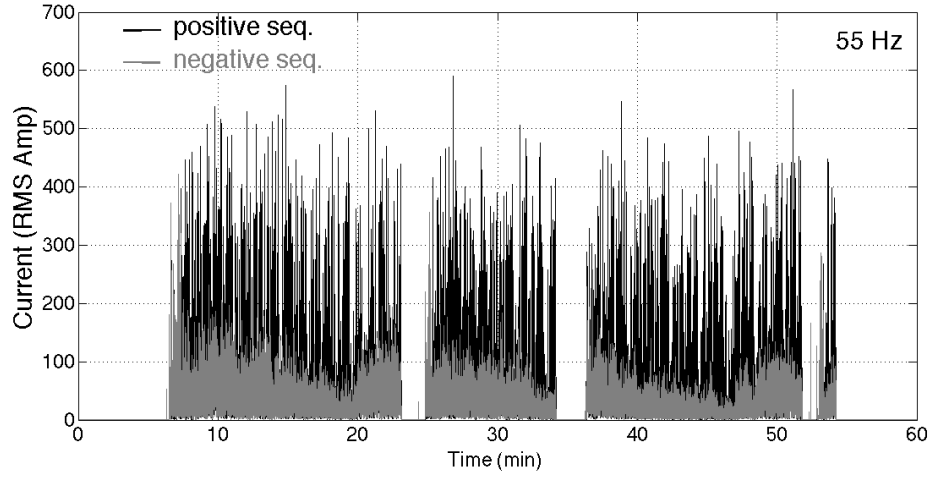
(a) $f_{iH}=40$ Hz



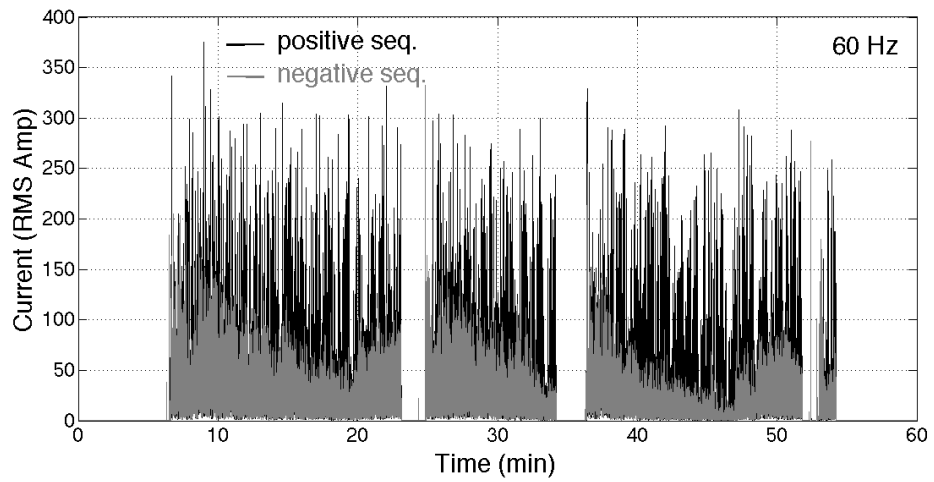
(b) $f_{iH}=45$ Hz



(c) $f_1=50$ Hz

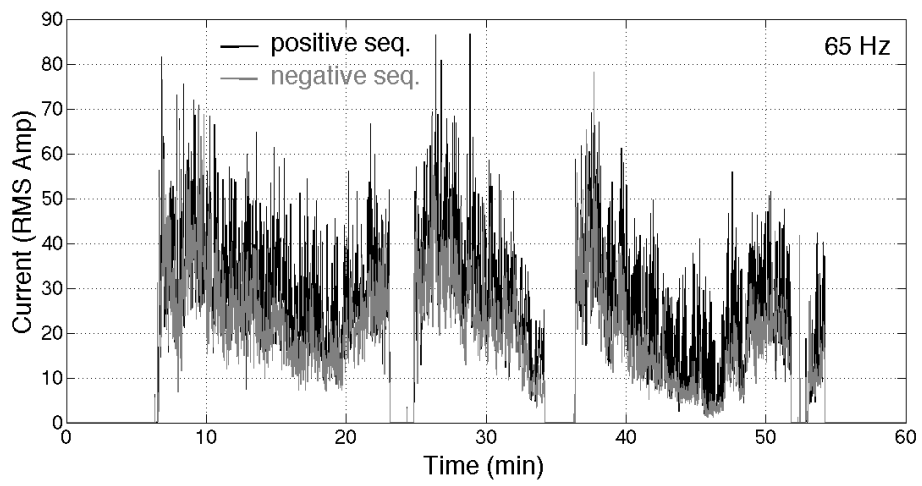


(d) $f_{iH}=55$ Hz

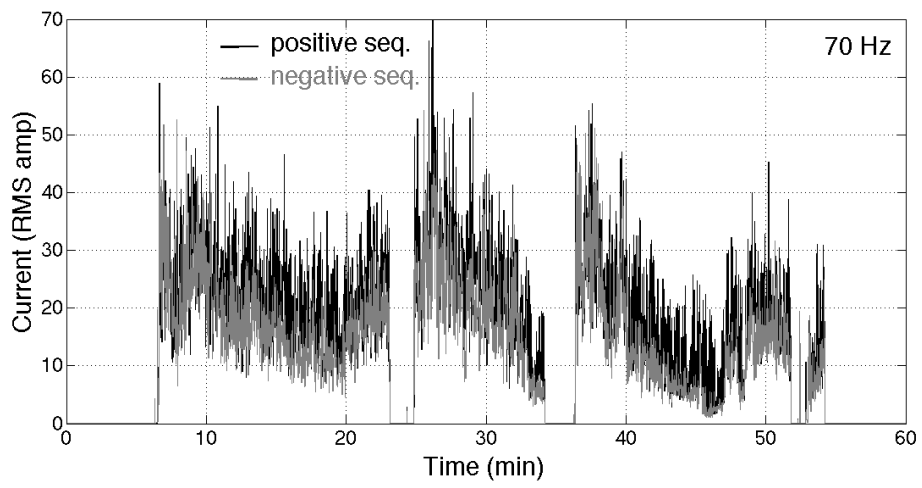


(e) $f_{iH}=60$ Hz

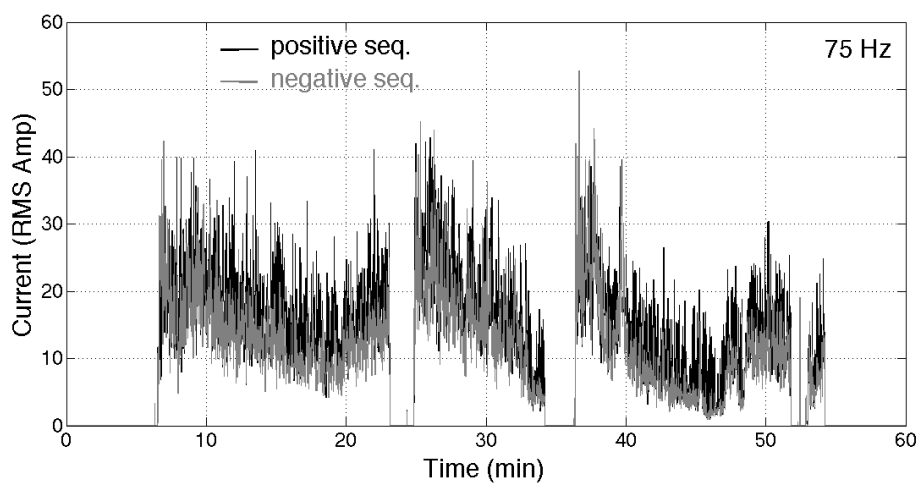
Figure 3.7: Positive-sequence (black colored) and negative-sequence (grey colored) RMS current components of some interharmonics in comparison with the RMS of the fundamental component (cycle-by-cycle RMS current calculation over a tap-to-tap time).



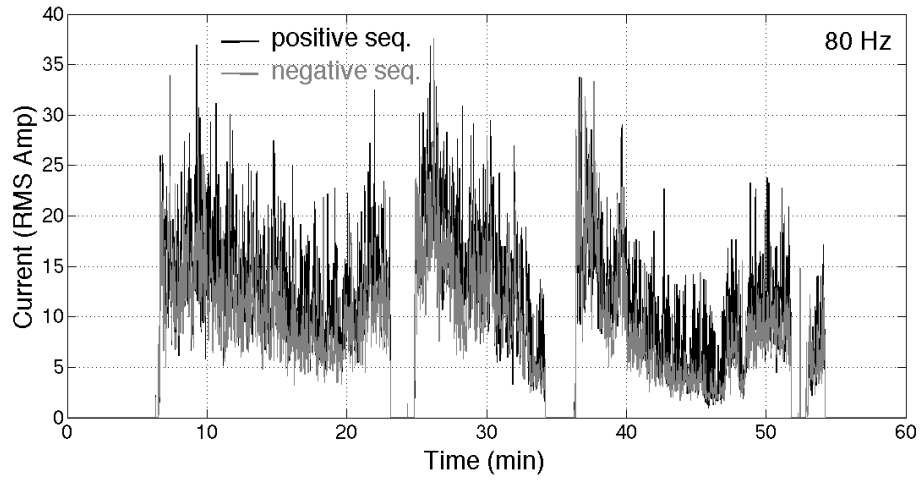
(a) $f_{iH}=65$ Hz



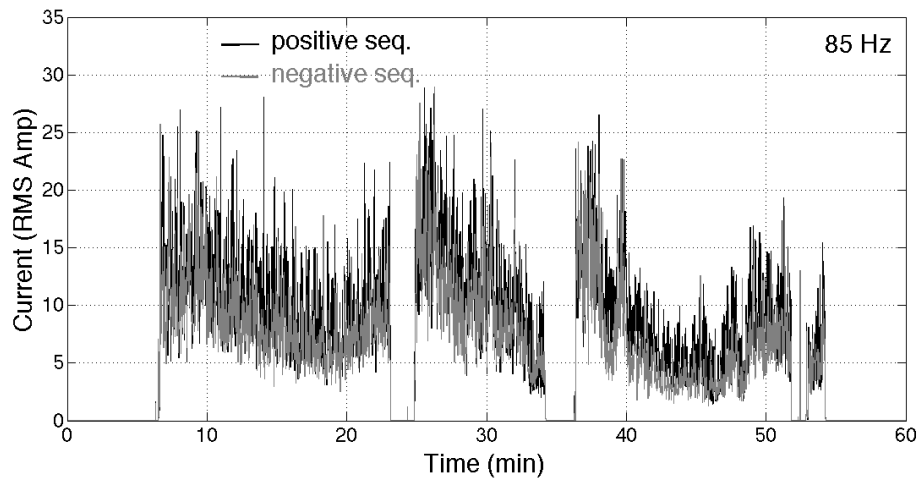
(b) $f_{iH}=70$ Hz



(c) $f_1=75$ Hz

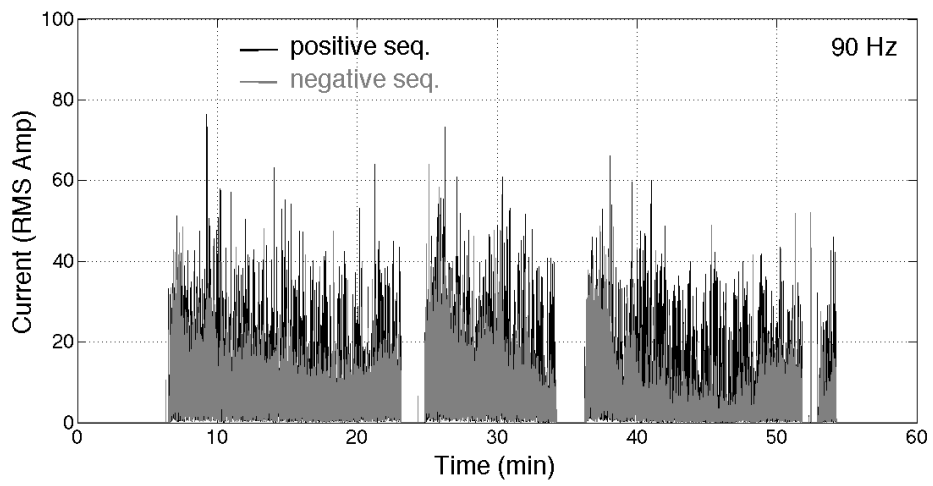


(d) $f_{iH}=80$ Hz

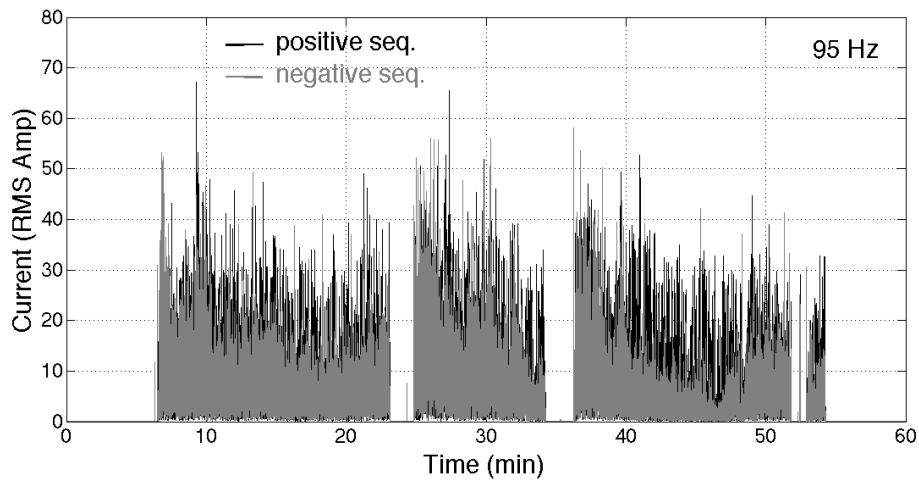


(e) $f_{iH}=85$ Hz

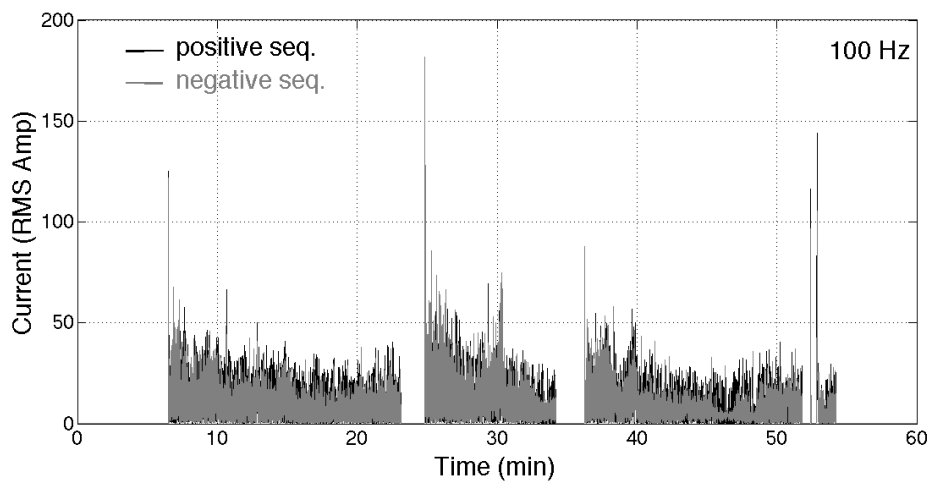
Figure 3.8: Positive-sequence (black colored) and negative-sequence (grey colored) RMS current components of some interharmonics (1-sec-averaged RMS current calculation over a tap-to-tap time).



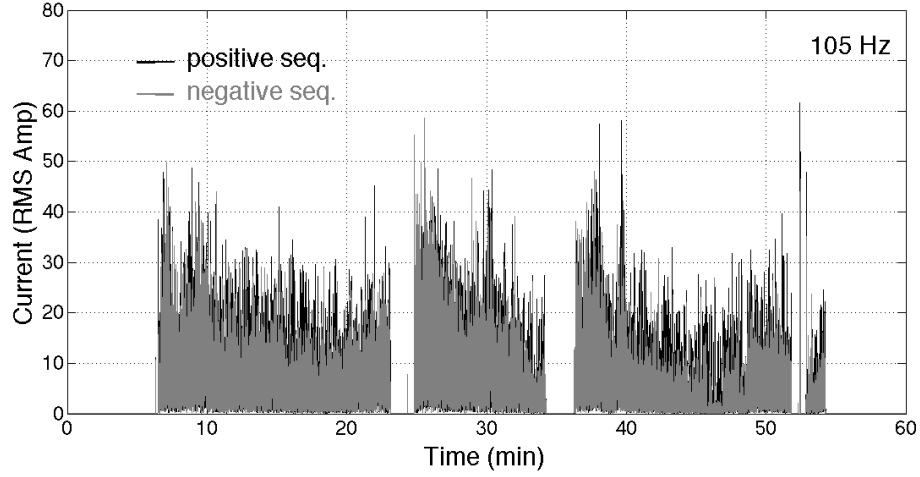
(a) $f_{iH}=90$ Hz



(b) $f_{iH}=95$ Hz



(c) $f_2=100$ Hz



(d) $f_{iH}=105$ Hz

Figure 3.9: Positive-sequence (black colored) and negative-sequence (grey colored) RMS current components of some interharmonics in comparison with the RMS of the second harmonic current component (cycle-by-cycle RMS current calculation over a tap-to-tap time).

fundamental component as shown in Table 3.1.

3.2 Verification of MSRF Results by Comparing Them with DFT Results

The results of MSRF analysis will be verified by DFT analysis in this section. For this purpose, line current components of harmonics ($i_{Ah}(t)$, $i_{Bh}(t)$, $i_{Ch}(t)$ in Figure 2.11) and interharmonics ($i_{AiH}(t)$, $i_{BiH}(t)$, $i_{CiH}(t)$ in Figure 2.12) are compared with corresponding harmonic and interharmonic components ($I_A(jw)$, $I_B(jw)$, and $I_C(jw)$) obtained from DFT analysis based on 10-cycle DFT for the same raw data set collected in the field. Figure 3.10 shows the computation of the frequency spectrum of the three-phase EAF currents on 10-cycle DFT windows, sliding one-cycle at each computation step. As shown in Figure 3.10, the raw data are resampled by spline interpolation so that 5120 sample fit 10-cycle of the fundamental frequency exactly in order to eliminate the spectral leakage effect of Fourier transform since 5120-sample is a multiple of a power of two, Fast Fourier Transform (FFT) is used for DFT analysis. In order to talk about the spectral leakage effect briefly, first the FFT window

Table 3.1: Interharmonics and harmonics in line current waveforms on MV side of a sample AC EAF transformer (mean RMS values over a tap-to-tap time; positive-sequence of the fundamental current is assumed to be 100%).

Frequency (Hz)	% Current		Comments
	Positive-Sequence	Negative-Sequence	
5	0.68	0.66	low and comparable seqs.
10	1	0.98	low and comparable seqs.
15	1.26	1.21	low and comparable seqs.
20	1.52	1.39	low and comparable seqs.
25	1.76	1.49	low and comparable seqs.
30	2.11	1.67	comparable seqs.
35	2.59	1.93	comparable seqs.
40	3.45	2.36	prominent (+)ve seq.
45	4.86	2.96	prominent (+)ve seq.
50	100	15.61	dominant (+)ve seq.
55	4.79	3.09	prominent (+)ve seq.
60	3.24	2.31	prominent (+)ve seq.
65	2.24	1.71	comparable seqs.
70	1.66	1.31	low and comparable seqs.
75	1.28	1.01	low and comparable seqs.
80	1	0.8	low and comparable seqs.
85	0.79	0.64	low and comparable seqs.
90	0.7	0.62	low and comparable seqs.
95	0.69	0.63	low and comparable seqs.
100	0.85	0.81	low and comparable seqs.
105	0.67	0.61	low and comparable seqs.
150	1.51	2.3	prominent (-)ve seq.
200	0.36	0.42	low and comparable seqs.
250	1.21	1.73	low and comparable seqs.
300	0.21	0.21	very low and comparable seqs.
350	0.6	0.54	low and comparable seqs.
400	0.1	0.1	very low and comparable seqs.
450	0.19	0.19	very low and comparable seqs.
500	0.07	0.07	very low and comparable seqs.
550	0.14	0.13	very low and comparable seqs.
600	0.05	0.05	very low and comparable seqs.
650	0.08	0.08	very low and comparable seqs.

should be taken care of. The multiplication of a signal composed of summation of sinusoidals by a square waveform in time domain corresponds to the convolution of pulses with a *sinc* function represented by $\frac{\sin(\pi f)}{\pi f}$ in frequency domain. *sinc* function has a sharp and narrow main lobe with fluctuating side lobes whose magnitude gets smaller and smaller as the frequency increases and decreases frequency as can be seen in Figure 3.11. In this figure, blue dots represent the ideal case when the window size matches exactly with the integer number of cycles taken from the sampled signal. It is obvious that the side lobes of the sinc function that belongs to the center frequency does not effect the other samples taken at the different frequencies since they are equal to zero. However, if the window size is greater or smaller than the number of cycles that are wished to be analyzed, the samples coincide with the shifted version of the sinc function which is shown by the red dots on the same figure. This time, neither the gain of the sample at the center frequency is equal to one (is diminished a little), nor the gain of the samples at the other frequencies will coincide with the zero crossings of the side lobes. For this reason, the energy of the signal at the corner frequency of the *sinc* function will be appeared as spread over the other frequencies. This situation alters the result for each frequency and spectral leakage occurs.

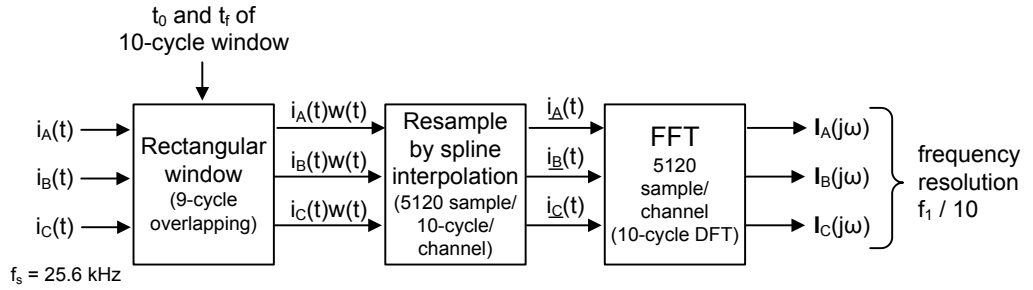


Figure 3.10: Computation of frequency spectrum of the three-phase EAF currents on 10-cycle FFT windows sliding one-cycle at each computation step.

Sample plots for the interharmonics around the fundamental frequency (5-, 10-, 15-, 10-, 25-, 30-, 35-, 40-, 45-, 55-, and 60-Hz) of phase-A currents are given in Figure 3.12. On the other hand, sample plots for the interharmonics around the second harmonic frequency (65-, 70-, 75-, 80-, 85-, 90-, 95-, and 105-) of phase-A currents are given in Figure 3.13. The data sets plotted in Figures 3.12 and 3.13 are 1-s-averaged RMS values. These figures have shown that there is a very good correlation between the results of MSRF analysis and FFT analysis. The discrepancies between the

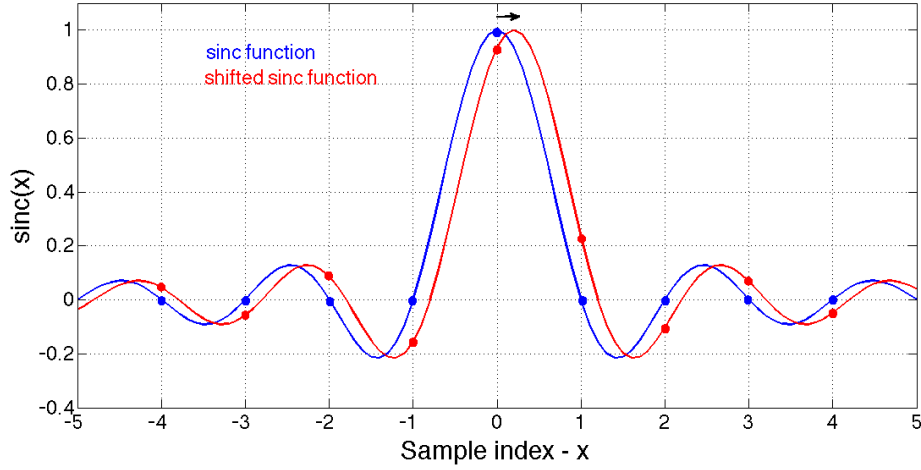
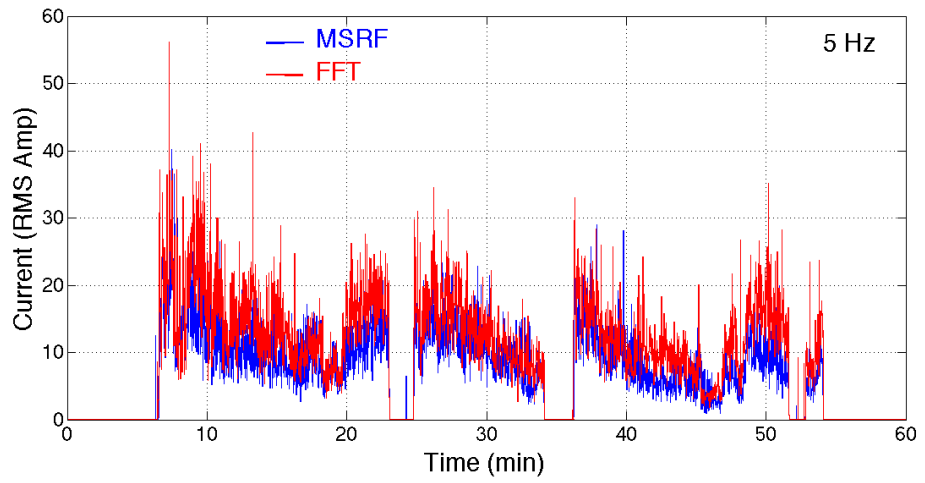


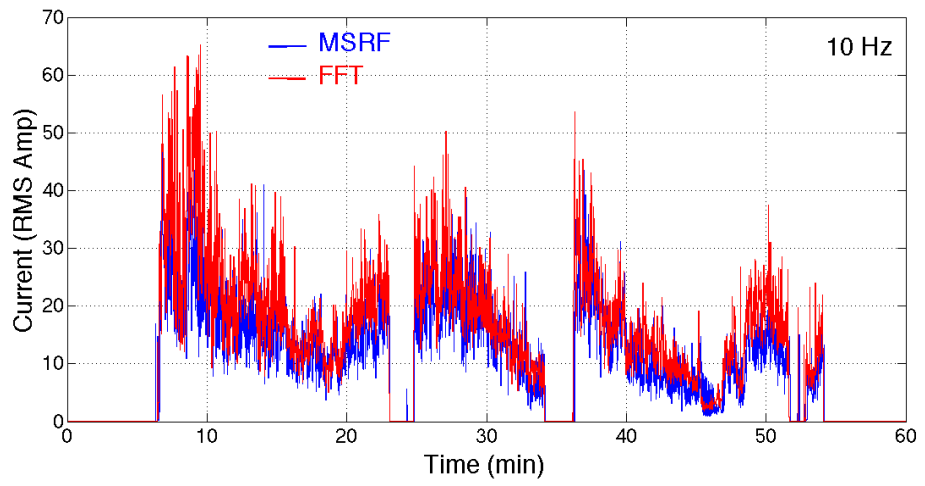
Figure 3.11: Samples taken on an ideal sinc function and on its shifted version.

associated curves are attributed to the fact that results of the FFT analysis are the 1-s-averaged RMS values of moving 10-cycle data windows while MSRF results are the 1-s-averaged values of cycle-by-cycle computed RMS values. The above comparative study shows that MSRF analysis gives very accurate results for the instantaneous magnitudes of the interharmonic and harmonic components of the AC EAF currents.

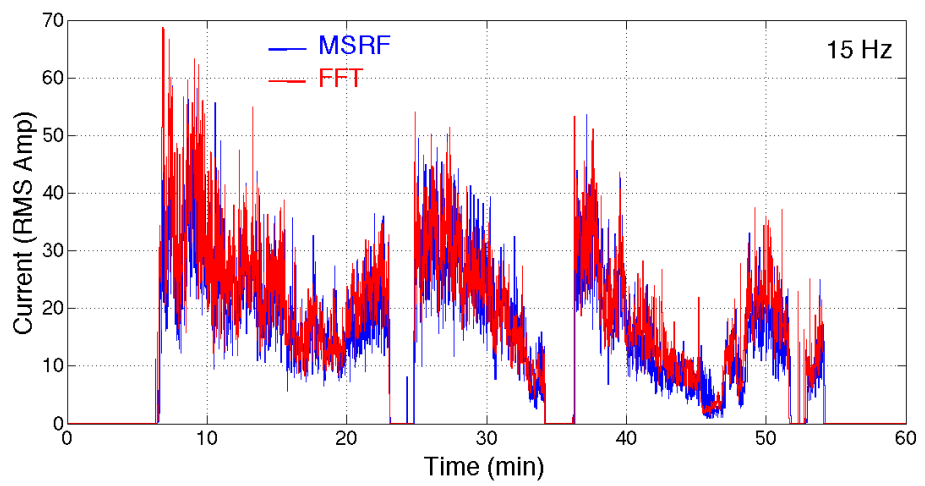
As can be understood from Figures 3.12 and 3.13, the crucible of the EAF is charged three times during the sample tap-to-tap time given. After each charging period, the EAF transformer is energized, thus causing flow of inrush currents in each MV line whose frequency spectrum are very rich in DC, fundamental and the second harmonic components. The inrush currents at the beginning of each charging period can be observed from Figure 3.12j and Figure 3.13h. This phenomenon has been analyzed in a previous study in detail in [2].



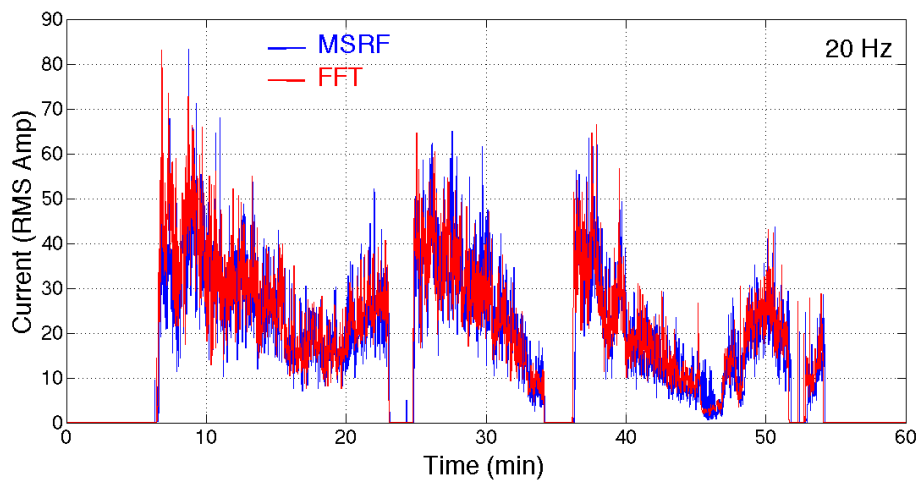
(a) $f_{iH}=5$ Hz



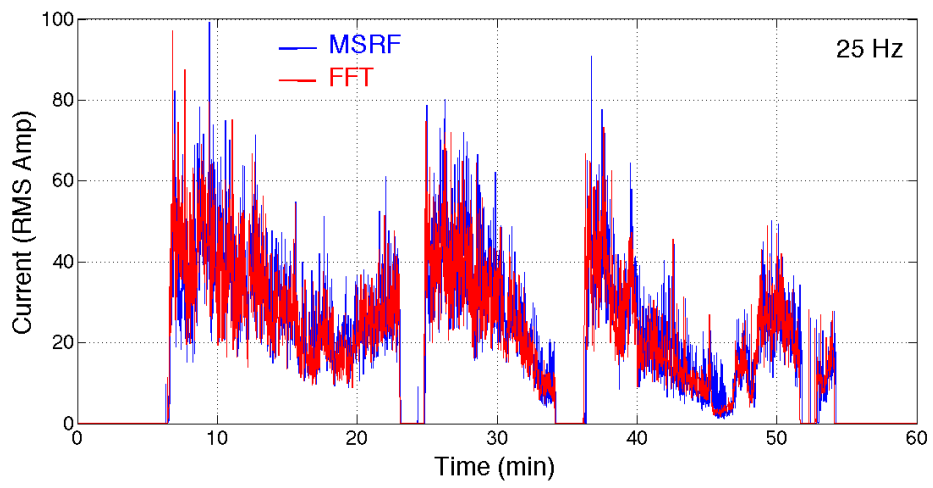
(b) $f_{iH}=10$ Hz



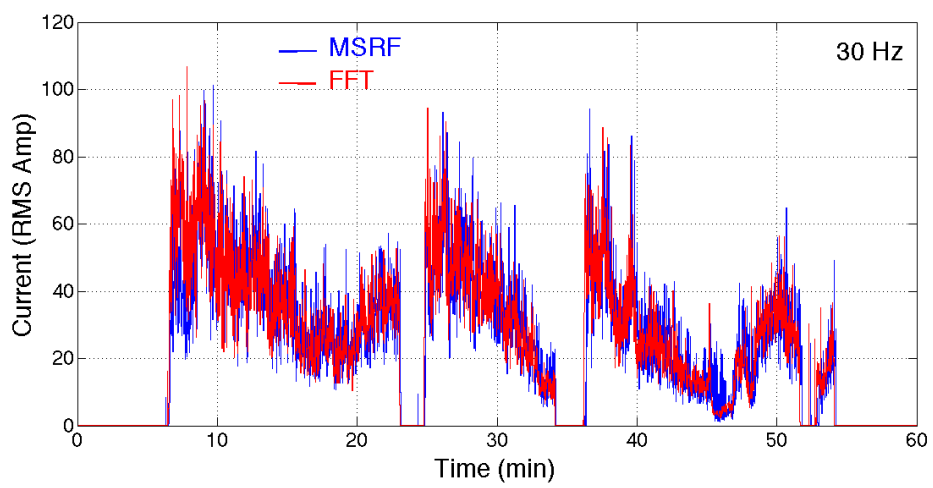
(c) $f_1=15$ Hz



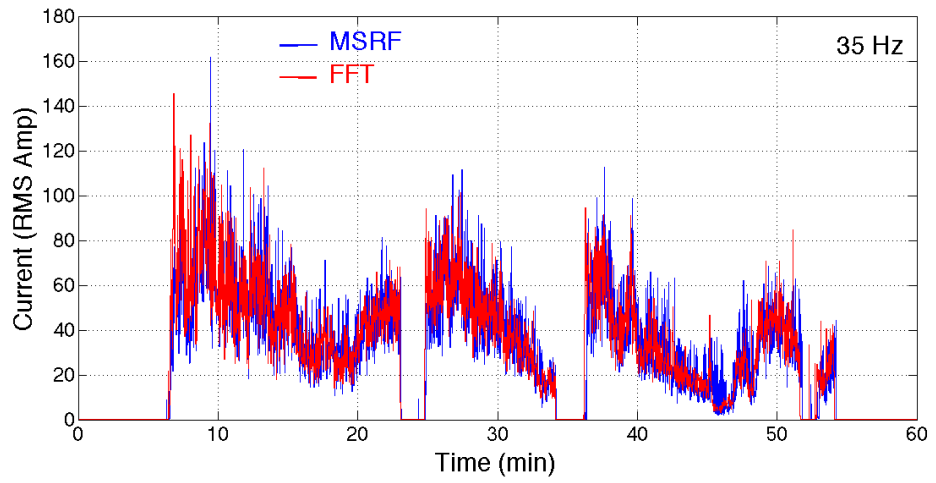
(d) $f_{iH}=20$ Hz



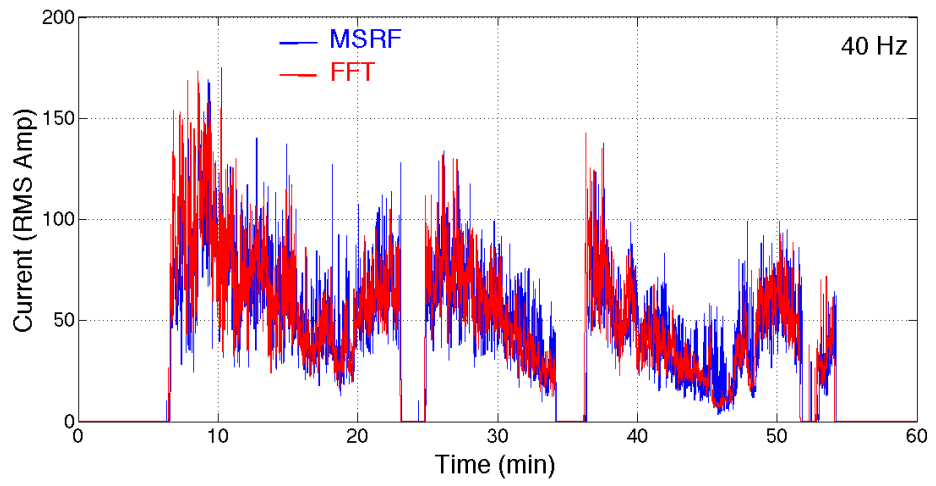
(e) $f_{iH}=25$ Hz



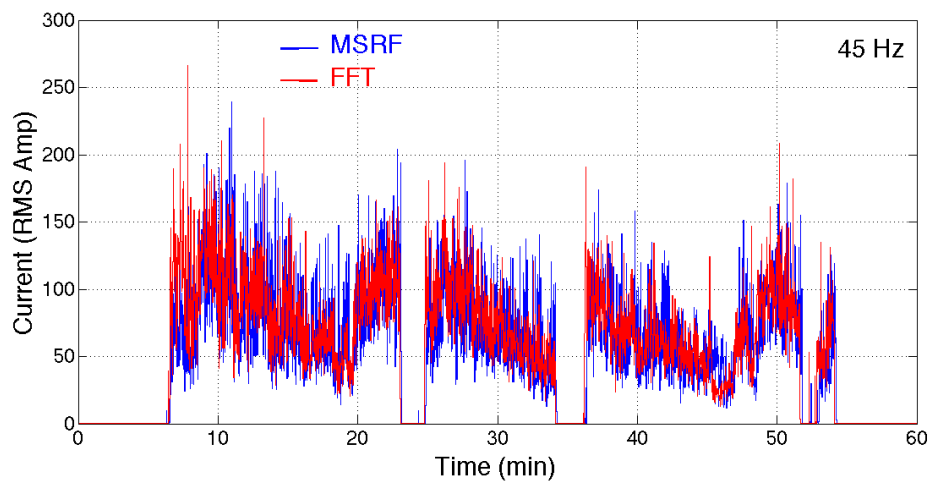
(f) $f_{iH}=30$ Hz



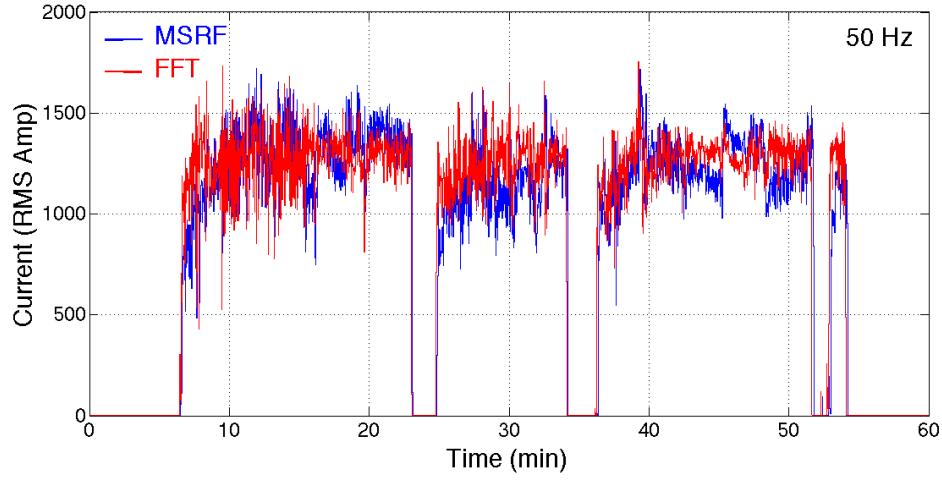
(g) $f_{iH}=35$ Hz



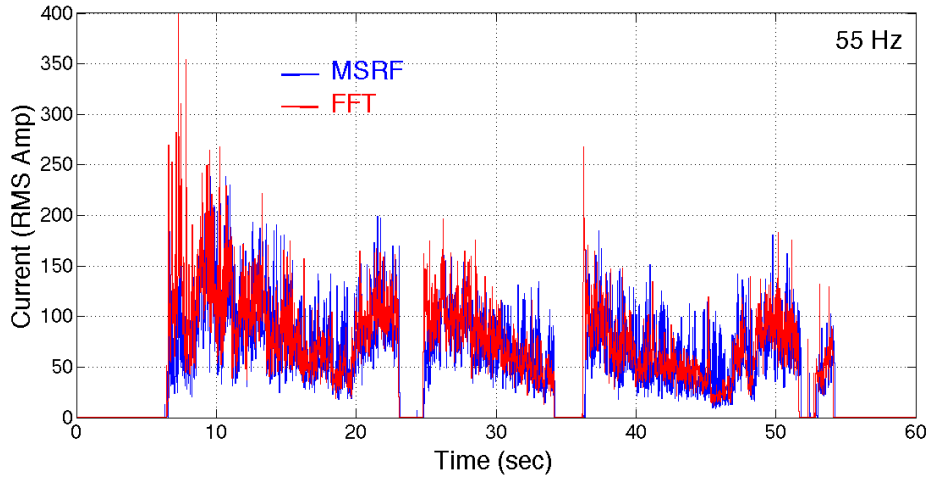
(h) $f_{iH}=40$ Hz



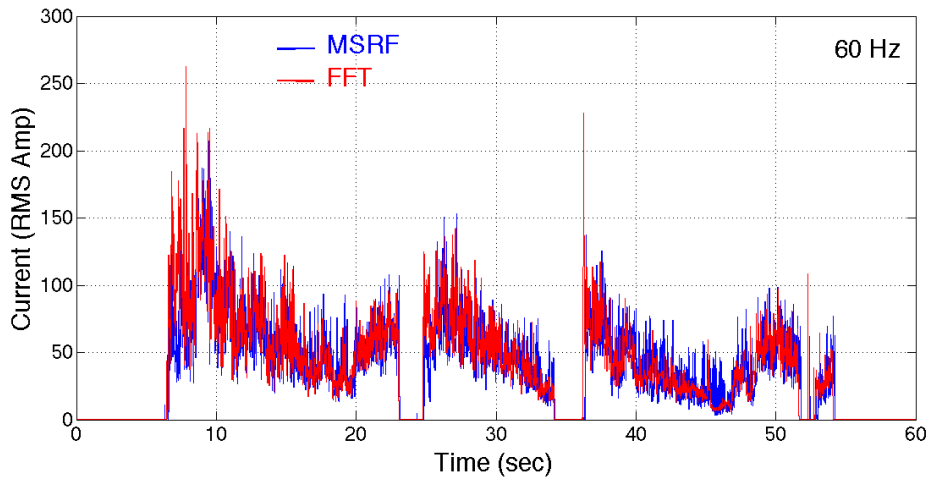
(i) $f_{iH}=45$ Hz



(j) $f_{iH}=50$ Hz

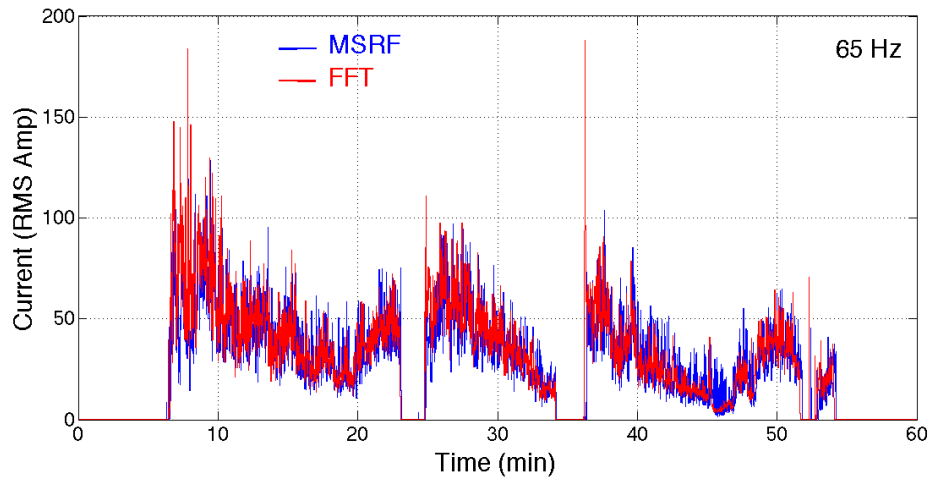


(k) $f_{iH}=55$ Hz

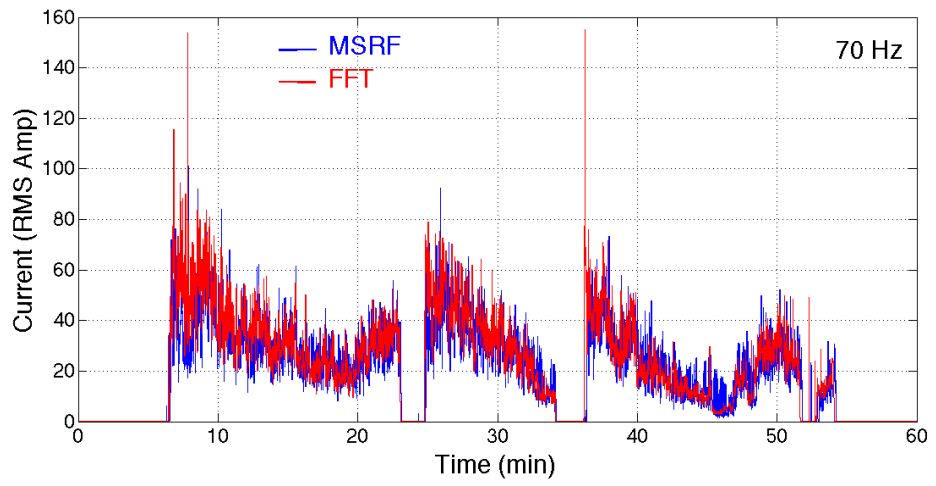


(l) $f_{iH}=60$ Hz

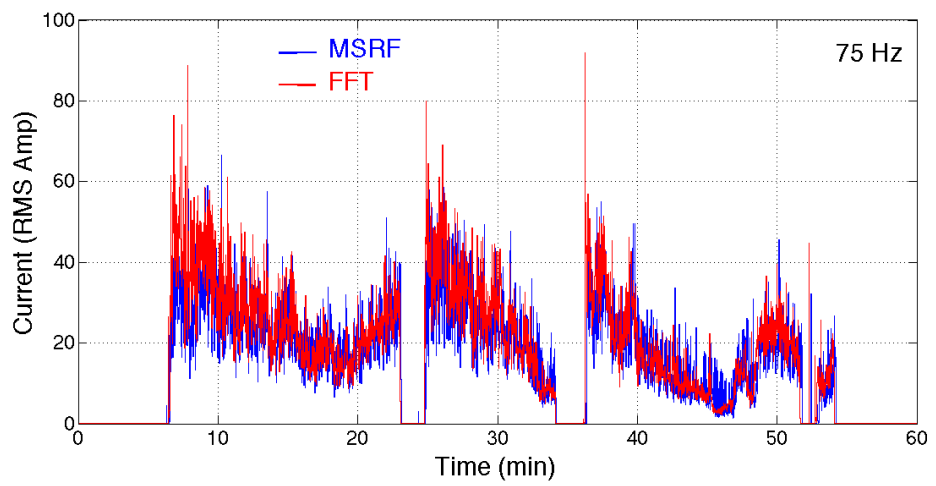
Figure 3.12: Comparison between the results of MSRF and FFT analyses for the interharmonics around the fundamental component (1-s averaged RMS phase-A currents).



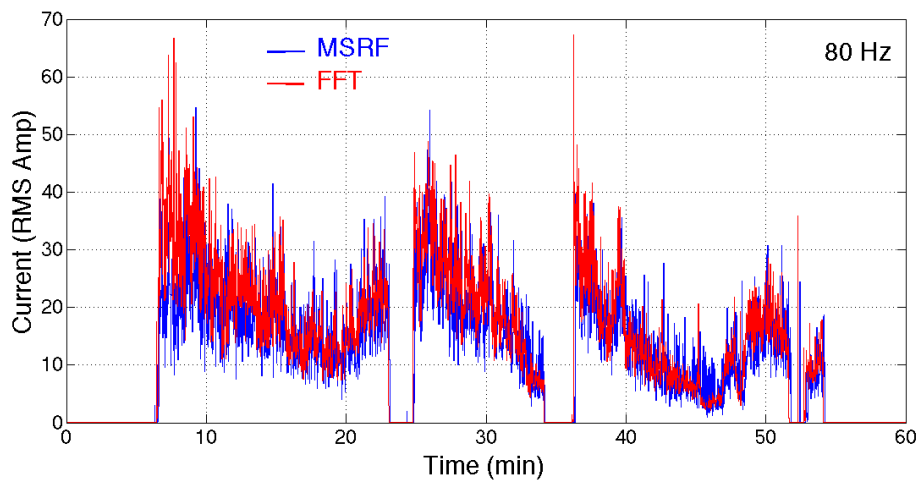
(a) $f_{iH}=65$ Hz



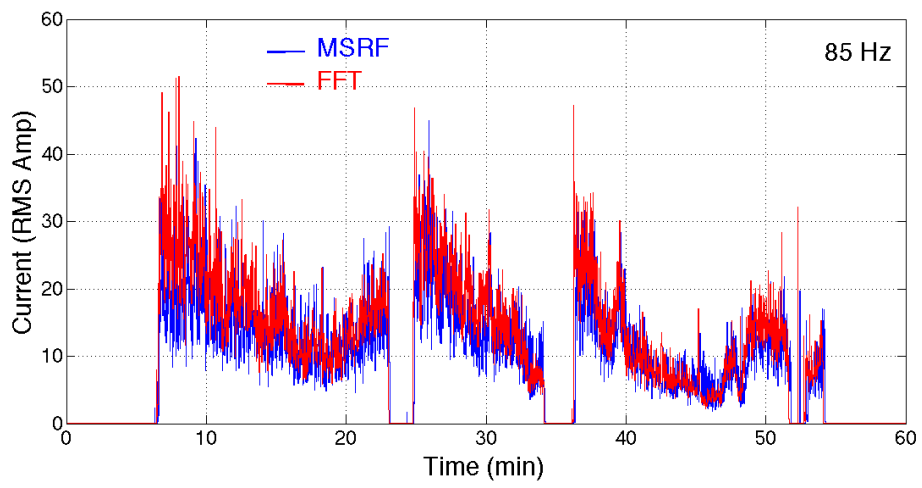
(b) $f_{iH}=70$ Hz



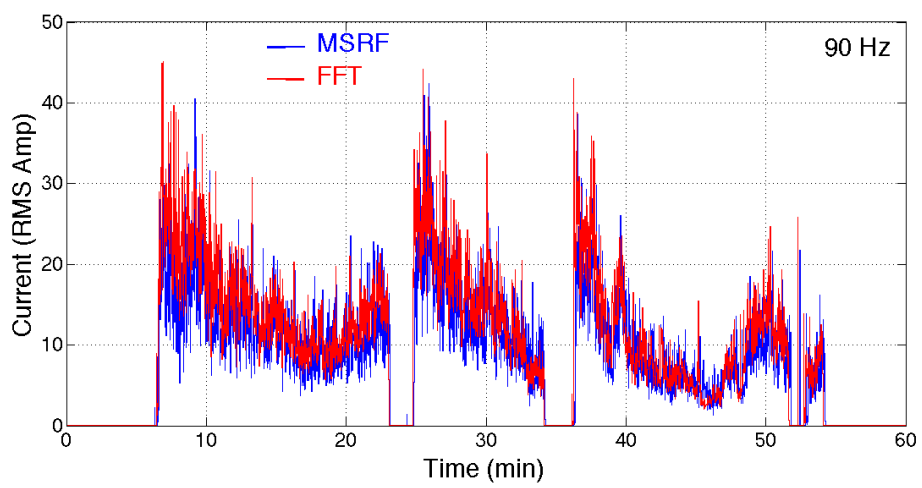
(c) $f_2=75$ Hz



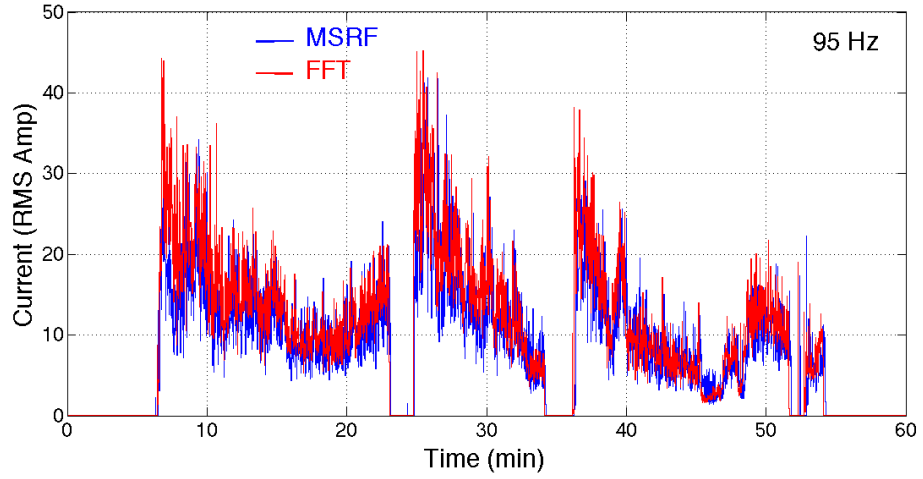
(d) $f_{iH}=80$ Hz



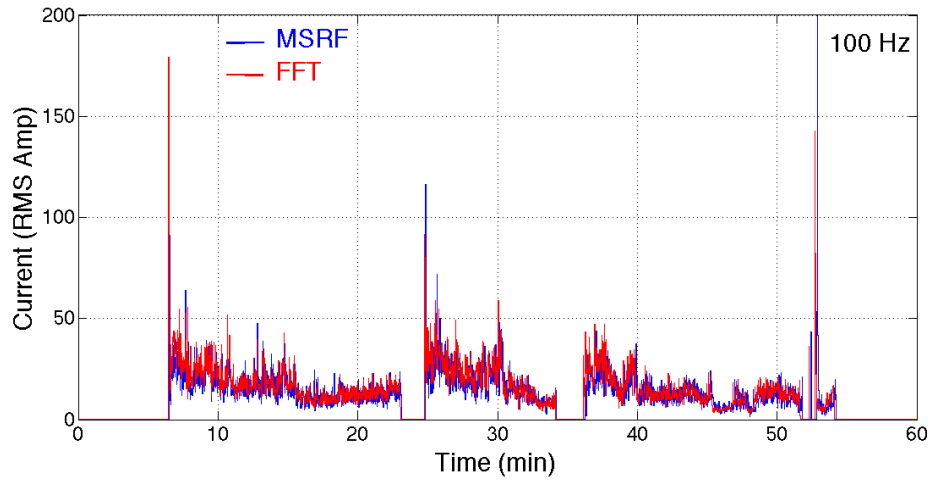
(e) $f_{iH}=85$ Hz



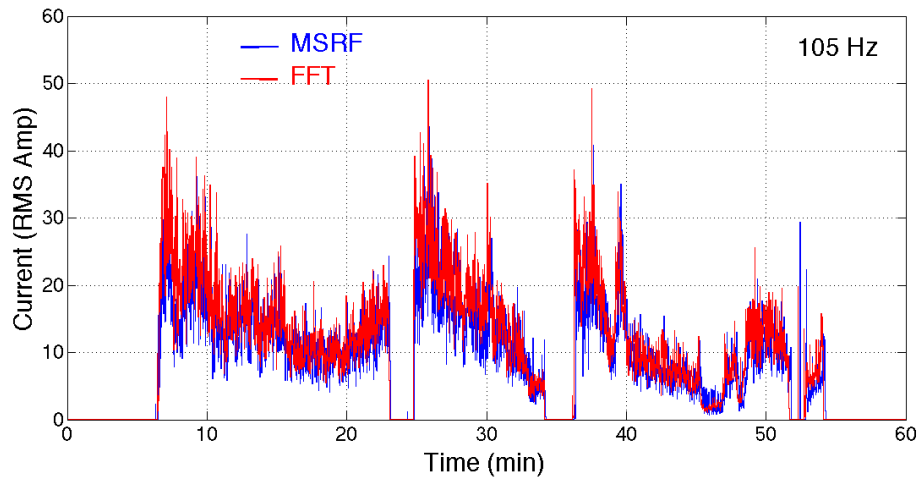
(f) $f_{iH}=90$ Hz



(g) $f_{iH}=95$ Hz



(h) $f_{iH}=100$ Hz



(i) $f_{iH}=105$ Hz

Figure 3.13: Comparison between the results of MSRF and FFT analyses for the interharmonics around the second harmonic component (1-s averaged RMS phase-A currents).

CHAPTER 4

PROPOSED METHOD

The effectiveness of the MSRF analysis has been proven in Chapter 3. For offline applications, the proposed method gives applicable and correct results. However, real-time applications require some additional care to be effective for this kind of current waveform which is highly fluctuating and rich in harmonic and interharmonic content. Causal filters with insignificant delay in response time and at the same time complex and repetitive calculations with small execution time which does not affect the performance of the countermeasures shall be implemented in the frequency decomposition analysis. In this thesis, these demanding features have been fulfilled with two novel methods which will be described next.

The first challenge faced in real-time applications is that the delay between the input and the output data which occurs due to the filters allocated inside the algorithm should be kept as small as possible. Especially for this kind of operations where the waveform under consideration changes so rapidly, this delay may cause totally different results than that is expected and the counteractions taken with respect to these results may even cause amplification of the focused harmonics and/or interharmonics instead of compensation. In a regular operation, this delay can go up to 10-cycles which makes the method impractical since the waveform changes so rapidly in every cycle as can be seen from Figure 3.1. The same duration of 10 cycles is also necessary for an FFT window for 5-Hz resolution and the FFT algorithm is powerful and fast to decompose the waveform into its spectral components. On the other hand, for the MSRF method, the filter delay is directly proportional to the filtering performance of the filter in most of the cases. In other words, the sharper the filter, the slower the

response is and vice versa. When the delay is aimed to be minimized, the filtering performance has to be sacrificed. In order to demonstrate this issue, the plot in Figure 4.1 has been generated for the second harmonic ($f_2 = 100\text{Hz}$). The well-known moving average filter performance is compared to that of the Butterworth filter by computing second harmonic of the actual EAF current waveform by MSRF analysis. Moving average filter is much-used in real time applications since it is easy to implement and does not require samples from future. However, it can be easily observed from this figure that the filtered waveform consists of many other harmonics which means that moving average filter is ineffective when the waveform fluctuates too much.

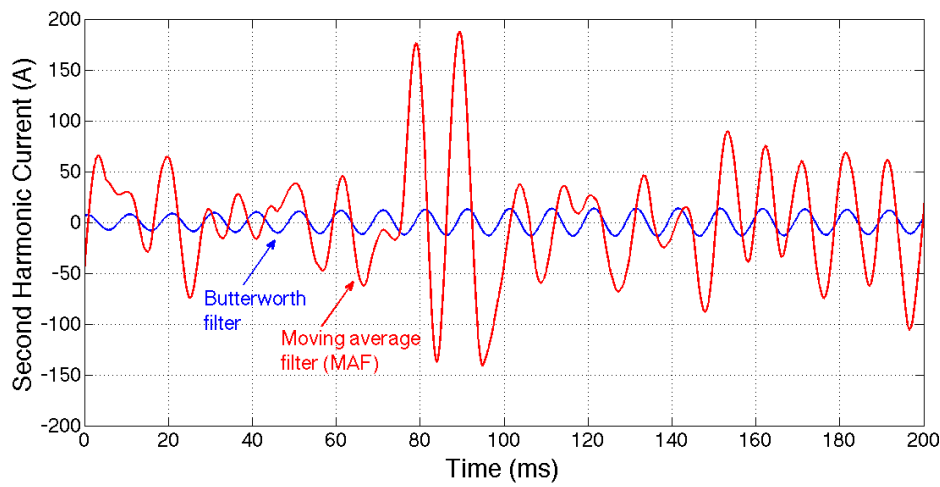


Figure 4.1: Comparison of the second harmonics produced by MSRF with Butterworth filter and Moving average filter in 200ms.

In this thesis, Kalman filter has been proposed for filtering purposes in order to make use of the prediction property of the Kalman filter. This property not only helps to increase the response time of the filter, but also keeps the filtering performance high compared to the similar low pass filters with the same delay time. Kalman filter has been used in order to decompose the waveform into its frequency components at the same time with any predetermined resolution. It is used as a substitute for the FFT analysis with some advantages and disadvantages [13]. In this thesis, Kalman filter has been used as a low pass filter with prediction capability in order to obtain the DC components of the waveform after dqo transformation. That is to say, the low pass filters used in Figures 2.10, 2.11 and 2.12 are replaced by Kalman filters.

MSRF analysis includes repetition of the transformation for each harmonic and/or

interharmonic since the procedures in Figures 2.11 and 2.12 have been used with different respective rotational speeds. Besides, the transformation matrices consist of some difficult calculations as trigonometric functions and matrix multiplications that need hundreds of clock cycles. The data transfer can also take a majority of the available time if a great care for this job is not given. Especially for the operating system-based implementations, one can easily say that the only drawback that prevents a fast real-time operation is the time that takes during the data transfer. Therefore it is a formidable job to finish extracting 300 harmonics in 40 μ s-period, which is the time between two samples of the waveform for the sampling rate of 25.6kHz. In this thesis, GPU-based hardware has been chosen to be responsible for the execution of the proposed method. In real-time harmonic analysis, the decomposition method needs to be completed before the next sample is taken, and the sampling frequency should not be reduced in order to keep the resolution of the waveform high. For the sampling frequency equal to 25.6 kHz as is the case in this thesis, the whole process including the calculations and the data transfer has to be done in 40 μ s-period.

4.1 Kalman Prediction Filter

One of the main application area of Kalman prediction filter is the target tracking systems since it gives fast and accurate results in the existence of noisy measurement data due to the rough environment. The primary reason to have a successful performance for this kind of application is the predictable movement of a physical target since the direction and the speed of the target can not alter from a negative maximum value to a positive maximum in two consecutive measurements. Same is true for the application mentioned in this thesis. Even if the amplitudes of each cycle change abruptly, the voltage and current waveforms need to track almost a sinusoidal waveform due to the physical elements consisted in the electrical systems, such as inductors and capacitors. If the sampling frequency is high enough, consecutive data give a similar characteristics as the ones mentioned in the target tracking system. Therefore, Kalman filter has been preferred to accomplish the tracking of the DC values in this thesis.

The standard Kalman prediction filter has been used in order to obtain the DC com-

ponent out of d - and q -component resulted from the transformation of the three phase system into synchronously rotating reference frame. However, the purpose of the Kalman filter has been modified slightly and benefited from the advantage of its prediction capability. It is well-known that Kalman filter predicts the next state and updates it with the upcoming measurement data. The measurement data is assumed to be noisy and with the coefficients chosen beforehand to calculate the error covariance, how much of the measured or calculated data should be taken into consideration and how much should be counted as noise or error are determined. With this knowledge in mind, Kalman filter modifies itself according to the reliability of the measurement and calculated data. In short, if the measurements seem to be inconsistent with the information provided before, Kalman filter evolves and starts not to take the measurements into consideration much and it produces its results according to its calculations. On the contrary, if the calculations give incoherent results, filter sticks with the measurements and follow their footsteps. In this thesis, the DC value corresponding to the harmonics and interharmonics is considered to be the measurement noise and the prior DC value guess of the analyzed harmonic or interharmonic frequency is provided approximately. By this way, the Kalman filter follows a DC value by gently modifying its amplitude according to the measurements. The efficiency of this method will be proven next. The superscript "-" demonstrates the priori estimate notation. If this superscript does not exist then it is called posteriori estimate.

$$\begin{aligned}\hat{x}_k^- &= A\hat{x}_{k-1}^- + Bu_{k-1} + v_{k-1} \\ P_k^- &= AP_{k-1}A^T + Q\end{aligned}\tag{4.1}$$

$$\begin{aligned}K_k &= P_k^- H^T (HP_k^- H^T + R)^{-1} \\ \hat{x}_k &= \hat{x}_k^- + K_k(z_k - H\hat{x}_k^-) \\ P_k &= (I - K_k H)P_k^-\end{aligned}\tag{4.2}$$

Regular Kalman filter time and measurement update equations can be stated as in 4.1 and 4.2 respectively. Here x is the state vector which is chosen to be 3-dimensional in this thesis with each dimension representing position, speed and the acceleration of the states respectively. A is the 3x3 dimensional matrix that shows the relation

between current state and the previous one. B represents the relation between the control input model and the state which is chosen to be zero in this case. The process noise, v , is ignored in this thesis. The error covariance P is calculated by the state transition matrix and the constant process noise covariance, Q , and later, it is updated by the constant measurement noise covariance, R . The constant Q and R are the predefined filter parameters that helps to determine the magnitude of the noise to be expected. Lastly, K represents the Kalman gain and H shows the relation between the measurement and the state.

The values of mentioned parameters used in this thesis are summarized in 4.3. The values of the elements in matrix P are chosen as follows. First of all, the offline implementation of the proposed method is achieved with a zero-phase low pass filter. In this thesis, this is achieved by a Butterworth filter with 2.5 Hz cut-off frequency and predefined *filtfilt* MATLAB function is used instead of *filter* function in order to obtain zero-phase response. Note that *filtfilt* function filters the waveform two-times, one of which is forward filtering and the other is the backward filtering to compensate the phase-lag. Therefore, the same performance should not be expected from these two functions. When the filtering performance is found to be satisfactory, the square of the maximum error between the calculated dq -components and their extracted DC values is measured from the plotted waveforms to find the initial guess of the first component of error covariance matrix. In this case, the element at p_{11} is chosen to be 300^2 which means that the maximum difference between the dq -components and their DC is 300 A. The second element of this matrix is chosen in a similar way. This time, the maximum difference between the differentiated values of the dq -components and the differentiated value of the DC-component is selected. Therefore, the p_{22} value is chosen to be 1000^2 which shows the speed of the difference is maximum 1000 A/s. Lastly, the waveforms calculated to find the speed of the dq -components are differentiated for the second time in order to find the difference in acceleration rates. Therefore, the initial guess of the p_{33} value is chosen to be $1e8^2$ which indicates the difference in acceleration is maximum 100 MA/s². Noise covariance, R is generally selected to be equal to the p_{11} component of the error covariance matrix, P . It should be considered that the noise covariance is not chosen to be a strictly constant value. This value can be modified to the different environments

during the process time in order to have an adaptive Kalman filter.

$$\begin{aligned}
T &= 1/25600 \\
P &= \begin{bmatrix} 300^2 & 0 & 0 \\ 0 & 1000^2 & 0 \\ 0 & 0 & 1e8^2 \end{bmatrix} \\
A &= \begin{bmatrix} 1 & T & \frac{T^2}{2} \\ 0 & 1 & T \\ 0 & 0 & 1 \end{bmatrix} \\
B &= \begin{bmatrix} \frac{T^3}{6} \\ \frac{T^2}{2} \\ T \end{bmatrix} \\
H &= \begin{bmatrix} 1 & 0 & 0 \end{bmatrix} \\
R &= 300^2 \\
Q &= \frac{1}{T^2}
\end{aligned} \tag{4.3}$$

The block diagram of the recursive Kalman filter implementation is shown in Figure 4.2. As an example, the calculated d-component of the fundamental frequency and its Kalman filtered version has been shown in this figure. The response delay time and the filtering capability of Kalman filter will be investigated later in detail, however the tracking performance of the Kalman filter is clearly seen in this figure especially in between 30-40s. Here, k stands for the data index where $k - 1$ is the previous data in reference to the current time. For the first step of the overall process flow presented in this figure, the estimates of the state and the error covariance are calculated by the initial conditions. When the measurement is taken, the estimates are corrected, and these corrected estimates are then used as the inputs of the next estimation stage. If the noise covariances are selected as constants, then the error covariance and the Kalman gain eventually converge to constant values. This is also the case in this thesis. For example, with the parameters assigned as in 4.3, the final values of the P

and K are reflected in 4.4.

$$P = \begin{bmatrix} 31 & 136 & 300 \\ 136 & 900 & 2640 \\ 300 & 2640 & 11630 \end{bmatrix}, K = \begin{bmatrix} 3.45e^{-4} \\ 0.0015 \\ 0.0033 \end{bmatrix} \quad (4.4)$$

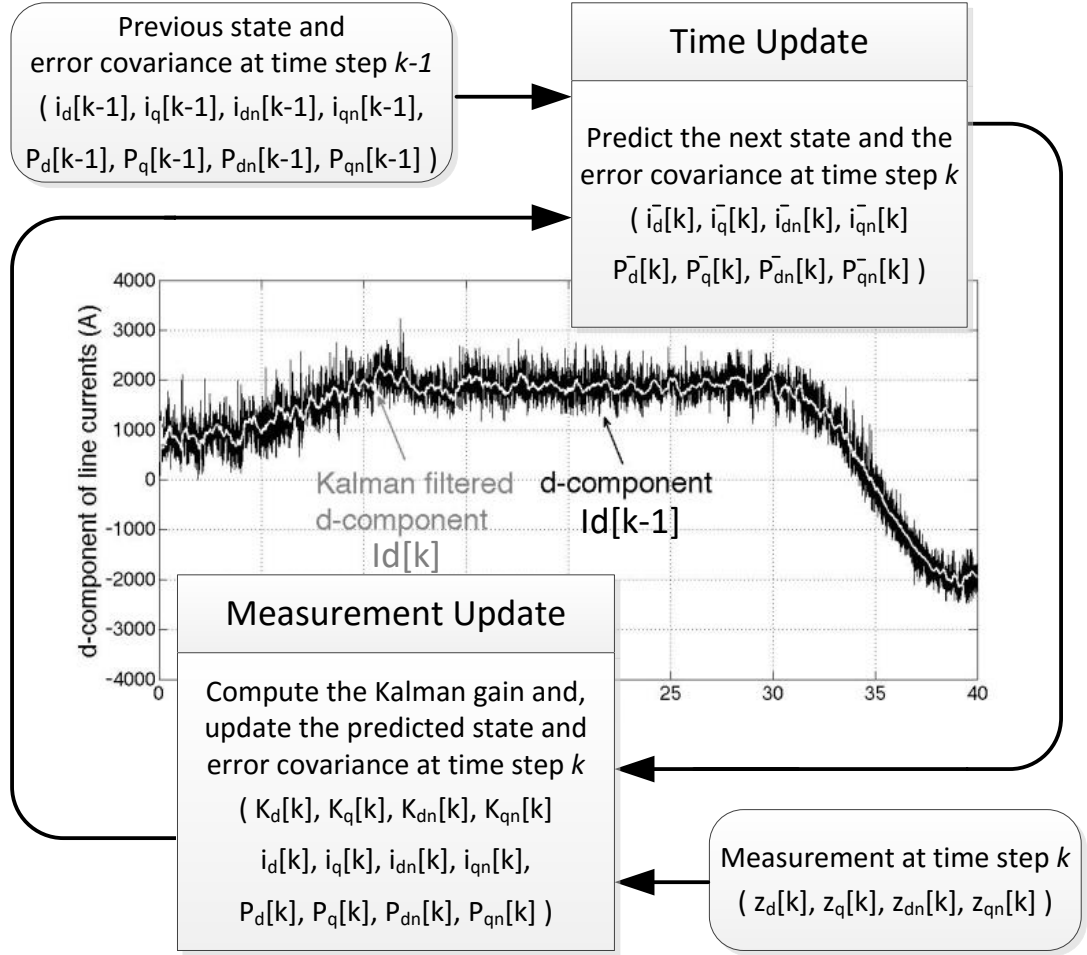
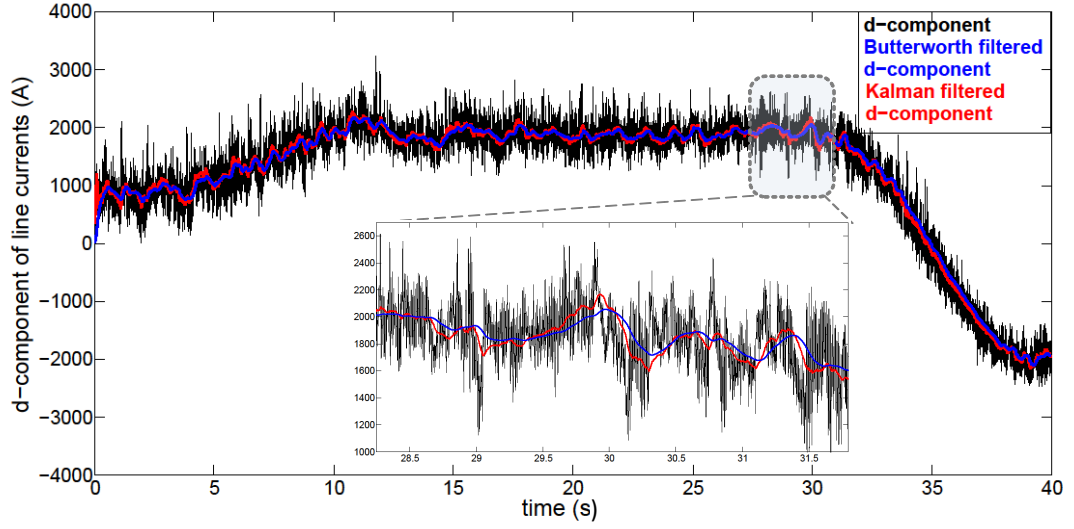


Figure 4.2: Flowchart of Kalman measurement and time update algorithms applied to positive- and negative-sequence components of all harmonics and interharmonics (k denotes the sampling index, where time step is $\Delta t = t_k - t_{k-1} = 40\mu s$).

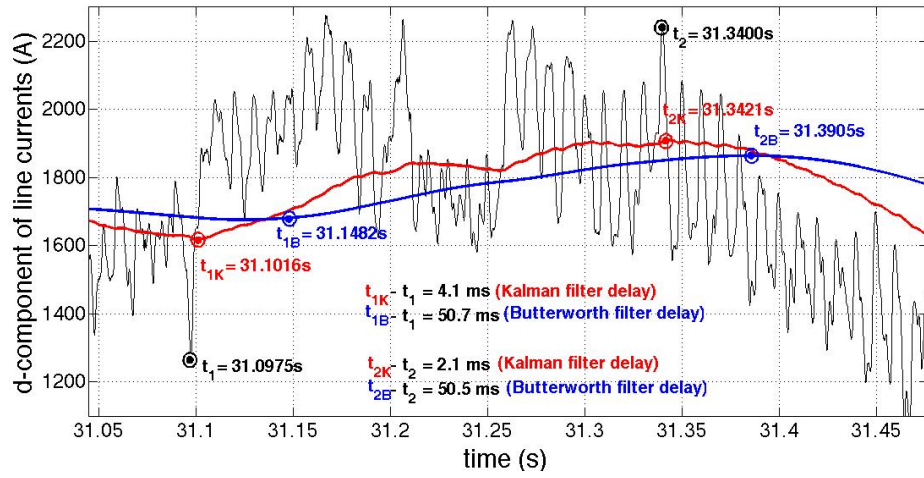
In order to compare the performances of the Butterworth and the Kalman filter, Figure 4.3 has been created. The reason of choosing the Butterworth filter instead of filters like Bessel, Chebyshev, elliptic, and etc. for comparisons is the fact that these different kind of low pass filters eventually have similar behaviors and the Butterworth is found out to have the optimum characteristics among all for this kind of appli-

cations. Meanwhile, the parameters of both filters are kept constant throughout the entire thesis in order to keep the results comparable. Figure 4.3a shows the filtered d-component of the positive-sequence fundamental frequency by Butterworth filter and by Kalman filter. The close-up of 3s-period is also presented in this figure to show the tracking performances in more details. It is apparent that the former cannot track the variations quickly, on the other hand the latter can keep track of the even local changes. As a reminder, the aim is to obtain the DC component of this parameter. When taken into account of the extraction of the DC component in real-time, it is tough to decide which variations are caused by the natural and nonrecurrent amplitude fluctuations which are due to the modulation of the amplitude by another frequency. In this kind of situations, the best practice is when course of the amplitude stays higher than the previous state for a while, than the DC value needs to keep track of this consistent amplitude. This concept can be seen from this figure and it is obvious that the Butterworth filter is insufficient to follow the consistent changes. 4.3b is the ms-level response delay comparison figure. The delay time of Kalman filter changes according to the waveform characteristics. Course of the event starts to change at t_1 instant and the Kalman filter responded to this change at t_{1k} whereas the Butterworth filter corresponded to the same event at t_{1B} . There is a 12.5-times quicker response in the former filter. The second sample case starts at t_2 and the differences in response time of these two filters go up to 25 times. There is one more thing to mention that the filtering performances of both filters are not so different than each other. For the same performance the Kalman filter response is proven to be much faster than the Butterworth filter.

Lastly, Figure 4.4 shows the speed of the response of the Kalman filter to a sudden change. The actual waveform belongs to the EAF transformer energization before 3rd charging period. There is an abrupt increase in phase current and the reconstructed phase current by the addition of all harmonics and interharmonics up to 1.5kHz in 5-Hz resolution could follow this jump without oscillation afterwards.



(a) 40s response



(b) 0.4s response

Figure 4.3: Comparison of time delays in LPF blocks in Figures 2.10, 2.11, and 2.12 corresponding to Kalman- and Butterworth-filter. Subscripts K and B denote Kalman- and Butterworth-filter, respectively.

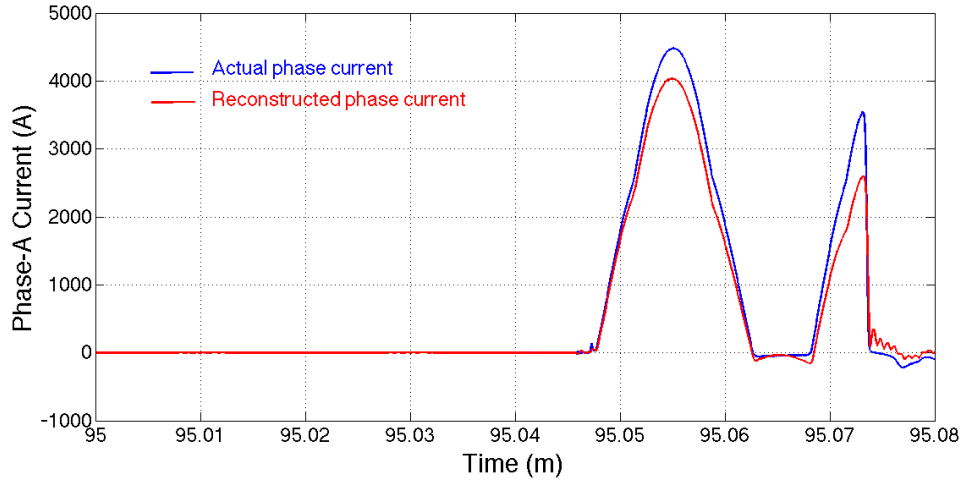


Figure 4.4: Response of the Kalman filter to a sudden jump.

4.2 GPU-based Implementation

MSRF algorithm is suitable to be executed in parallel during the computation of harmonics and interharmonics since the calculations include repetition of the same procedure with a single input. There are some compatible hardware options that can be used for this kind of application such as GPU, CPU, FPGA, and etc. They all have some application specific superior performances over each other, however GPU steps forward for MSRF algorithm and its utilization area. GPU is a popular hardware among the image processing applications. However, power electronics area has not taken the advantage of GPU very much. Therefore, it is novel to introduce this hardware to implement the MSRF algorithm. There are several advantages of GPU which recall the GPU to mind in the first place. With the technological advance, GPU became more and more powerful with smaller size and price. Nowadays, GPU has more computing power per its price than a similar performance FPGA and CPU. In addition to this, GPU has effectively unlimited I/O channels comparing the FPGA since the data transfer is managed by software and the limitation depends only on the memory whereas the limitation depends on the number of physical I/Os in FPGA. On the other hand, for micro-second-latency real-time applications, CPU lacks of precision in every execution time, since the timing of the interrupts are managed by the operating system and the operating system puts all the interrupts in an order and allows the one with the most critical mission for its survival. This condition can be

overcome by a real-time operating system, however it is cumbersome and expensive for these kind of operations.

MRSF algorithm is implemented in three different GPU platforms as part of this work which are NVIDIA's Jetson TK1, NVIDIA's Jetson TX1 and NVIDIA's GeForce GTX 970. The first two are the developer kits with CPU and GPU embedded in one credit card size chip. The last one is a powerful graphic card connected to the slot of the desktop computer motherboard. In this thesis, NVIDIA's Jetson TX1 developer kit has been used which occurred to be the optimum one in computing power, cost and size among three of them. It has 256 CUDA cores that can be paralleled delivering over 1 teraflops of performance. NVIDIA developed an application programming interface (API) named as Cuda. Cuda recognizes C-type programming language and when interfacing with GPU for parallel processing, it has its own syntax. Cuda is a user friendly and easy programming language, therefore it is suitable for developers.

4.2.1 Code Development and Optimization in CUDA

Code development in CUDA language is not a tough job to achieve. However, the challenging part lies on the optimization of the generated code. It is advised to develop the code by following the steps mentioned in Figure 4.5. It helps to decrease the time consumed on the optimization period. Otherwise, it is easy to be caught up between optimization and the code generation steps. Therefore, throughout this chapter, the code snippets will be given as well as the optimization procedure benefited from.

Figure 4.6 shows the code flowchart of the MRSF algorithm. The repetition of the entire steps occurs for every upcoming data which is suitable for a real time operation. The first step is responsible from the definition of all the variables used in CPU and GPU memory. Once they are created, they are only modified and are not freed until the lifetime of the execution. The sample codes are given in 4.1, one for CPU and one for GPU. The d in front of the variable shows the variable is created on the device which is in this case the GPU memory. The size of the vectors are chosen as 300 which means that the algorithm will be applied to find 300 harmonics and interharmonics with 5Hz resolution (which consists of the frequencies: 5, 10, 15, ...,

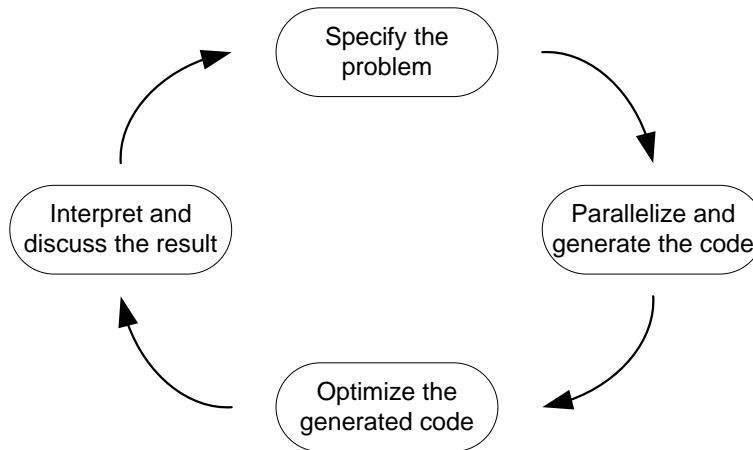


Figure 4.5: Best practice of the design cycle for the application developers.

1500 Hz).

Code Snippet 4.1: First step of the MSRF algorithm mentioned in 4.6

```
float *ia_new = (float*)malloc(300*sizeof(float));
cudaMalloc((void**) &d_ia_new, sizeof(float)*300);
```

The second step is to execute the trigonometric functions beforehand once for all and to form a look-up table in order to be used in transformation steps. Since the calculation of these functions requires some time, it would be time consuming to find them in every loop. For the same reason of step one, the time required to generate this look-up table is excluded from the overall execution time calculations. The sample calculations is shown in 4.2. One cycle trigonometric function results for each harmonic and interharmonic frequency are included in this table and since the largest period ($=200\text{ms}=5120$ sample) belongs to the 5Hz, the vector consists of 300×5120 elements. For the rest of the frequencies, the values are repeated since they have smaller periods than 5Hz.

Code Snippet 4.2: Second step of the MSRF algorithm mentioned in 4.6

```
for i=1:300
    for k=1:5120
        sinus[i*5120 + k]=sin(2*PI*(i+1)*5*k/25600);
        ...
    end
end
```

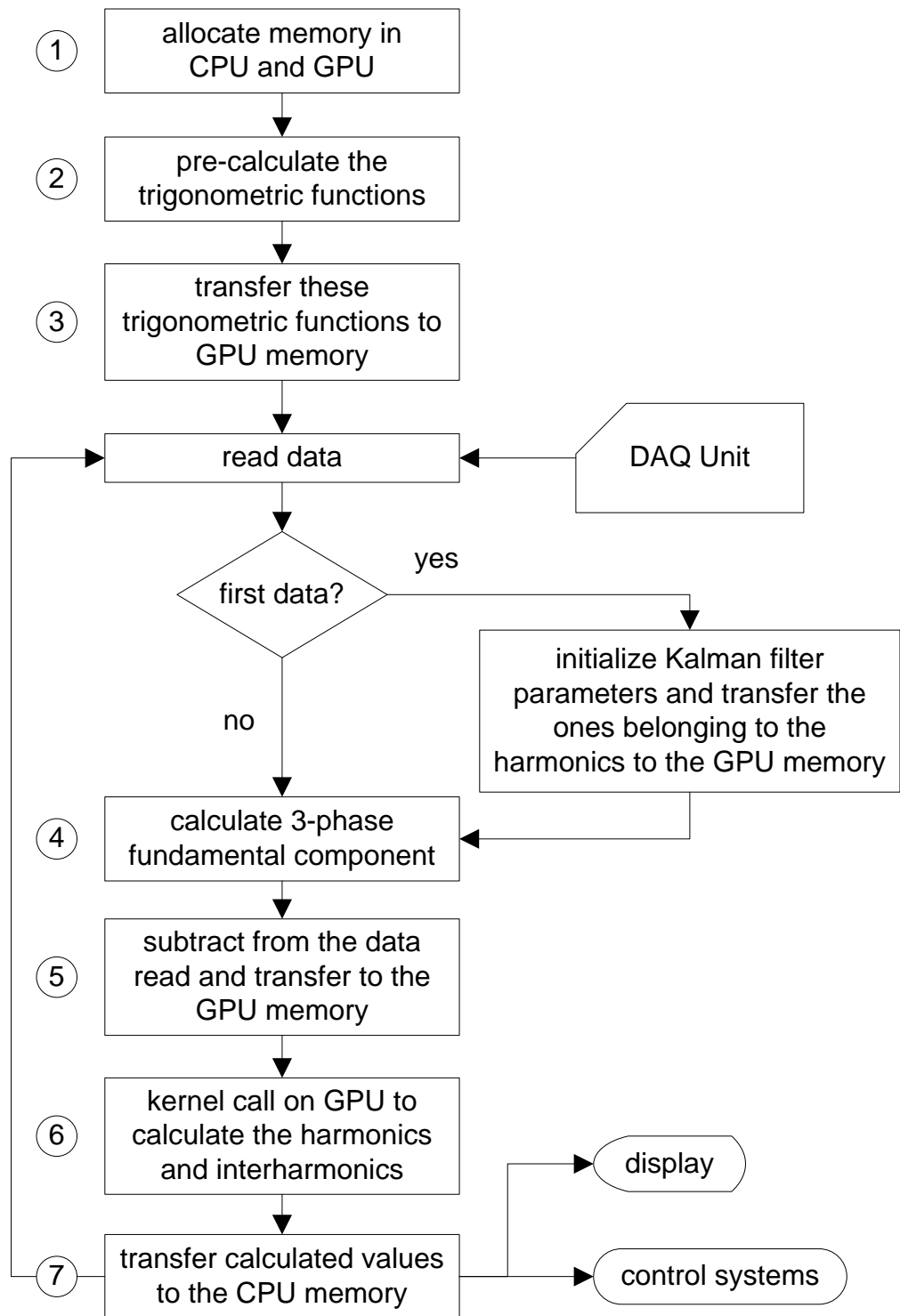



Figure 4.6: Generated code flowchart for MSRF algorithm implementation.

There is a concept which is called the coalesced memory access as described in Figure 4.7. The most time consuming process in a program flow is the memory transactions. When an access to an array element is required, a block of memory is called each time. If the other threads uses elements of the array from this same memory block at the same time, then there is no other memory transaction occurs which reduces the execution time considerably. Otherwise, another block of memory is called, and the time spent in the memory doubles for this operation. The worst case is to call a different chunk of memory for each array element. In order to increase the coalescent access to the memory, the places of the elements of the trigonometric function vector is chosen carefully. For example, at each loop iteration for each data, the first 300 elements of vector named *sinus* is called because the elements that will be used to calculate all the harmonics and interharmonics are located consecutively to the vector.

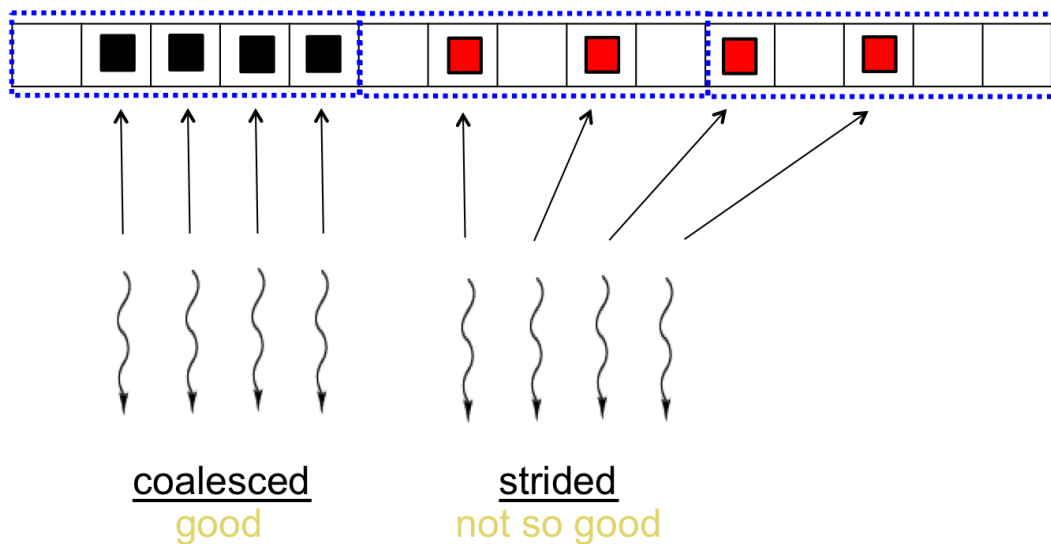


Figure 4.7: Coalesced memory access.

The look-up table is transferred to the GPU memory only once at the beginning of the algorithm and used in every calculations. For the code optimization, especially for the equations carried on GPU, when the complexity of each mathematical operation increases, the efficiency of the GPU cores drop resulting a considerable increase in the execution time. In 4.3, a sample code snippet is shown. *cudaMemcpyHostToDevice* means the memory transfer occurs from host (CPU) to device (GPU). As mentioned before, the TX1 developer kit is an embedded plat-

form which has a shared memory available for both CPU and GPU. Therefore, it takes insignificant time to transfer a chunk of memory from CPU-to-GPU or vice versa.

Code Snippet 4.3: Third step of the MSRF algorithm mentioned in 4.6

```
cudaMalloc((void**) &d_sinus, sizeof(float)*5120*300);  
cudaMemcpy(d_sinus, sinus, sizeof(float)*5120*300,  
           cudaMemcpyHostToDevice);
```

At the fourth and fifth steps, the proposed method explained in details in previous chapters is applied to the data read to calculate the fundamental component and subtract this result from the data read in order to obtain the plain harmonic and interharmonic content of the actual signal. Then the result is sent to the GPU memory in order to parallel the decomposition of the harmonics and interharmonics. The only memory transfer from CPU to GPU repeated at every loop iteration occurs at this stage for each three phase signal as shown in 4.4. As mentioned before, the less the time spent on the memory transfer, the more efficient the code is. There is one more issue that should be paid attention to that the choice of the variable types is important. Double precision variables always consume much more time than single precision variables and integers. In addition to this, there is limited amount of registers responsible from the operations consisting of double precision numbers. Therefore, even if the number of the arguments to be launched is small enough to be executed in parallel according to the capacity of GPU, the operation may not always be initiated due to the lack of registers. It would be a good practice to reduce the number of the double precision variables even if it costs some more calculation steps to obtain the necessary accuracy. Note that GPU is highly efficient especially in integer arithmetic operations.

Code Snippet 4.4: Fourth and fifth steps of the MSRF algorithm mentioned in 4.6

```
cudaMemcpy(d_iaharm, &ia_harm, sizeof(float),  
           cudaMemcpyHostToDevice);
```

In step six, the parallel operation is initiated by calling the kernel. The syntax of a kernel is shown in 4.5. The `<<<>>>` Cuda language extension is used to launch a kernel. The numbers between them indicates the grid and the block sizes. In the first case, the grid size is chosen to be 4 which represents the positive- and negative-sequence dq -components. On the other hand, the block size is set to 300 which shows

that the decomposition algorithm is applied to find 300 different harmonics and interharmonics. In this case, a total of $4 \times 300 (=1200)$ kernel is launched in parallel. For the second case, grid size, 6, represents the number of three phase positive- and negative- sequence components. Block size is determined by the same reason mentioned above. This time, the total number of kernel launch becomes $6 \times 300 (=1800)$.

When the threads are launched, there is no guarantee of which one to finish the assigned task first even if the tasks were exactly the same. The so called *racecondition* is described in Figure 4.8. At every launch of the kernel, the order can change and it is impossible to know or presume which thread will be executed when. For example, assume that two distinct threads have two different assignments, one of which decreases the value of a variable by one, and the other one increases the value of the same variable by one. The resulting value of this variable will never be certain and may change at every different kernel launch. However, there are some synchronization functions to prevent this situation. In 4.5, it should be realized that there is an expression between two kernel calls. The expression of *cudaDeviceSynchronize()* is called between two kernels, so that one can be sure of that the tasks of the threads launched with the above kernel are completed before the threads belonging to the next kernel are launched. In other words, the GPU functions are serialized and the result of the first function can be used as a variable of the second function. In this case the computation of the positive- and negative-sequence of the *dq*-component must be finished before the calculation of the positive- and negative-sequence of three phases starts. There is one more function that serves to the same purpose which is called *__syncthreads()*. The first one is called from the host, on the contrary this one is called from the device. In this thesis, the synchronization function is called after the calculation of positive- and negative-sequence *dq*-components, prediction of the state variable and error covariance, and multiplication of the *H* matrix with the predicted state variable.

Code Snippet 4.5: Sixth step of the MSRF algorithm mentioned in 4.6

```
HARMMain1<<<<4, 300>>>>(var1, var2, var3, ...);
cudaDeviceSynchronize();
HARMMain2<<<<6, 300>>>>( var1, var2, var3, ...);
```

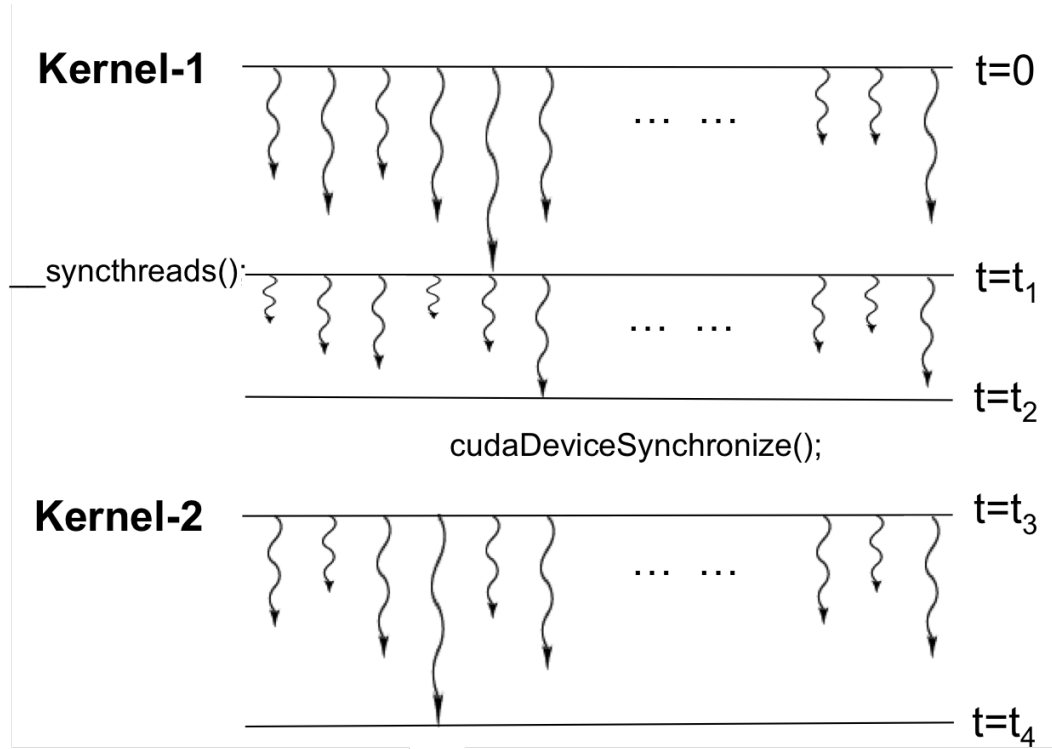


Figure 4.8: Race condition and synchronization techniques.

The last step includes the transfer of the calculated variables from GPU memory to CPU memory. The code snippet is shown in 4.6. The syntax is similar with the one in step 5. This time the reserved key word is *cudaMemcpyHostToDevice* since the direction of the transfer has changed. After this stage, the results can be send to the control systems of the advanced technology compensation systems or can be observed on the screen in real time which is the case in this thesis.

Code Snippet 4.6: Last step of the MSRF algorithm mentioned in 4.6

```
cudaMemcpy(d_ia_harm, &ia_harm, sizeof(float),
           cudaMemcpyHostToDevice);
```

4.2.2 Developed System on GPU Framework

Algorithms well-suited to GPU architecture are the ones that are data parallel and throughput intensive. Since computer vision and video/image processing applications are pixel-based, the algorithms possess these properties, thus being very well suited to general purpose GPU (GPGPU) technology. In power electronics area, GPU does

not gain so much attention, moreover it has never been utilized in the literature for the applications similar to the one proposed in this thesis. However, due to the increase in nonlinearity and the number of the power system loads, the waveform decomposition algorithms become more complex and iterative which requires a massive computational power with parallel process capability. Therefore, the need for the hardware such as FPGAs and GPUs which are able to implement multiple and independent tasks at the same time arises day by day. The rest of this chapter will be focused on MSRF analysis employed on a GPU framework for microsecond latency necessary for real-time operations.

As mentioned earlier, in this thesis, a spectrum decomposition method is developed by the NVIDIA Jetson TK1 Developer Kit to calculate all the harmonic and inter-harmonic current waveforms which can be used as a reference signal for the control systems of advanced technology compensation devices. The primary reason to employ this CPU/GPU embedded development kit instead of the traditional GPU computing method is that, it is able to communicate directly with the analog-to-digital converters, which in this case is the DAQ unit, through PCI Express. This results in decreasing the overall computational time. Advantages of GPU over its competitors, such as FPGA and CPU, can be summarized as follows:

- GPU is much cheaper than a high performance FPGA.
- It is easier to program in GPU comparing to FPGA since NVIDIA gives a great support of Cuda programming language.
- GPU has more computing power with unlimited input and output channels than FPGA.
- GPU has more computing power in parallel than a CPU and has much better real-time performance without requiring the use of a real-time operating system.

Figure 4.9 illustrates the GPU-based system for real-time determination of AC EAF interharmonics and harmonics. Voltage and current transformers are connected to the inspected transformer substation in order to obtain three-phase analog voltage (in the range of 100V) and current (in the range of 5V) waveform. These waveforms

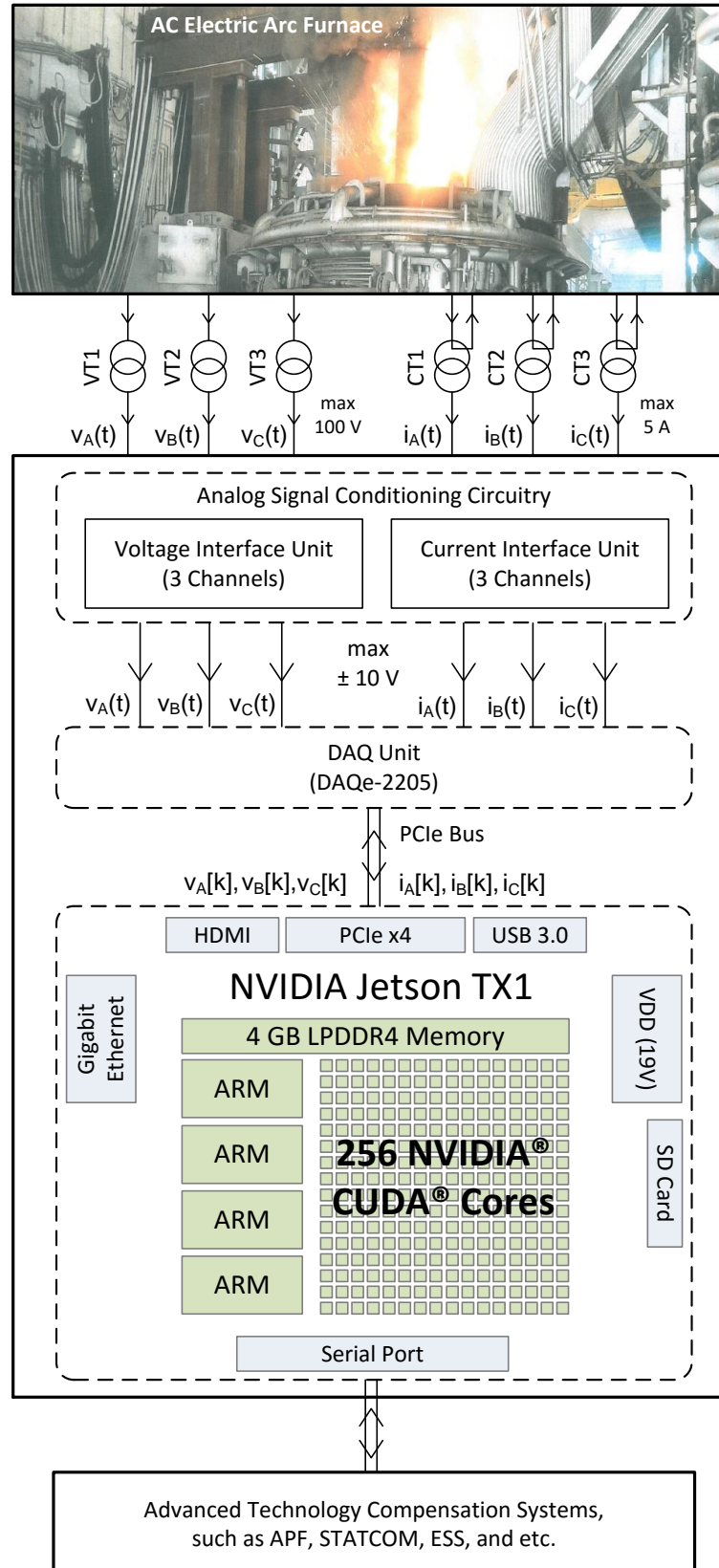


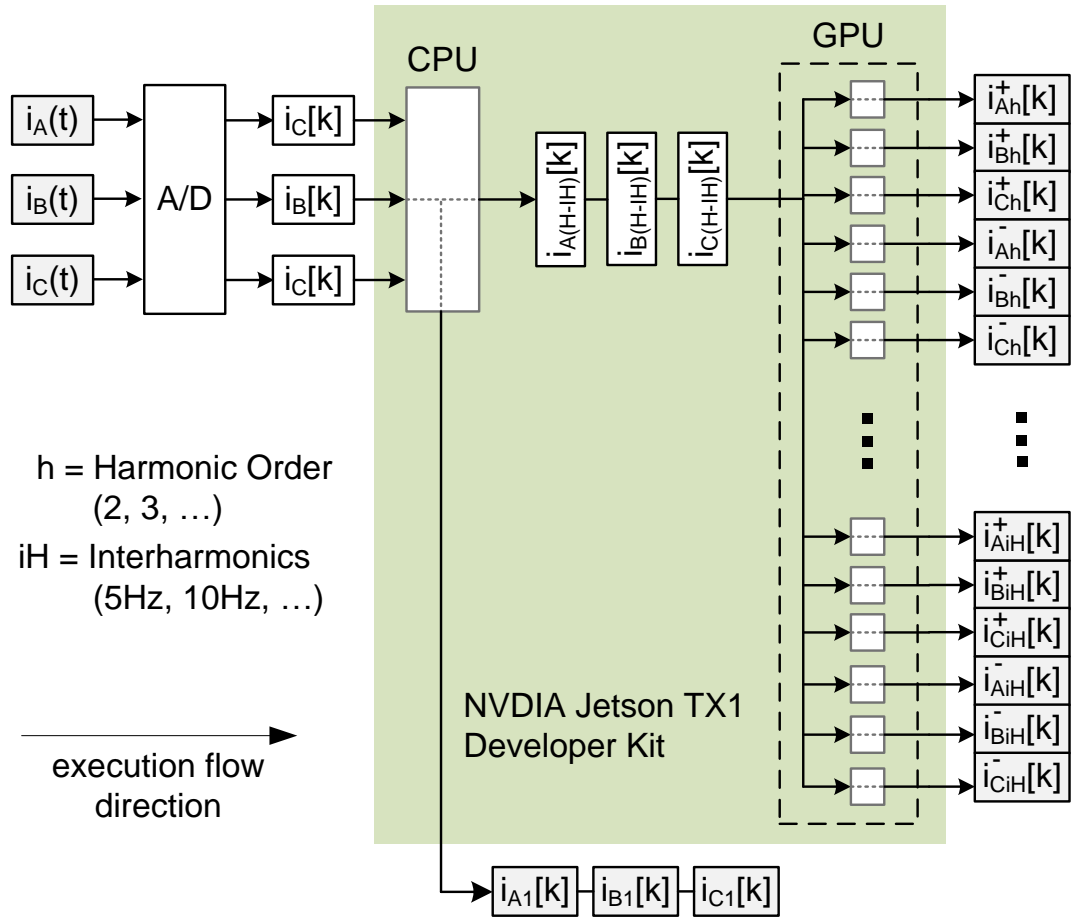
Figure 4.9: The system developed for the real-time detection of interharmonics and harmonics of AC EAFs on GPU framework.

are then processed by the analog signal conditioning circuitry so that the voltage range of the analog three phase signals become in the range suitable for the input of the data acquisition (DAQ) unit. These signals are then sampled by the DAQ unit at a rate of 25.6 kHz per input channel. This sampling frequency is enough to identify the harmonic and interharmonic frequencies up to 12.8 kHz according to the Nyquist theorem. By PCIe bus, the DAQ unit send the sampled data to the CPU/GPU integrated hardware. GPU is capable of processing these sampled data with its 256 Cuda cores and give the resulting harmonic and interharmonic information with their respective positive- and negative-sequence components at the same time.

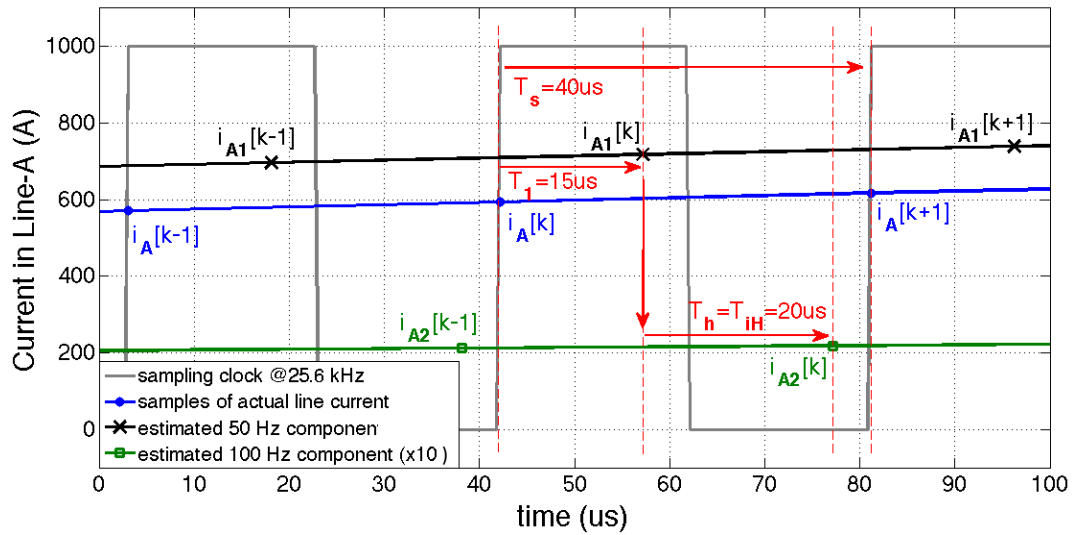
Figure 4.10a shows the data flow and where the parallel process begins. Since the first step before any of the harmonic and interharmonic component calculation, the fundamental frequency component needs to be extracted from the actual signal, this process is preferred to be executed in CPU where the cores are much more powerful than the GPU cores. In Figure 4.10b, the execution times of these two steps are given. In 40 μs available period which is due to the chosen sampling rate of the DAQ unit, 15 μs is spent by the CPU (the data transfer from CPU memory to the GPU memory and vice versa are also included inside this duration), whereas a total of 20 μs is spent by the GPU to calculate 300 different harmonic and interharmonic current components. The sample clock is given to be the reference for the initiation of the iterative process. i_A represents the samples of actual line current and i_{An} represents the estimated harmonic current, in this case fundamental and second harmonic current components are chosen as an example. The total execution time becomes 35 μs which means taht there is still 5 μs left for the data transfer. Therefore, it can be concluded that proposed algorithm executed in GPU framework is suitable for real-time applications.

4.3 Results of the Overall System

In order to verify the results, all harmonics and interharmonics obtained by the proposed algorithm with 5-Hz resolution up to 1.5 kHz are added up sample by sample and compared with the actual current waveform. Figure 4.11 shows the comparison of the actual and this reconstructed line current waveforms. It can be observed from this



(a) Data flow on high performance GPU-accelerated computing framework



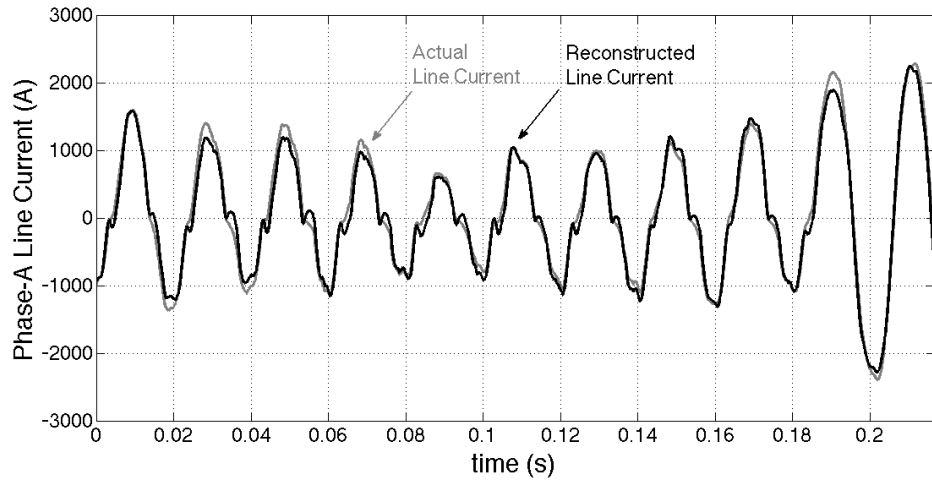
(b) An illustration of some sample calculations for fundamental and second harmonic components with the corresponding execution times

Figure 4.10: Implementation of MSRF.

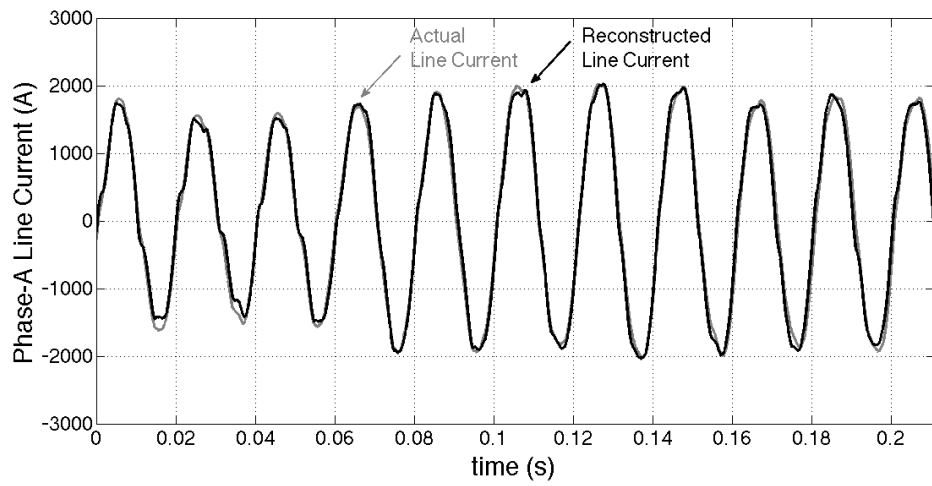
figure that the traction performance of the proposed method is very good especially when the current amplitude variation is relatively small (this generally corresponds to the three-phase current waveform behavior in melting period). In addition to this, the reconstructed current waveform can still follow the actual current waveform shape in boring period where the considerable variations in amplitude and the harmonic content can be observed frequently. As can be seen from Figures 4.12a and 4.12b, the DFT results which belong to the RMS values of fundamental and second harmonic components of the actual and the reconstructed waveforms match during a whole tap-to-tap time. These results prove that, the proposed algorithm is not only able to find the amplitudes of these harmonic and interharmonic current components, but also it is successful in finding their respective phase angles.

One of the main purpose to develop this algorithm is to create a reference signal for the control systems of the advanced technology compensation systems. In order to simulate the behavior of an active power filter, 2^{nd} harmonic subgroup (95Hz, 100Hz and 105Hz) obtained with the MSRF analysis is subtracted from the actual current waveform. The 10-cycle DFT results are given in Figures 4.13a, 4.13b and 4.13c. These figures show an important result. The proposed method not only diminishes the second harmonic and its subgroup, but it also does not amplify the interharmonics around the extracted components. There can be observed a slight increase in amplitudes of the nearby components. It is because the actual current waveform includes interharmonic components with a frequency resolution smaller than 5Hz. When some of them are extracted from the actual signal during this operation, the representation of the nearby interharmonics with DFT decomposition in 5Hz resolution also changes. Depending on where the tail of the *sync* functions of the extracted signals coincide with these nearby interharmonics, their amplitudes can increase and decrease slightly. Figure 4.14 shows the actual current waveform in comparison with the compensated waveform. It can be seen that the latter has a shape close to an ideal sinusoidal waveform without losing the variations on its amplitude.

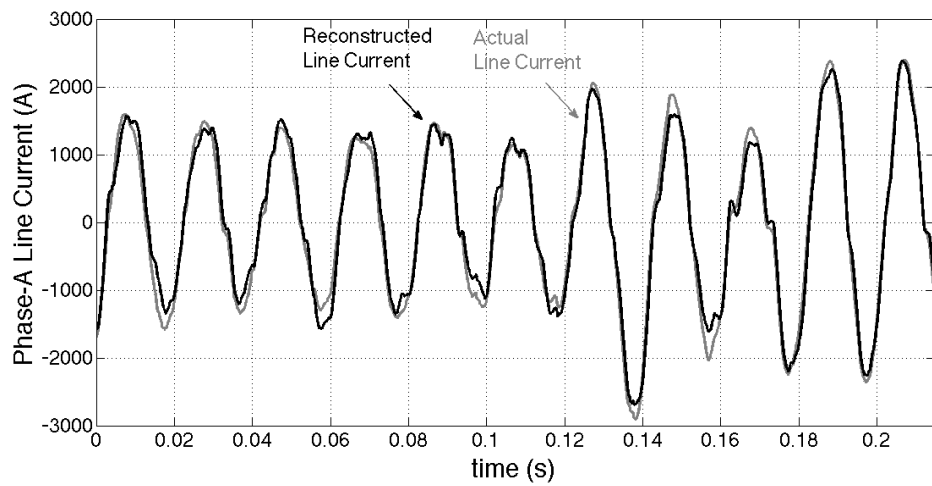
Figure 4.15 shows the actual RMS line current (black colored), RMS line current after compensation with MSRF + Butterworth Filter (red colored) and RMS line current after compensation with MSRF + Kalman Filter (blue colored) components of some major harmonics for 2 minutes. The performance of the Kalman filter is su-



(a) Boring period

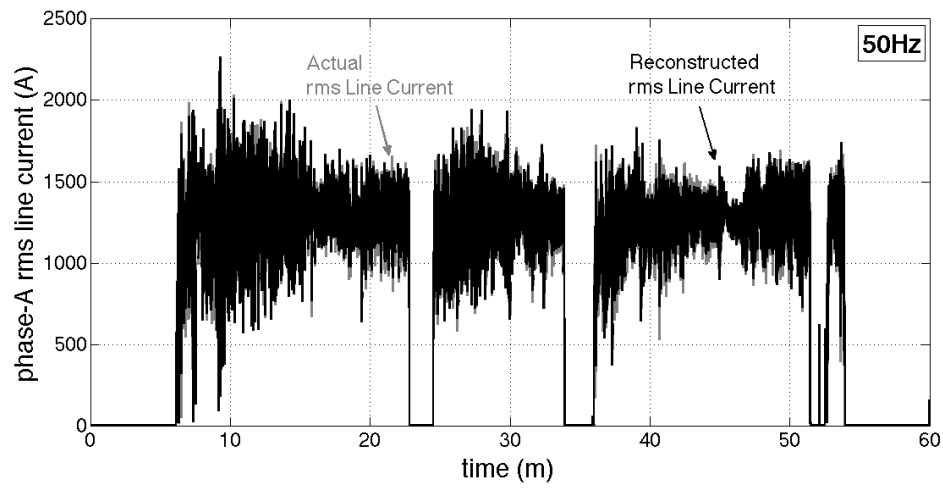


(b) Melting period after second charge

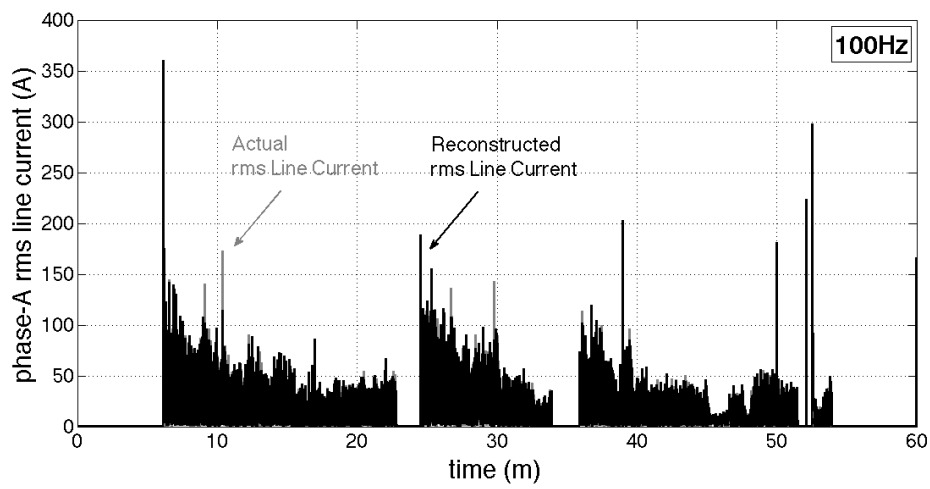


(c) Melting period after third charge

Figure 4.11: Comparison of actual and reconstructed (all harmonics and interharmonics with 5-Hz resolution are included up to 1.5kHz) line current sample waveforms.

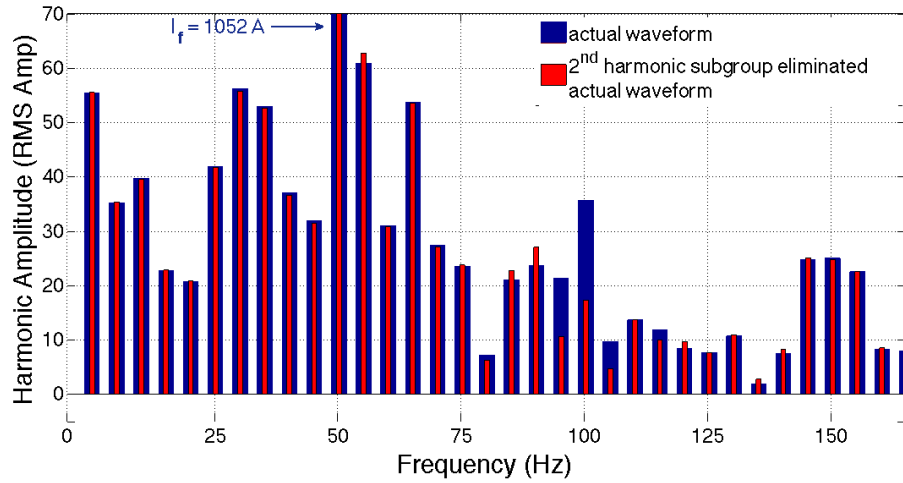


(a) 50Hz

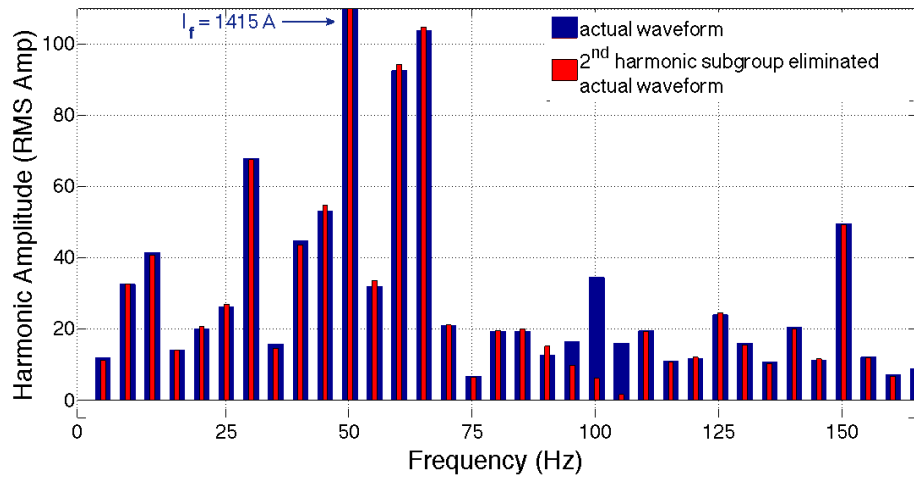


(b) 100Hz

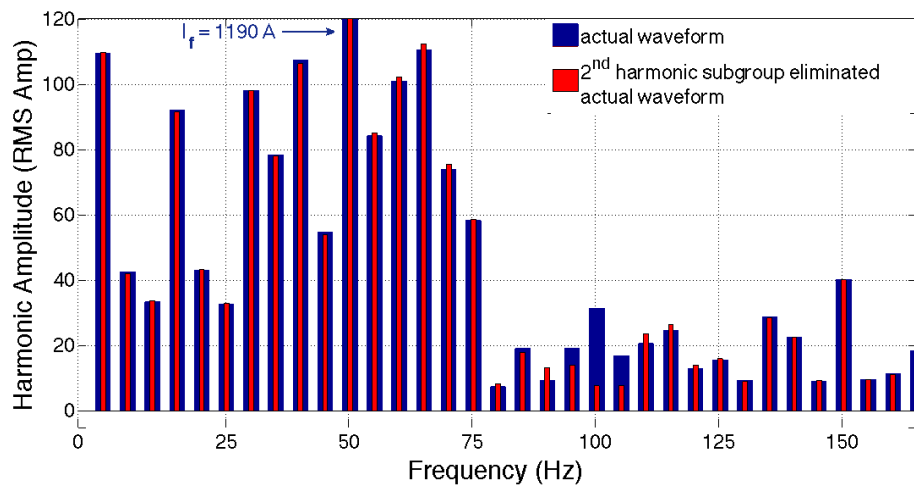
Figure 4.12: Comparison of FFT results of actual and reconstructed line current waveforms during a typical tap-to-tap time.



(a) Boring phase



(b) Melting period after second charge



(c) Melting period after third charge

Figure 4.13: 10-cycle window FFT comparison of actual and 2nd harmonic subgroup (obtained by MSRF analysis) subtracted actual line current waveforms.

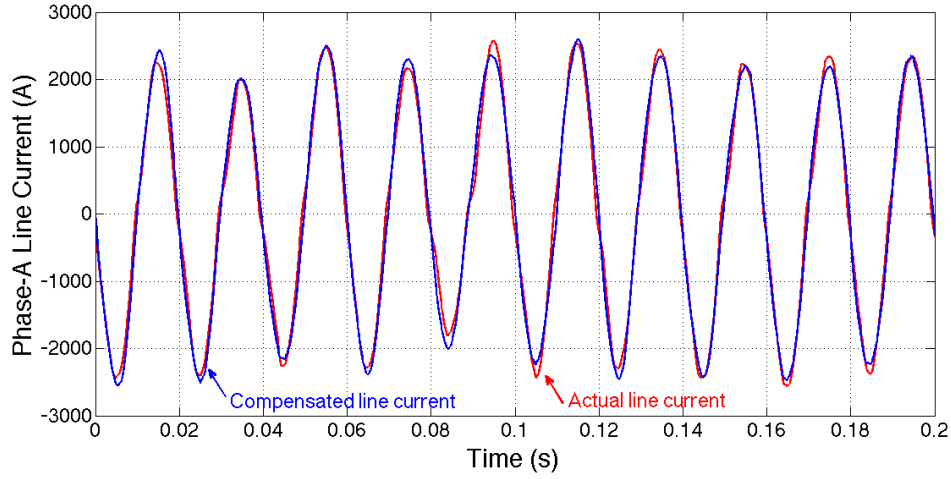
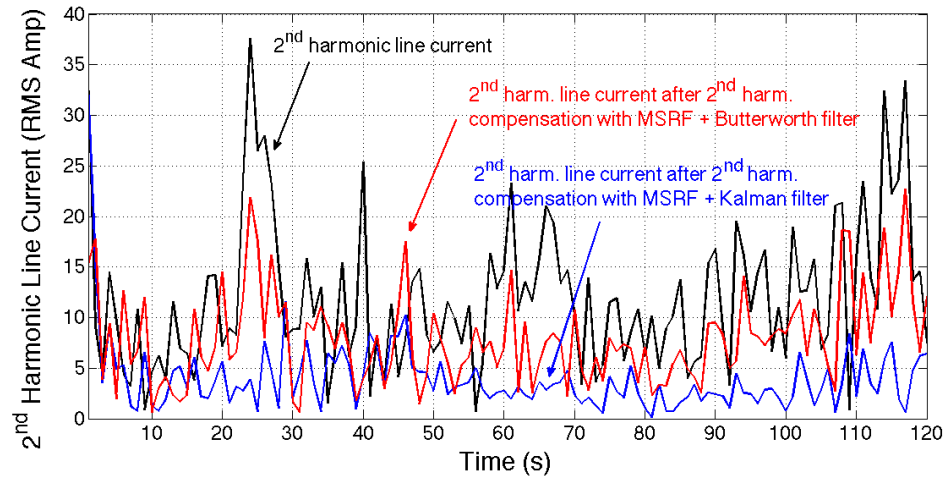


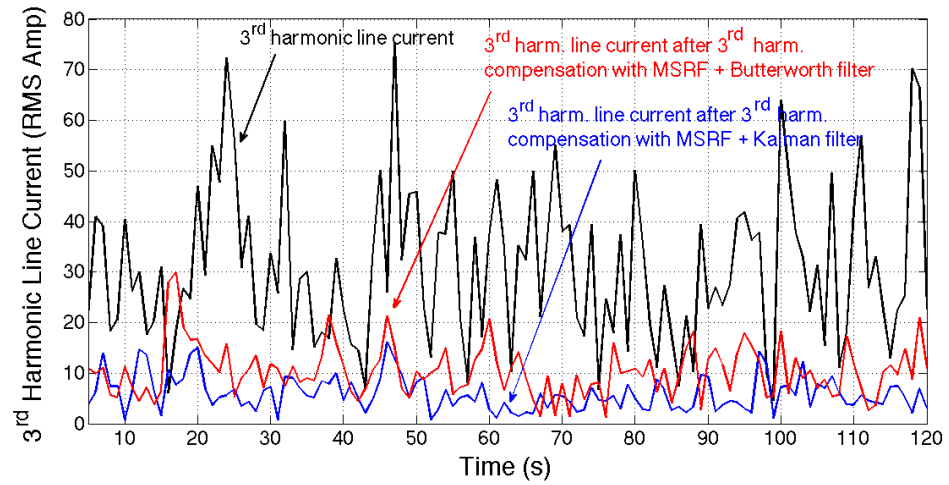
Figure 4.14: 10-cycle waveform of actual line current and filtered line current whose harmonic and interharmonic components between 65Hz and 675Hz are eliminated.

perior than the performance of the Butterworth filter in every harmonics due to the fast and accurate response of the Kalman filter. It should be noted that Butterworth filter is sometimes responsible for the amplification of the related harmonic component instead of eliminating it. The filtering performance of the Kalman filter is also satisfactory when the amplitude of the respective harmonic components is very small.

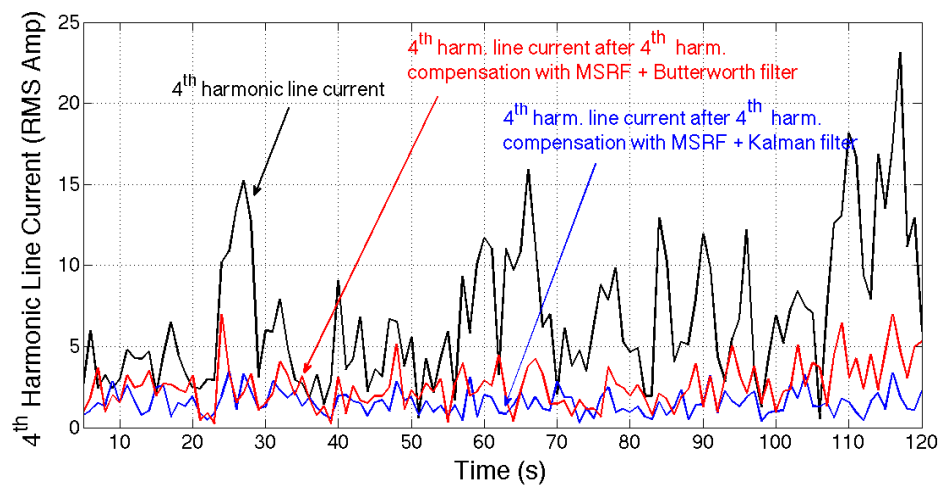
The overall filtering performance of the proposed algorithm can be observed from Figure 4.16. Only the subgroup harmonics of the fundamental frequency component are left and everything else is subtracted from the actual current waveform. The DFT results obtained from various periods in a tap-to-tap time show that the proposed MSRF analysis is well suited for the real-time applications and should be combined with fast response advance technology compensation devices.



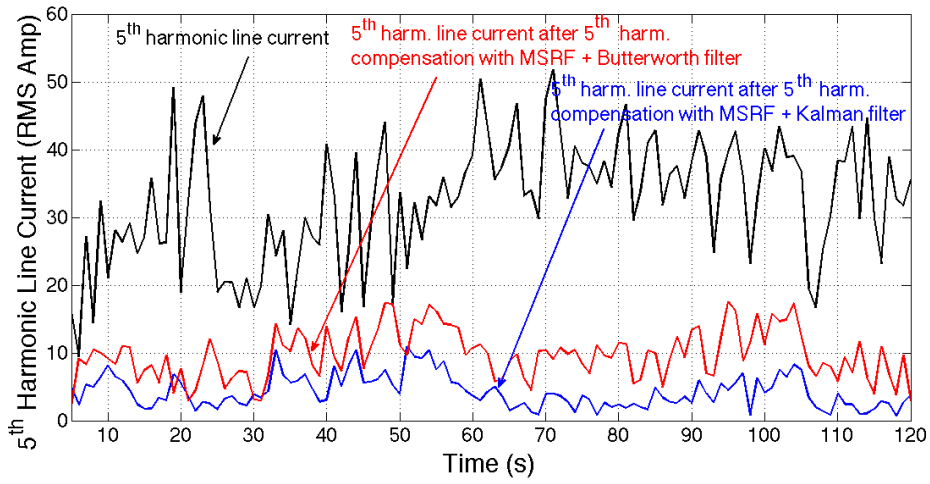
(a) $f_{iH}=100$ Hz



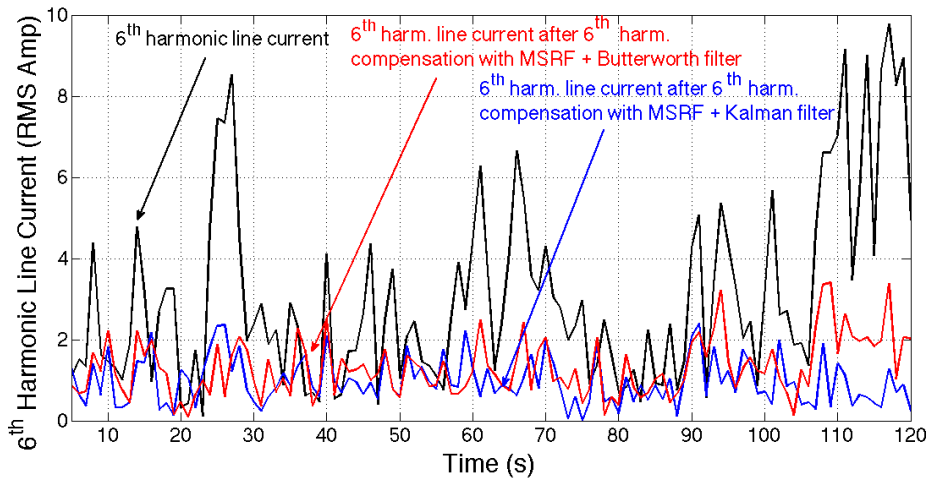
(b) $f_{iH}=150$ Hz



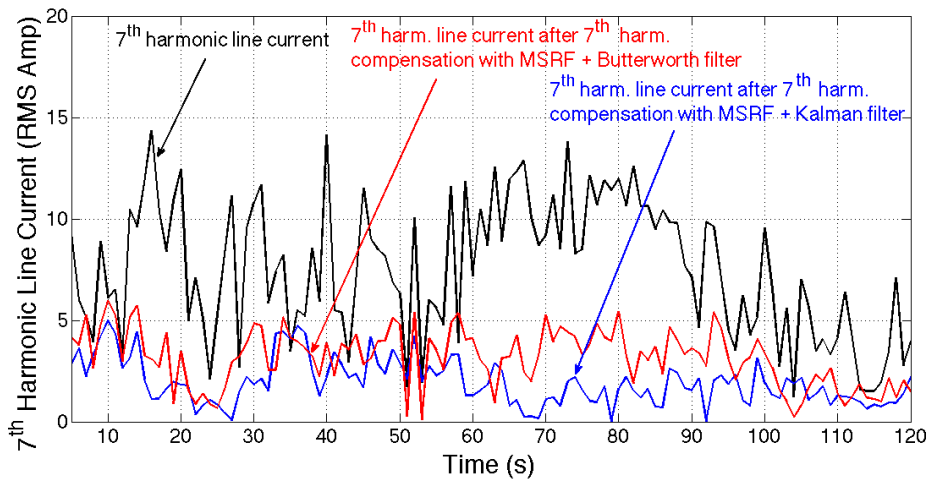
(c) $f_1=200$ Hz



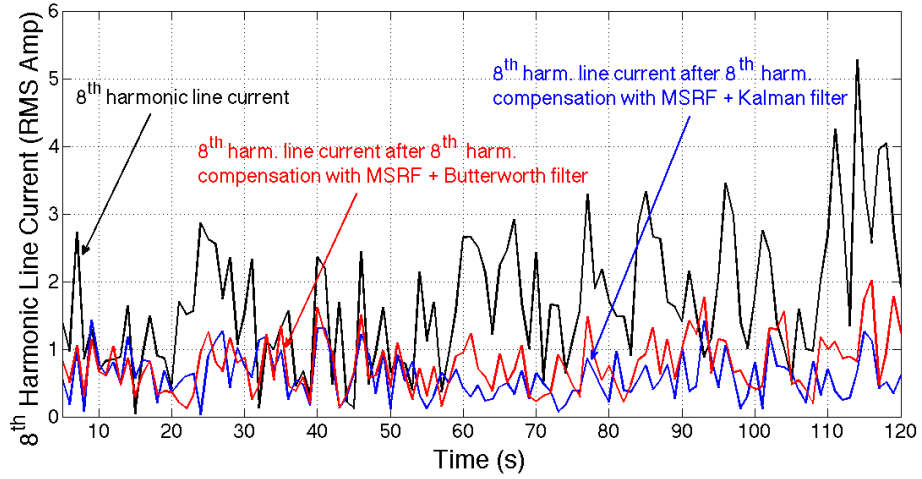
(d) $f_{iH}=250$ Hz



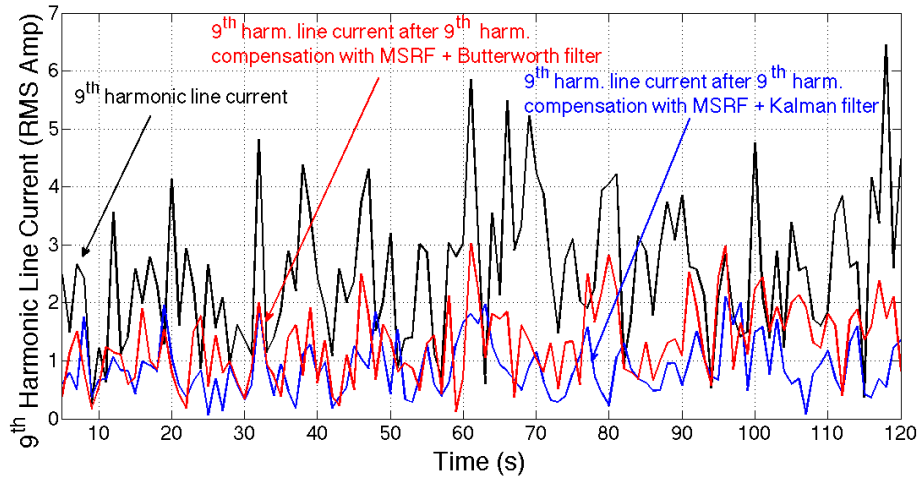
(e) $f_{iH}=300$ Hz



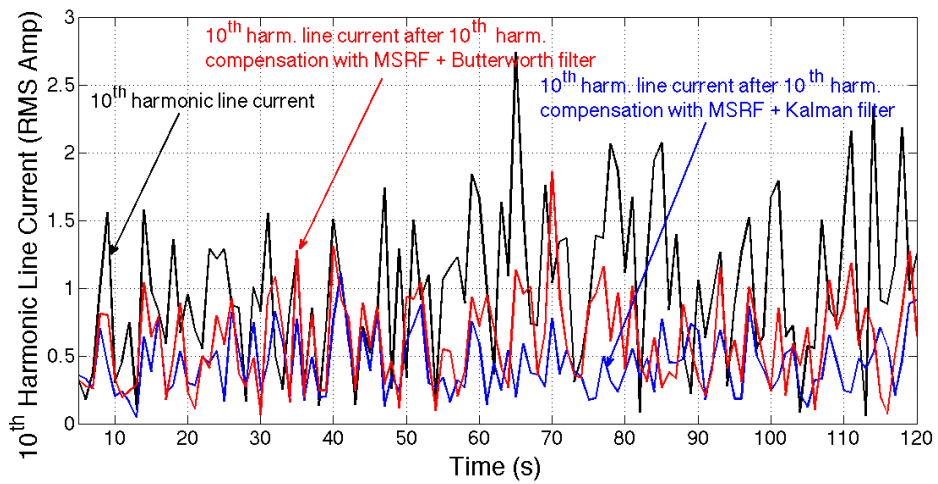
(f) $f_{iH}=350$ Hz



(g) $f_{iH}=400$ Hz

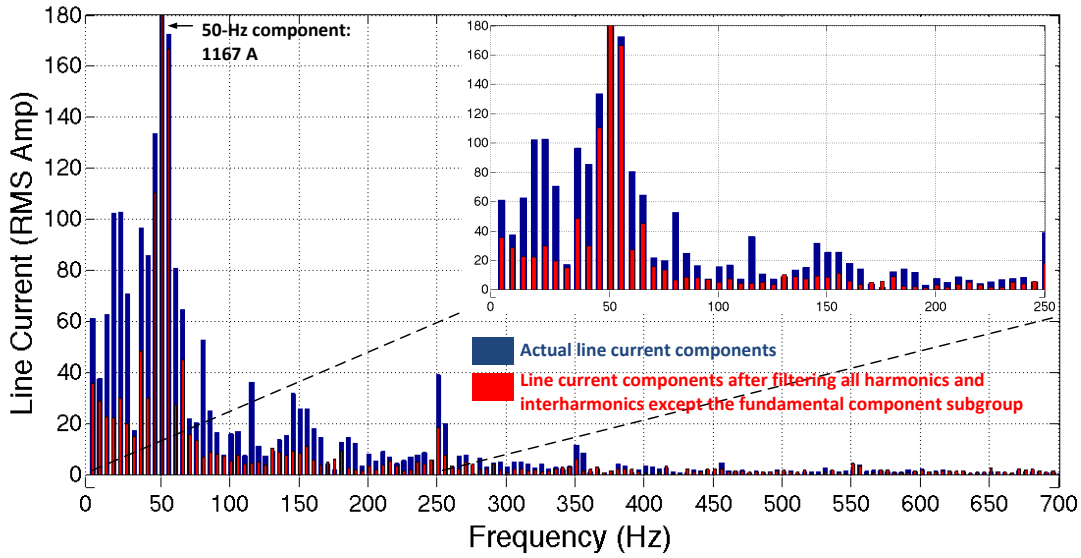


(h) $f_{iH}=450$ Hz

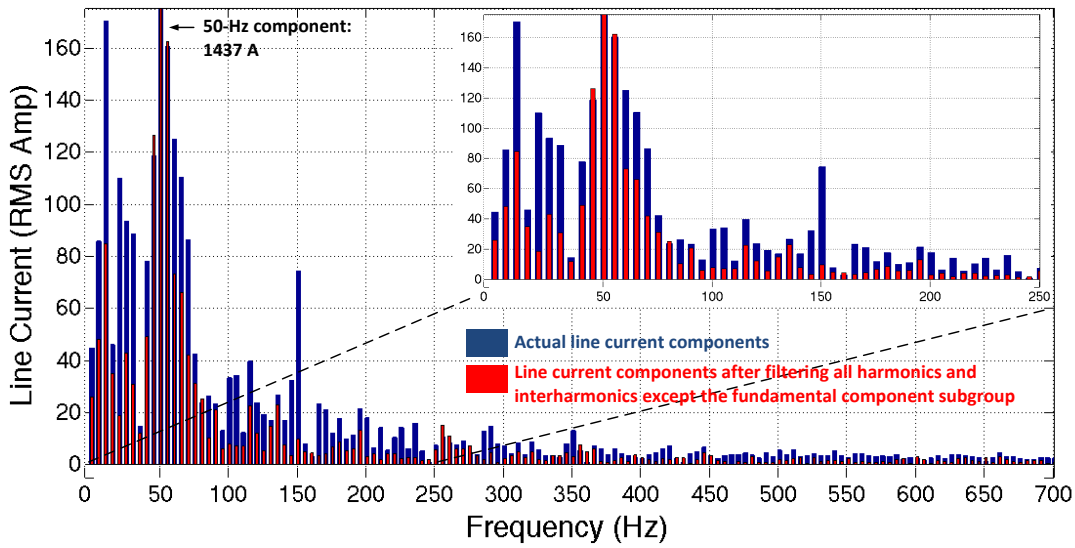


(i) $f_{iH}=500$ Hz

Figure 4.15: RMS line current components of some major harmonics during 2 minutes.



(a) Boring period



(b) Meltdown period

Figure 4.16: Comparison of FFT results of actual and compensated line current wave-forms whose all harmonic and interharmonic components except the fundamental component subgroup are eliminated.

CHAPTER 5

DISCUSSIONS AND CONCLUSIONS

An AC EAF installation can be considered as a rapidly fluctuating balanced but asymmetrical load on the power system. Real-time characterization of interharmonic and harmonic EAF currents including the fundamental component is achieved by multiple synchronous reference frame (MSRF) analysis in this thesis. By the proposed MSRF analysis framework, positive and negative sequence components of all interharmonics and harmonics can be determined fast by using a parallel computing hardware. Various field measurements and the results reported in the literature show that conventional reactive power compensation and harmonic filtering systems such as TCR-based SVCs and passive shunt harmonic filter banks tuned to the characteristic and the uncharacteristic power system harmonics are not satisfactory in reducing the interharmonics, lower order harmonics, and hence flicker to values below the planning and compatibility levels indicated in the standards. Advanced technology systems such as active power filters, STATCOMs with and without energy storage elements in their DC links, unified power flow controllers, and etc. are needed to mitigate PQ problems of AC arc furnace installations. MSRF analysis presented in the thesis can provide rapid and accurate information about all positive- and negative-sequence interharmonic and harmonic current components for the advanced technology systems to generate reference currents [3].

Second harmonic and its subgroup is the most problematic harmonic to be identified in real time. Since it is the frequency close to the fundamental frequency, the extraction of the fundamental frequency component which has comparably very high amplitude can cause misdetection of the second harmonic content if the filtration is

not so satisfactory to eliminate the effects of the fundamental component. In addition to this, the amplitudes of the second harmonic and its subgroup are comparable and change so rapidly in one cycle. Conventional second harmonic filters are able to filter the second harmonic somewhat however they also cause amplification of the interharmonics around the second harmonic and the fundamental, and hence increases the flicker level considerably. In [2], a modified C-type second harmonic filter is proposed in order to prevent this amplification, however it could not offer a solution to filter the second harmonics effectively. In this thesis, it is shown that the second harmonic is no longer a problem to identify among a waveform rich in harmonic and interharmonic content with the proposed method.

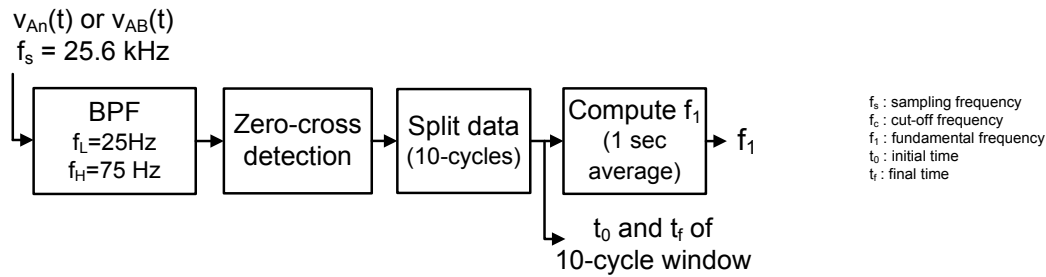


Figure 5.1: Detection of the power system fundamental frequency to update the speeds of the rotating reference frames in Figures 2.10, 2.11 and 2.12 (f_1 is the fundamental frequency of the power system).

MSRF analysis is very sensitive to the variations in the grid frequency. If the variations are considerable such as $50 \pm 0.5 \text{ Hz}$ during the application of the MSRF analysis, the fundamental frequency should be continuously detected and hence the speeds of the rotating reference frames should be updated by using the algorithm illustrated in Figure 5.1. However, in this thesis supply frequency is assumed to be constant at 50 Hz, because the interconnected system of Turkey is operating connected to the world's largest electricity system of European Network of Transmission System Operators for Electricity (ENTSO-E), thereby frequency variations are very low ($50 \pm 0.02 \text{ Hz}$). If the connection was not managed, the variation of the grid frequency would be the one shown in Figure 5.2.

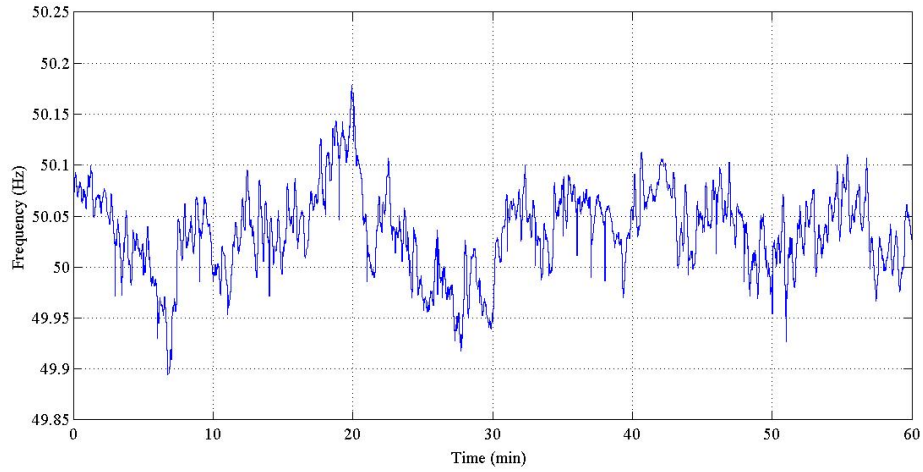


Figure 5.2: Frequency variation of power system for one hour before the interconnection.

5.1 Possible Application Areas

Since online application of MSRF analysis described in this paper can give accurate information on the magnitudes and phases of positive-sequence, negative-sequence and total phase currents of all interharmonic and harmonic components in the MV lines of the AC EAF transformer, it can be used in the generation of reference current signals for the controllers of advanced-technology systems which can be connected to the MV side of the EAF transformer to compensate for the reactive power and/or to suppress voltage flicker and some selected interharmonics/harmonics. Some of these applications may be listed as follows as in [3]:

- a Since positive- and negative-sequence components of all interharmonics and harmonics can be simultaneously resolved by using the sampled line current and voltage data, MSRF analysis permits the design and development of two separate and independent advanced technology systems such as active power filters, STATCOMs, flicker compensation systems, etc, one for the positive-sequence and the other for the negative-sequence current components. Each system will operate as a balanced and symmetrical system, thus providing ease in design, control and operation, and reduced initial cost. Otherwise, a more complicated and costly conditioning system with the ability of having independent and asymmetrical control

of the three phases would be required.

- b A low or medium size shunt active power filter can be designed and connected to the MV side of the EAF transformer via a coupling transformer to eliminate second harmonic subgroup, I_{2sg} , (root of the sum of the squares of 95-, 100-, and 105-Hz current components). By considering the time spent for the extraction of the DC, the fundamental, and the second harmonic current components from the actual current waveforms, the reference current signals are said to be applied to the APF with a delay of 20ms. In order to determine the effects of time delay on the performance of APF, a cloud diagram is developed in which $I_{A2(REF)}(t + 20 \times 10^{-3})$ signals are plotted against $I_{A2(REF)}(t)$ in Figure 5.3. Persistency results in Figure 5.3 show that magnitudes of second harmonic subgroup are not changing too rapidly, especially when the RMS value of the second harmonic current is considerably high, thereby the MSRF analysis can give quite satisfactory results in suppressing second subgroup harmonics. Similar conclusion can be drawn also for the phases of second subgroup harmonic signals.

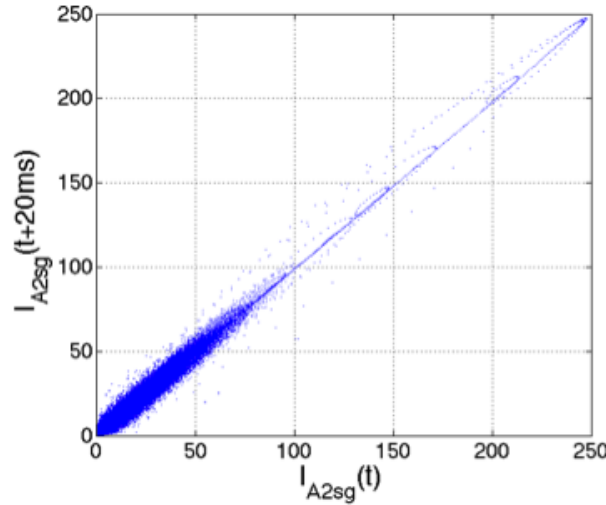


Figure 5.3: Persistency test results of second harmonic subgroup in phase-A.

- c Short term values of voltage flicker (P_{st}) at the PCC have been calculated for a typical tap-to-tap time using the current data in the MV lines of the EAF transformer and the method described in [64]. It is assumed here that, the utility grid is an infinite bus and there are no other flicker sources supplied from 154 kV and 34.5 kV busses in Figure 2.4. These flicker computations will give us only the flicker

contributions of the AC EAF installation and some countermeasures for the following cases; (i) there is no reactive power compensation or harmonic filtering, (ii) reactive current components at fundamental frequency are fully compensated, (iii) compensation is achieved according to the instantaneous-p-q theory [65, 66], (iv) interharmonics and harmonics are all eliminated, (v) interharmonics, harmonics, and reactive current at supply frequency are all eliminated (EAF installation draws only the active current component at fundamental frequency from the 34.5 kV bus). P_{st} variations in Figure 5.4 show that, a) case (ii) makes marginal contribution, and b) cases (iii) and (iv) make significant contributions in reducing P_{st} values. The flicker variation curve in Figure 5.4 for case (v) shows that P_{st} values exceed the planning level of 0.9 [54] from time to time after eliminating reactive current component at the fundamental frequency at all interharmonics and harmonics even for an infinite 154 kV bus in Figure 2.4 and in the absence of any other flicker sources. It can therefore be concluded that in order to keep P_{st} values below the planning level during the tap-to-tap time of the EAF, an advanced energy storage system should be installed in parallel with the MV side of the EAF transformer. For all other cases, especially for multi-furnace operation, it is not possible to comply with neither planning level nor the compatibility level for P_{st} [54].

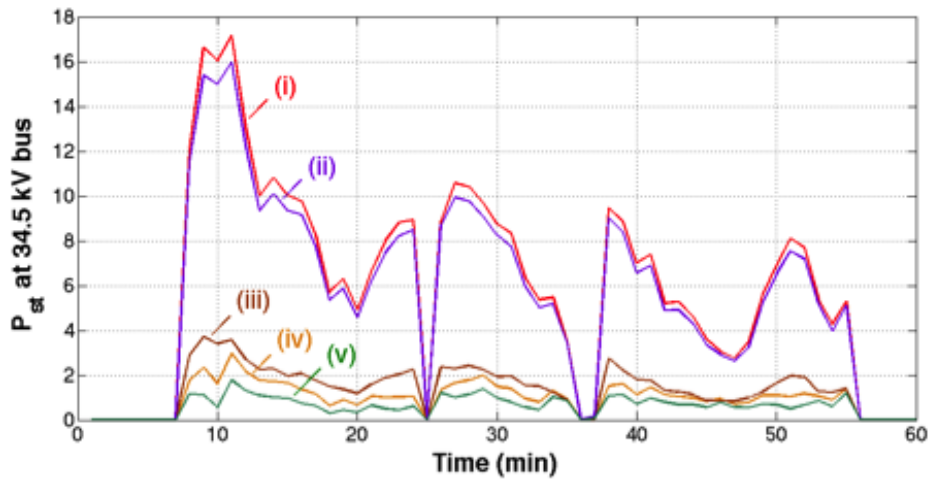


Figure 5.4: P_{st} variations at 34.5 kV bus over a typical tap-to-tap time for case studies, i) there is no reactive power compensation or harmonic filtering, ii) reactive current components at fundamental frequency are fully compensated, iii) compensation is achieved according to the instantaneous-p-q theory, iv) interharmonics and harmonics are all eliminated, v) interharmonics, harmonics, and reactive current at supply frequency are all eliminated (EAF installation draws only the active current component at fundamental frequency from the 34.5 kV bus).

REFERENCES

- [1] Gary Atkinson-Hope. Relationship between harmonics and symmetrical components. *International journal of electrical engineering education*, 41(2):93–104, 2004.
- [2] Cem Ozgur Gercek, Muammer Ermis, Arif Ertas, Kemal Nadir Kose, and Ozgur Unsar. Design, implementation, and operation of a new C-type 2nd harmonic filter for electric arc and ladle furnaces. *Industry Applications, IEEE Transactions on*, 47(4):1545–1557, 2011.
- [3] Eda Uz-Logoglu, Ozgul Salor, and Muammer Ermis. Online characterization of interharmonics and harmonics of AC electric arc furnaces by multiple synchronous reference frame analysis. *IEEE Transactions on Industry Applications*, 52(3):2673–2683, 2016.
- [4] Guan-Chyun Hsieh and James C Hung. Phase-locked loop techniques. a survey. *Industrial Electronics, IEEE Transactions on*, 43(6):609–615, 1996.
- [5] Dragan Jovcic. Phase locked loop system for FACTS. *Power Systems, IEEE Transactions on*, 18(3):1116–1124, 2003.
- [6] Baoquan Liu, Fang Zhuo, Yixin Zhu, Hao Yi, and Feng Wang. A three-phase PLL algorithm based on signal reforming under distorted grid conditions. *Power Electronics, IEEE Transactions on*, 30(9):5272–5283, 2015.
- [7] Saeed Golestan, Mohammad Monfared, and Francisco D Freijedo. Design-oriented study of advanced synchronous reference frame phase-locked loops. *Power Electronics, IEEE Transactions on*, 28(2):765–778, 2013.
- [8] Shaohua Sun, Hongqi Ben, Tao Meng, and Jinyong Zhang. A new PLL based on fast positive and negative sequence decomposition algorithm with matrix operation under distorted grid conditions. In *Power Electronics Conference (IPEC-Hiroshima 2014-ECCE-ASIA), 2014 International*, pages 3213–3217. IEEE, 2014.
- [9] Masoud Karimi-Ghartemani and Houshang Karimi. Processing of symmetrical components in time-domain. *IEEE Transactions on Power Systems*, 22(2):572–579, 2007.
- [10] Masoud Karimi-Ghartemani, Mohsen Mojiri, Alireza Safaei, Jan Åge Walseth, Sayed Ali Khajehoddin, Praveen Jain, and Alireza Bakhshai. A new phase-

- locked loop system for three-phase applications. *IEEE Transactions on Power Electronics*, 28(3):1208–1218, 2013.
- [11] Saeed Golestan, Josep Guerrero, and Juan Vasquez. Three-phase PLLs: A review of recent advances. 2016.
 - [12] Lucian Asiminoaei, Frede Blaabjerg, and Steffan Hansen. Detection is key-harmonic detection methods for active power filter applications. *Industry Applications Magazine, IEEE*, 13(4):22–33, 2007.
 - [13] Víctor M Moreno, Marco Liserre, Alberto Pigazo, and Antonio Dell’Aquila. A comparative analysis of real-time algorithms for power signal decomposition in multiple synchronous reference frames. *Power Electronics, IEEE Transactions on*, 22(4):1280–1289, 2007.
 - [14] Peng Xiao, Keith Corzine, Ganesh Kumar Venayagamoorthy, et al. Multiple reference frame-based control of three-phase PWM boost rectifiers under unbalanced and distorted input conditions. *Power Electronics, IEEE Transactions on*, 23(4):2006–2017, 2008.
 - [15] Poh Chiang Loh, Yuchen Tang, Frede Blaabjerg, and Peng Wang. Mixed-frame and stationary-frame repetitive control schemes for compensating typical load and grid harmonics. *IET power electronics*, 4(2):218–226, 2011.
 - [16] Guodong Chen, Miao Zhu, and Xu Cai. Medium-voltage level dynamic voltage restorer compensation strategy by positive and negative sequence extractions in multiple reference frames. *Power Electronics, IET*, 7(7):1747–1758, 2014.
 - [17] Sergio MA Cruz and AJ Marques Cardoso. Multiple reference frames theory: A new method for the diagnosis of stator faults in three-phase induction motors. *IEEE Transactions on Energy Conversion*, 20(3):611–619, 2005.
 - [18] Eider Robles, Josep Pou, Salvador Ceballos, Jordi Zaragoza, José Luis Martín, and Pedro Ibañez. Frequency-adaptive stationary-reference-frame grid voltage sequence detector for distributed generation systems. *Industrial Electronics, IEEE Transactions on*, 58(9):4275–4287, 2011.
 - [19] Mohsen Mojiri, Masoud Karimi-Ghartemani, and Alireza Bakhshai. Processing of harmonics and interharmonics using an adaptive notch filter. *IEEE transactions on power delivery*, 25(2):534–542, 2010.
 - [20] VM Moreno Saiz and J Barros Guadalupe. Application of Kalman filtering for continuous real-time tracking of power system harmonics. *IEE Proceedings-Generation, Transmission and Distribution*, 144(1):13–20, 1997.
 - [21] Steven Liu. An adaptive Kalman filter for dynamic estimation of harmonic signals. In *Harmonics and Quality of Power Proceedings, 1998. Proceedings. 8th International Conference On*, volume 2, pages 636–640. IEEE, 1998.

- [22] CI Chen, GW Chang, RC Hong, and HM Li. Extended real model of Kalman filter for time-varying harmonics estimation. *IEEE Transactions on Power Delivery*, 25(1):17–26, 2010.
- [23] Rafael A Flores, Irene YH Gu, and Math HJ Bollen. Positive and negative sequence estimation for unbalanced voltage dips. In *Power Engineering Society General Meeting, 2003, IEEE*, volume 4. IEEE, 2003.
- [24] N Kose, O Salor, and K Leblebicioglu. Kalman filtering based approach for light flicker evaluation of power systems. *IET generation, transmission & distribution*, 5(1):57–69, 2011.
- [25] Iman Sadinezhad and Vassilios G Agelidis. Frequency adaptive least-squares-Kalman technique for real-time voltage envelope and flicker estimation. *IEEE Transactions on Industrial Electronics*, 59(8):3330–3341, 2012.
- [26] R Yacamini. Power system harmonics. part 4: Interharmonics. *Power Engineering Journal*, 10(4):185–193, 1996.
- [27] Luis F Beites, Julio G Mayordomo, Araceli Hernández, and Rafael Asensi. Harmonics, interharmonics and unbalances of arc furnaces: a new frequency domain approach. *Power Delivery, IEEE Transactions on*, 16(4):661–668, 2001.
- [28] Özgül Salor, Burhan Gültekin, Serkan Buhan, Burak Boyrazoğlu, Tolga Inan, Tevhid Atalik, Ayse Ak, A Terciyanl, Özgür Ünsar, E Altıntas, et al. Electrical power quality of iron and steel industry in Turkey. *Industry Applications, IEEE Transactions on*, 46(1):60–80, 2010.
- [29] Ilker Yılmaz, Özgül Salor, Muammer Ermis, and Isık Çadircı. Field-data-based modeling of medium-frequency induction melting furnaces for power quality studies. *IEEE TRANSACTIONS ON INDUSTRY APPLICATIONS*, 48(4):1215, 2012.
- [30] Igor Zhezhelenko and Yuri Sayenko. Analysis methods of interharmonics investigations in power supply systems. In *Harmonics and Quality of Power, 2000. Proceedings. Ninth International Conference on*, volume 1, pages 61–63. IEEE, 2000.
- [31] Neslihan Kose and Ozgul Salor. New spectral decomposition based approach for flicker evaluation of electric arc furnaces. *Generation, Transmission & Distribution, IET*, 3(4):393–411, 2009.
- [32] Özgül Salor. Spectral correction-based method for interharmonics analysis of power signals with fundamental frequency deviation. *Electric Power Systems Research*, 79(7):1025–1031, 2009.
- [33] Emel Gunlu and Ozgul Salor. Harmonics and interharmonics analysis of power signals using synthetic resampling. In *Signal Processing and Communications Applications Conference (SIU), 2014 22nd*, pages 750–753. IEEE, 2014.

- [34] A Testa, MF Akram, R Burch, G Carpinelli, G Chang, V Dinavahi, C Hatziadoniu, WM Grady, E Gunther, M Halpin, et al. Interharmonics: theory and modeling. *Power Delivery, IEEE Transactions on*, 22(4):2335–2348, 2007.
- [35] International Electrotechnical Commission et al. Electromagnetic compatibility (EMC) Part 4-7: Testing and measurement techniques general guide on harmonics and interharmonics measurements and instrumentation, for power supply systems and equipment connected thereto. Technical report, IEC 61000-4-7, Second Edition, 2002 08, 2002.
- [36] Ilker Yilmaz, Muammer Ermiş, and Işık Çadırcı. Medium-frequency induction melting furnace as a load on the power system. *Industry Applications, IEEE Transactions on*, 48(4):1203–1214, 2012.
- [37] Jin Hui, Honggeng Yang, Wilsun Xu, and Yamei Liu. A method to improve the interharmonic grouping scheme adopted by IEC standard 61000-4-7. *Power Delivery, IEEE Transactions on*, 27(2):971–979, 2012.
- [38] Zhongdong Liu, Jörg Himmel, and Karl Walter Bonfig. Improved processing of harmonics and interharmonics by time-domain averaging. *Power Delivery, IEEE Transactions on*, 20(4):2370–2380, 2005.
- [39] Francisco AS Neves, Helber EP de Souza, Fabrício Bradaschia, Marcelo C Cavalcanti, Mario Rizo, and Francisco J Rodriguez. A space-vector discrete Fourier transform for unbalanced and distorted three-phase signals. *IEEE Transactions on Industrial Electronics*, 57(8):2858–2867, 2010.
- [40] Francisco AS Neves, Helber EP de Souza, Marcelo C Cavalcanti, Fabrício Bradaschia, and Emilio J Bueno. Digital filters for fast harmonic sequence component separation of unbalanced and distorted three-phase signals. *IEEE Transactions on Industrial Electronics*, 59(10):3847–3859, 2012.
- [41] Azam Bagheri, Mohammad Mardaneh, Amirhossein Rajaei, and Akbar Rahideh. Detection of grid voltage fundamental and harmonic components using Kalman filter and generalized averaging method. *IEEE Transactions on Power Electronics*, 31(2):1064–1073, 2016.
- [42] Cheng-I Chen and Yeong-Chin Chen. Comparative study of harmonic and interharmonic estimation methods for stationary and time-varying signals. *IEEE Transactions on Industrial Electronics*, 61(1):397–404, 2014.
- [43] Dahai Zhang, Wilsun Xu, and Yutian Liu. On the phase sequence characteristics of interharmonics. *Power Delivery, IEEE Transactions on*, 20(4):2563–2569, 2005.
- [44] Fran González-Espín, Emilio Figueres, and Gabriel Garcera. An adaptive synchronous-reference-frame phase-locked loop for power quality improve-

- ment in a polluted utility grid. *IEEE Transactions on Industrial Electronics*, 59(6):2718–2731, 2012.
- [45] Kyoung-Jun Lee, Jong-Pil Lee, Dongsul Shin, Dong-Wook Yoo, and Hee-Je Kim. A novel grid synchronization PLL method based on adaptive low-pass notch filter for grid-connected PCS. *IEEE Transactions on Industrial Electronics*, 61(1):292–301, 2014.
 - [46] Mihaela Popescu, Alexandru Bitoleanu, and Vlad Suru. A DSP-based implementation of the pq theory in active power filtering under nonideal voltage conditions. *IEEE Transactions on Industrial Informatics*, 9(2):880–889, 2013.
 - [47] Muhammad Tahir and Sudip K Mazumder. Improving dynamic response of active harmonic compensator using digital comb filter. *IEEE Journal of Emerging and Selected Topics in Power Electronics*, 2(4):994–1002, 2014.
 - [48] Eric Monmasson, Lahoucine Idkhajine, Marcian N Cirstea, Imene Bahri, Alin Tisan, and Mohamed Wissem Naouar. FPGAs in industrial control applications. *IEEE Transactions on Industrial Informatics*, 7(2):224–243, 2011.
 - [49] Naji Rajai Nasri Ama, Fernando Ortiz Martinz, Lourenço Matakas, and Fuad Kassab. Phase-locked loop based on selective harmonics elimination for utility applications. *IEEE Transactions on Power Electronics*, 28(1):144–153, 2013.
 - [50] Giovanni Betta, Luigi Ferrigno, and Marco Laracca. Cost-effective FPGA instrument for harmonic and interharmonic monitoring. *IEEE Transactions on Instrumentation and Measurement*, 62(8):2161–2170, 2013.
 - [51] Paulo SB Nascimento, Helber EP De Souza, Francisco AS Neves, and Leonardo R Limongi. FPGA implementation of the generalized delayed signal cancelation—Phase locked loop method for detecting harmonic sequence components in three-phase signals. *IEEE Transactions on Industrial Electronics*, 60(2):645–658, 2013.
 - [52] Vincent Roberge, Mohammed Tarbouchi, and Gilles Labonté. Parallel algorithm on graphics processing unit for harmonic minimization in multilevel inverters. *IEEE Transactions on Industrial Informatics*, 11(3):700–707, 2015.
 - [53] Hadis Karimipour and Venkata Dinavahi. Extended Kalman filter-based parallel dynamic state estimation. *IEEE Transactions on Smart Grid*, 6(3):1539–1549, 2015.
 - [54] International Electrotechnical Commission et al. Electromagnetic compatibility (EMC) Part 3-7: Limits—Assessment of emission limits for the connection of distorting installations to MV, HV and EHV power systems, February 2008. Technical report, IEC 61000-3-6.

- [55] IEEE 519 Working Group et al. IEEE recommended practices and requirements for harmonic control in electrical power systems. *IEEE Std*, pages 519–1992, 1992.
- [56] Regulation on service quality in electricity distribution and retail sale. <http://www.emra.org.tr/index.php/electricity-market/legislation/>, 2013. Last accessed on April 2015.
- [57] Colin Schauder. STATCOM for compensation of large electric arc furnace installations. In *Power Engineering Society Summer Meeting, 1999. IEEE*, volume 2, pages 1109–1112. IEEE, 1999.
- [58] R Grunbaum. SVC light: A powerful means for dynamic voltage and power quality control in industry and distribution. In *IEE Conference Publication*, pages 404–409. London; Institution of Electrical Engineers; 1999, 2000.
- [59] Lucian Asiminoaei, Frede Blaabjerg, and Steffan Hansen. Evaluation of harmonic detection methods for active power filter applications. In *20th Annual IEEE Applied Power Electronics Conference and Exposition, 2005. APEC 2005.*, volume 1, pages 635–641. IEEE, 2005.
- [60] Charles L Fortescue. Method of symmetrical co-ordinates applied to the solution of polyphase networks. *Transactions of the American Institute of Electrical Engineers*, 37(2):1027–1140, 1918.
- [61] WC Duesterhoeft, Max W Schulz, and Edith Clarke. Determination of instantaneous currents and voltages by means of alpha, beta, and zero components. *Transactions of the American Institute of Electrical Engineers*, 70(2):1248–1255, 1951.
- [62] Robert H Park. Two-reaction theory of synchronous machines generalized method of analysis-part I. *Transactions of the American Institute of Electrical Engineers*, 48(3):716–727, 1929.
- [63] Tevhid Atalik, Isik Çadirci, Turan Demirci, Muammer Ermiş, Tolga Inan, Alper Sabri Kalaycioglu, and Ozgul Salor. Multipurpose platform for power system monitoring and analysis with sample grid applications. *Instrumentation and Measurement, IEEE Transactions on*, 63(3):566–582, 2014.
- [64] Erineç Altıntaş, Özgül Salor, Işık Çadirci, and Muammer Ermiş. A new flicker contribution tracing method based on individual reactive current components of multiple EAFs at PCC. *Industry Applications, IEEE Transactions on*, 46(5):1746–1754, 2010.
- [65] Hirofumi Akagi, Edson Hirokazu Watanabe, and Mauricio Aredes. *Instantaneous power theory and applications to power conditioning*, volume 31. John Wiley & Sons, 2007.

- [66] Vasco Soares, Pedro Verdelho, and Gil D Marques. An instantaneous active and reactive current component method for active filters. *Power Electronics, IEEE Transactions on*, 15(4):660–669, 2000.

CURRICULUM VITAE

PERSONAL INFORMATION

Surname, Name: Uz-Loğoğlu, Eda

Nationality: Turkish (TC)

Date and Place of Birth: 01.01.1983, İskenderun

Marital Status: Married

Phone: 0 533 5532331

E-mail: edauz.ee@gmail.com

EDUCATION

Degree	Institution	Year of Graduation
M.S.	Electrical & Electronics Eng. Dept., METU	2010
B.S.	Electrical & Electronics Eng. Dept., METU	2007

PROFESSIONAL EXPERIENCE

Year	Place	Enrollment
April 2013 - Present	ASELSAN A.Ş.	Senior Design Engineer
July 2007 - March 2013	TUBITAK - UZAY	Researcher

PUBLICATIONS

Journal

[1] E. Uz-Logoglu, O. Salor, and M. Ermis, "Online characterization of interharmonics and harmonics of AC electric arc furnaces by multiple synchronous reference frame analysis", *Industry Applications, IEEE Transactions on*, 52(3):2673-2683, 2016.

Proceedings

[2] E. Durna, D. Parlak, E. U. Loğoğlu and C. Ö Gerçek, "Adaptation of renewable based power plants to the energy market using battery energy storage systems," *Renewable Energy Research and Application (ICRERA), 2014 International Conference on*, Milwaukee, WI, 2014, pp. 643-647.

[3] E. Uz Loğoğlu, "High power three phase series resonant DC/DC converter," *Electrical, Electronics and Computer Engineering (ELECO), 2010 National Conference on*, Bursa, 2010, pp. 273-277.